Lawrence Berkeley National Laboratory
Recent Work

Title
Ultrashort X-ray Pulse Science

Permalink
https://escholarship.org/uc/item/02c027bh

Author
Chin, Alan H.

Publication Date
1998-05-22

ERNEST ORLANDO LAWRENCE
BERKELEY NATIONAL LABORATORY

Ultrashort X-ray Pulse Science

Alan H. Chin

Materials Sciences Division

May 1998

Ph.D. Thesis

DISCLAIMER

Ultrashort X-ray Pulse Science

Alan Hap Chin
Ph.D. Thesis

Department of Physics
University of California, Berkeley

and

Materials Sciences Division
Ernest Orlando Lawrence Berkeley National Laboratory
University of California
Berkeley, CA 94720

May 1998

Ultrashort X-ray Pulse Science

by

Alan Hap Chin

B.S. (Oregon State University) 1990
B.S. (Oregon State University) 1990
M.A. (University of California, Berkeley) 1993

A dissertation submitted in partial satisfaction of the

requirements for the degree of

Doctor of Philosophy

in

Physics

in the

GRADUATE DIVISION

of the

UNIVERSITY OF CALIFORNIA, BERKELEY

Committee in charge:

Professor Charles V. Shank, Chair
Professor Roger W. Falcone
Professor David T. Attwood

Spring 1998

Ultrashort X-ray Pulse Science

Copyright © 1998

by

Alan Hap Chin

This work is dedicated to

my family and friends,

who have encouraged and supported me all these years.

Acknowledgements

Graduate studies in the physics department at the University of California at Berkeley have been both challenging and rewarding for me. There is no doubt I would not have been able to achieve my goal of obtaining a Ph.D. degree without the support of my family and friends – both old and new. With their help, the graduate student experience has been one that I will fondly look back upon.

I thank all of my classmates with whom I attended classes and struggled through homework assignments with for giving me confidence in my abilities. There are also more practical matters that have to be addressed while being a graduate student. I have to thank Anne Takizawa for her help in getting me and my fellow classmates through all of the various red tape that is part of being a student at U.C. Berkeley. I also thank all of the other members of the physics department staff who have also helped me.

I think surviving graduate school is impossible without fellow graduate students to commiserate with. The group of graduate students with whom I've had the pleasure of commiserating the most is of course my fellow lab mates. Chris Bardeen, Qing Wang, Alvin Yeh and I have all been through the sweat shop that is the Shank Research Group. I definitely have to thank these guys for assisting me - whether its helping me understand some obscure point about physics, or simply helping me carry some heavy piece of equipment. I am especially grateful for the friendship they have provided; this was essential for making life in the lab bearable.

Of course, the main purpose of graduate school for me was to learn how to become a physicist. For helping me achieve that goal, I have to thank Bob Schoenlein. He

has served as my surrogate advisor throughout my time in the Shank group. His knowledge and advice has helped me "learn the ropes" and will hopefully help me become a successful physicist. Ernie Glover has also been a particularly good resource of knowledge as well as comic relief, and working with him has been a pleasure. Giulio Cerullo, Peter Balling, and Sandy Rosenthal have also been good resources during their stays in the Shank group. Our collaborators, Wim Leemans, Pavel Volfbeyn, and others in the Center for Beam Physics deserve thanks for stimulating conversations and technical expertise; the Thomson scattering x-ray source would not exist without their help. I am particularly indebted to my research advisor, Prof. Charles Shank, for giving me a chance to perform research in his group. Although quite busy with his lab director duties, he has provided me with invaluable support and advice. I am also grateful for the opportunity to interact with the other members of my thesis committee – Prof. David Attwood, and Prof. Roger Falcone - as well the many other professors with whom I have taken classes.

Finally, I have to thank the friends and family who have supported me throughout my graduate career. I am indebted to my younger brother, Jerry, for his encouragement and agreeing to join me on my crazy trips. Tom (Yukka) Lau, Peter Kwok, Tseng Wong, David Young, Manh Lerng, and the rest of my Portland connection have been supportive throughout. Jim Morehead, Peter Kner, and Tom Lee and other friends I have made more recently have provided me with invaluable support and entertainment. Jim in particular helped nurse me through perhaps the low point of my life – the post ACL surgery period. Joan Chang deserves special thanks for exposing me to a wider range of pursuits. I am grateful to these people and others who have both helped me and changed me for the better.

Table of Contents

List of Figures

Abstract

Ultrashort X-Ray Pulse Science

by

Alan Hap Chin

Doctor of Philosophy in Physics

University of California, Berkeley

Professor Charles V. Shank, Chair

A variety of phenomena involves atomic motion on the femtosecond time-scale.
These phenomena have been studied using ultrashort optical pulses, which indirectly probe
atomic positions through changes in optical properties. Because x-rays can more directly
probe atomic positions, ultrashort x-ray pulses are better suited for the study of ultrafast
structural dynamics. One approach towards generating ultrashort x-ray pulses is by 90°
Thomson scattering between terawatt laser pulses and relativistic electrons. Using this
technique, we generated ~ 300 fs, 30 keV (0.4 Å) x-ray pulses. These x-ray pulses are
absolutely synchronized with ultrashort laser pulses, allowing femtosecond optical
pump/x-ray probe experiments to be performed.

Using the right-angle Thomson scattering x-ray source, we performed time-
resolved x-ray diffraction studies of laser-perturbed InSb. These experiments revealed a
delayed onset of lattice expansion. This delay is due to the energy relaxation from a dense
electron-hole plasma to the lattice. The dense electron-hole plasma first undergoes Auger
recombination, which reduces the carrier concentration while maintaining energy content.

1

Longitudinal-optic (LO) phonon emission then couples energy to the lattice. LO phonon decay into acoustic phonons, and acoustic phonon propagation then causes the growth of a thermally expanded layer.

Source characterization is instrumental in utilizing ultrashort x-ray pulses in time-resolved x-ray spectroscopies. By measurement of the electron beam diameter at the generation point, the pulse duration of the Thomson scattered x-rays is determined. Analysis of the Thomson scattered x-ray beam properties also provides a novel means of electron bunch characterization. Although the pulse duration is inferred for the Thomson scattering x-ray source, direct measurement is required for other x-ray pulse sources. A method based on the laser-assisted photoelectric effect (LAPE) has been demonstrated as a means of measuring ultrashort x-ray pulse durations. LAPE may also serve as the basis for a gated x-ray detector.

The development of the Thomson scattering x-ray source and its application to the study of laser-perturbed InSb represent some of the first steps towards studying ultrafast structural dynamics using ultrashort x-ray pulses. To allow a wider range of applications, sources with higher spectral brightness are required. Schemes to achieve higher spectral brightness are discussed.

Chapter 1: Introduction

Since the advent of femtosecond lasers [1, 2], many ultrafast phenomena in condensed matter have been studied with femtosecond temporal resolution using ultrashort laser pulses [3, 4]. The ability to excite solids and molecules impulsively with ultrashort laser pulses (down to ~ 5 fs [5-8]) permits the study of many relaxation or energy-transfer processes that would otherwise not be observable. Many of these phenomena are purely electronic in nature, and are accessible to study using light near the visible regime. However, a variety of interesting phenomena in condensed matter involves ultrafast atomic motion [9]. For example, ultrashort laser pulse induced disordering [10, 11], surface desorption [12], coherent phonons [13], and photo-dissociation [14] all involve the motion of atoms on a femtosecond time scale. These phenomena have mainly been studied by using changes in optical properties induced by changes in atomic coordinates. However, the connection between atomic structure and optical properties is not always straightforward. A more direct method for studying ultrafast structural dynamics is clearly needed.

X-ray techniques have long been used to determine atomic structure in condensed matter. This is because x-rays interact with core-shell electrons, and these electrons lie within atomic radii. One of these techniques, x-ray diffraction, is an established technique for determining crystal structure (long-range order) [15]. The regular atomic arrangement of a crystal can be directly obtained from the Fourier transform of x-ray diffraction patterns, which is straightforward for simple crystals. Another x-ray technique, Extended X-ray Absorption Fine Structure (EXAFS) and related x-ray absorption spectroscopies,

1

can be used to determine local atomic environments (short-range order) [16, 17], which is particularly useful for studying non-crystalline matter. EXAFS refers to the oscillation in the x-ray absorption as a function of x-ray photon energy, just above an absorption edge. The Fourier components of this oscillation depend in a simple manner on the interatomic spacing. This allows nearest-neighbor distances to be readily obtained. Using these x-ray techniques with ultrashort x-ray pulses would allow for the study of ultrafast atomic motion phenomena in condensed matter.

Schemes for Generating Ultrashort X-Ray Pulses

As summarized in Table 1.1, various schemes have been proposed and implemented for generating ultrashort x-ray pulses [18]. The method of ultrashort x-ray pulse generation that has received the most attention is laser-produced plasma x-ray emission [19, 20]. These plasma-based sources are capable of generating x-ray pulses with photon energies up to the hard x-ray regime. However, laser-produced plasma x-rays are highly divergent, and the x-ray pulse duration using these sources is dependent upon the characteristics of the generating laser pulse and the resulting plasma [21].

Another scheme, high-order harmonic generation, has been shown to produce ultrashort soft x-ray pulses. By using a novel technique of x-ray pulse and laser pulse cross-correlation based on the laser assisted photoelectric effect (LAPE), the pulse duration of high-order harmonic x-rays were measured to be on the order of the generating laser pulse duration [22]. In fact, the intrinsic pulse duration of high-order harmonics should be much less than the generating laser pulse duration [23, 24], but the effects of the spatial and temporal laser profile tend to broaden the harmonic pulse

2

duration. Although ultrashort soft x-ray pulses can be generated in this way, extending to higher x-ray energies is difficult. This lack of hard x-ray generation limits the range of applications of high-order harmonic sources. The generation of multiple harmonics can pose a problem if a monochromatic x-ray beam is desired. Monochromators can be used to select individual harmonics, but the resulting losses due to poor grating efficiency may not be tolerable.

Source	Advantages	Disadvantages
Laser-Produced Plasmas	• Large x-ray flux • Tunable by using different material K-α lines, or broadband plasma emission	• Highly divergent ($\sim 4\pi$ solid angle) • Pulse duration and flux are highly dependent on laser and plasma parameters
High-Order Harmonics	• Subpicosecond x-ray pulses • Highly collimated • Spatial and temporal coherence	• Limited to soft x-rays • Many harmonics (if monochromatic beam is desired)
Synchrotrons	• High-brightness • Tunable • Collimated	• Pulse duration limited by the electron bunch length (~ 100 ps) • Very expensive
Laser-synchrotrons	• Tunable • Collimated • Subpicosecond x-ray pulses possible	• Relatively low average flux • Bandwidth

Table 1.1: Ultrashort x-ray pulse sources.

The most expensive scheme of x-ray pulse generation are the storage ring synchrotron based x-ray sources. Although they provide highly directed, tunable x-ray beams, the x-ray pulse duration from these sources is limited by the electron bunch duration. However, special techniques can be used to provide femtosecond resolution,

such as gating the x-ray detection, producing femtosecond slices of the longer electron

pulses [25], or x-ray pulse switching [26].

Laser-synchrotron sources are more compact sources of directed x-rays than

synchrotrons, as only a lower energy electron beam from a linear accelerator is necessary

[27-29]. In these sources, the relativistic electrons see Doppler upshifted light in the UV

regime, which are Thomson scattered in the rest frame of the electrons (i.e. the frame of

reference moving with the electrons). In the lab frame, this scattered light is once again

Doppler upshifted, yielding photons with energy in the x-ray regime. Unfortunately, the

conventional back-scattering geometry yields x-ray pulses that are as long as the electron

pulses used to generate them.

Right-Angle Thomson Scattering X-Ray Source

An ideal source of ultrashort x-ray pulses would provide highly directed,

subpicosecond, tunable pulses of x-rays synchronized with ultrashort laser pulses. One

source that fulfils these criteria is the right angle Thomson scattering x-ray source. Being a

laser synchrotron source, the right angle Thomson scattering source is capable of

generating highly directed beams of x-rays, as described above. By scattering the laser

photons at right angles relative to the relativistic electrons, the x-ray pulse duration is

determined by the transit time of the ultrashort laser pulses across the electron beam waist

[30]. Focusing the electron beam down to a small enough spot (~ 90 μm), the x-ray pulse

duration can be made to be subpicosecond (~ 300 fs). The source is also tunable by

changing the angle of interaction between the laser and electron beams, the electron beam

energy, or the laser photon energy. Because laser pulses are used to generate the x-ray

pulses, the ultrashort x-ray pulses are absolutely synchronized to the laser pulses. This is crucial to extract the maximum time resolution in time-resolved x-ray diffraction or x-ray absorption experiments.

Although it has many advantages, the right-angle Thomson scattering x-ray source suffers from relatively poor x-ray flux. The poor x-ray yield is due to the small Thomson cross-section for electron-photon scattering along with the use of only a small portion of the electron bunch in the right-angle geometry. As shown below, the source also suffers from a relatively broad bandwidth, which may be disadvantageous for some experiments (e.g. x-ray diffraction). This is a disadvantage for an x-ray source, but it opens up the possibility for microprobing electron bunches [31, 32]. This possibility arises because the electron beam emittance can have a significant effect on both the x-ray beam divergence and the x-ray spectral characteristics, and because the laser pulse only interacts with a small portion of the electron beam. Thus, performing Thomson scattering in the right-angle geometry offers the possibility of microprobing the electron beam emittance, rather than averaging over the entire electron bunch. This opens the possibility of studying electron beam dynamics within a bunch.

Because they offer many attractive features, right-angle (or more generally, large angle) Thomson scattering x-ray sources will receive considerable attention. Future improvements in linear accelerator technology and laser technology should overcome the intrinsic problem of poor laser photon to x-ray photon conversion efficiency. High-brightness linear accelerators using laser photocathodes and multi-terawatt peak power laser systems are becoming mature technologies. Continued development of laser and

electron beam technology will make large-angle Thomson scattering x-ray sources useful tools for studying ultrafast structural dynamics in condensed matter [33].

Applications of Ultrashort X-Ray Pulses

A large number of applications for ultrashort x-ray pulse sources will be available with continued source development. One such application involves the response of semiconductors to intense laser excitation. This response includes phenomena such as lattice heating [34], shock wave propagation [35], and annealing [36-38]. Perhaps the most interesting of these phenomena is the ultrafast disordering of semiconductors under intense laser excitation [10, 39]. Ultrafast disordering occurs due to the excitation of a large number of electron-hole pairs (the creation of a dense electron-hole plasma). This may also be viewed as the promotion of a large number of electrons from bonding to anti-bonding orbitals. This conversion to a large number of anti-bonding orbitals weakens the restoring force between atoms in the semiconductor (modifies the atomic potential energy), allowing the atoms to move more freely. For a dense enough electron-hole plasma, the result is a lattice instability due to a change in the potential energy of the atoms, allowing atomic disordering to occur in the semiconductor [39-44]. The high-density electron-hole plasma generated under these conditions dominates the optical properties of the excited semiconductor, and a connection between atomic order and optical properties may become disguised. For example, optical surface second harmonic techniques are sensitive to atomic order in a thin surface layer under normal conditions [45], but can become significantly modified by a dense electron-hole plasma [46]. Therefore, a more direct probe of atomic structure, such as x-rays, is desirable for the

study ultrafast disordering of semiconductors.

As x-rays interact with core-shell electrons, using ultrashort x-ray pulses synchronized to laser pulses allows one to more directly probe ultrafast structural changes in condensed matter induced by ultrashort laser pulses. This is done by delaying the x-ray pulse relative to the laser pulse and monitoring changes in x-ray properties as a function of time delay. For example, performing time-resolved x-ray diffraction, one may observe the changes in long-range order in a crystal by observing the changes in the x-ray diffraction signal as a function of time delay. Similarly, time-resolved x-ray absorption experiments can provide information about local or short-range atomic order dynamics in condensed matter. Both of these complementary techniques can provide a picture of the time evolution of the atoms in a laser perturbed condensed matter system.

Chapter 2: Right-Angle Thomson Scattering X-Ray Source

We built a source based on right-angle Thomson scattering because of the advantages of a highly collimated beam of tunable ultrashort x-ray pulses [33]. Another advantage of Thomson scattering x-ray sources, especially when comparing them to laser-produced plasma based sources, is that they are based on relatively simple physics. Understanding the underlying physics behind the x-ray generation leads to reliable source characteristics and operation. In this chapter, relativistic Thomson scattering theory, experimental details and results, and electron beam characterization using Thomson scattering will be discussed.

Relativistic Thomson Scattering Theory

The basic idea behind the right-angle Thomson scattering x-ray source, shown schematically in Figure 2.1, is to increase the energy of laser photons into the x-ray regime by Thomson scattering the laser photons off of relativistic electrons. A quantitative description of the Thomson scattering x-ray source can be obtained by using one of three descriptions: the colliding particle picture, the undulator picture, and the Thomson scattering picture. Single electron theory will be described first, followed by electron beam emittance effects on the x-rays generated.

Single electron theory

Perhaps the simplest description of the Thomson scattering x-ray source is the colliding particle picture. Viewing both photons and electrons as particles, laser photons
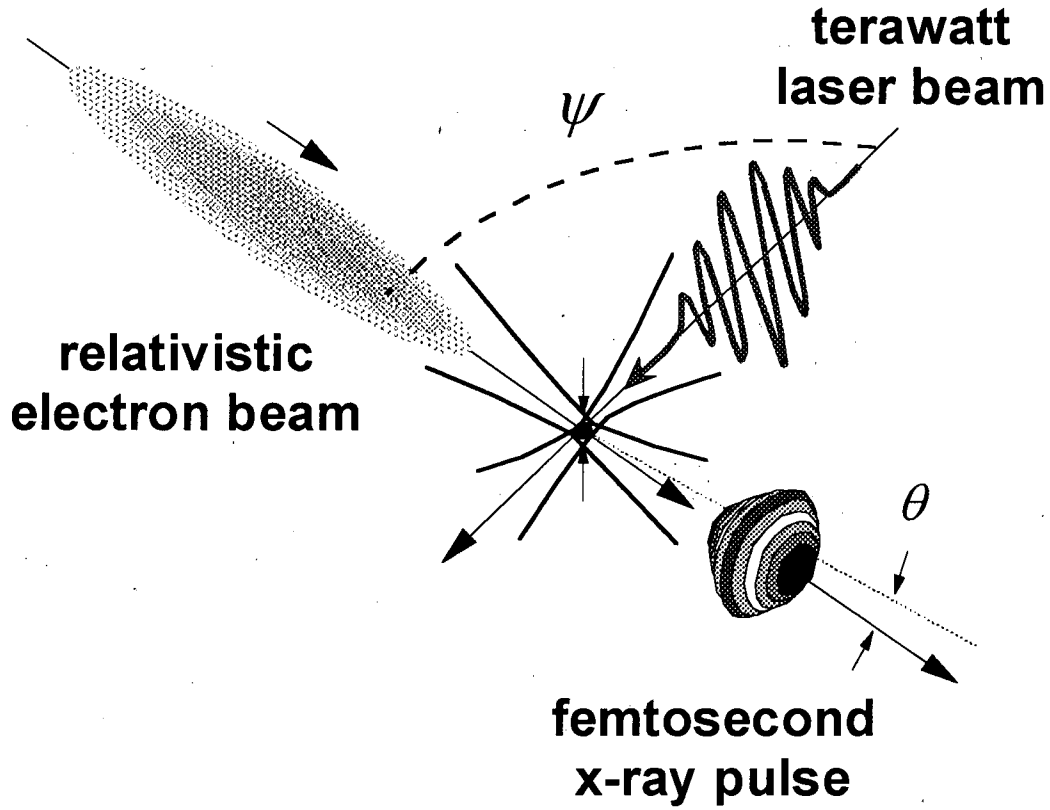
Figure 2.1: Thomson scattering x-ray source.

incident upon relativistic electrons elastically scatter off of them, giving the scattered

photons more energy and taking a negligible amount of energy from the electrons. The

flux of scattered photons, $F_{scattered}$, is given by

$$F_{scattered} = I_{laser} N_{electron} \sigma_T \qquad (2.1)$$

where I_{laser} is the incident photon intensity, $N_{electron}$ is the number of electrons that interact

with the photons, and $\sigma_T = 6.65 \times 10^{-25}$ cm^2 is the Thomson scattering cross-section. The

laser photon intensity is determined by

$$I_{laser} \approx \frac{N_{laser}}{A_{laser} \tau_{laser}} = \frac{U_{laser}}{(\hbar \omega_{laser}) A_{laser} \tau_{laser}} \qquad (2.2)$$

where N_{laser} is the total number of photons in the laser pulse, τ_{laser} is the full-width at half-

maximum (FWHM) laser pulse duration, A_{laser} is the area of the focused laser beam (using the FWHM beam diameter), U_{laser} is the total laser pulse energy, and $\hbar\omega_{laser}$ is the laser photon energy. To determine the number of electrons participating in the scattering process, let us consider the right angle geometry ($\psi = 90°$ in Figure 2.1), since that is the scattering geometry chosen for our femtosecond x-ray source. For a laser focal spot smaller than (or comparable to) the electron beam focal spot size, the number of electrons undergoing Thomson scattering is given by

$$N_{electron} \approx n_{electron} A_{laser} w_{electron} = n_{electron} A_{laser} \left(c\tau_{transit} \right) \tag{2.3}$$

where $w_{electron} = c\tau_{transit}$ is the electron beam diameter (FWHM), $\tau_{transit}$ is the transit time of the laser pulse across the electron beam diameter (the laser cuts a diagonal path across the electron beam, since the relativistic electrons travel at a velocity $v_{electron} \approx c$), and

$$n_{electron} \approx \frac{N_{total}}{A_{electron} \, l_{electron}} = \frac{N_{total}}{A_{electron} \left(c\tau_{electron} \right)} \tag{2.4}$$

is the electron density in the bunch, where N_{total} is the total number of electrons in the bunch, $A_{electron}$ is the area of the focused electron beam (using the FWHM beam diameter), and $l_{electron} = c\tau_{electron}$ is the electron bunch length (FWHM), where $\tau_{electron}$ is the electron bunch duration (FWHM). Gaussian spatial and temporal profiles are assumed for the electron bunch. The number of scattered photons is given by $N_{scattered} = F_{scattered} \, \tau_{laser}$, which becomes upon substitution

$$N_{scattered} \approx n_{electron} N_{laser} w_{electron} \sigma_T = \frac{N_{laser} N_{total}}{A_{electron}} \frac{\tau_{transit}}{\tau_{electron}} \sigma_T \, . \tag{2.5}$$

Note that for a laser beam diameter less than $w_{electron}$, $N_{scattered} \propto 1/ w_{electron}$ and is independent of the laser focal spot size. Because the momentum of the relativistic

electrons is much larger than the momentum of the photons, the scattered photons essentially follow the trajectory of the electrons. This leads to a highly directed beam of photons upshifted to x-ray energies.

Another description of the source is the undulator picture [30]. In this picture, the electric field of the laser pulse serves as an undulator for the relativistic electrons. As the relativistic electrons are caused to change their trajectory by a single cycle of the electric field of the laser (the magnetic field of the laser has a negligible effect for laser intensities considered here), they emit a broad range of radiation due to the acceleration they undergo [47]. As shown schematically in Figure 2.2, with repeated accelerations caused by the periodic nature of the laser field, a large amount of radiation is generated in the direction of propagation of the electron beam. For relativistic electrons traversing a magnetic undulator, a measure of the amplitude of oscillation of the electrons caused by the periodic magnetic field, and therefore the flux of x-rays generated, is the deflection parameter, K [30]. Using the equivalent magnetic field seen by the electrons due to the electric field of the laser pulse, and equivalent deflection parameter can be obtained, given by

$$K_{eq} = a_0 = \frac{e\mathcal{E}_o \lambda_{laser}}{2\pi mc^2} \tag{2.6}$$

where e is the charge of the electron, $\mathcal{E}_0$ is the peak electric field of the laser pulse, λ_{laser} is the wavelength of the laser pulse, and mc^2 is the electron rest mass energy. The equivalent deflection parameter can be regarded as the amount of energy gained by an electron in the presence of the electric field of the laser over a laser wavelength relative to the rest mass energy of the electron (see Appendix A). It can also be thought of as the ponderomotive

potential of the laser field relative to the rest mass energy of the electron. When $K_{eq} \sim 1$,

relativistic effects due to the electric field have to be taken into account. K_{eq} is also known

as the normalized vector potential (or the dimensionless laser strength parameter), a_0,

which is a measure of the strength of the electromagnetic field of the laser pulse. In the

following, let $K = K_{eq}$, as we are concerned with Thomson scattering here.

electron angular excursion   emitted radiation cone

$$\theta \sim \frac{1}{\gamma}$$

$$\theta_{e,max} \approx \frac{K}{\gamma}$$

undulator

$$\theta \sim \frac{1}{\gamma}$$

$$\theta_{e,max} \leq \frac{1}{\gamma}$$

wiggler

$$\theta \gg \frac{1}{\gamma}$$

$$\theta_{e,max} \gg \frac{1}{\gamma}$$
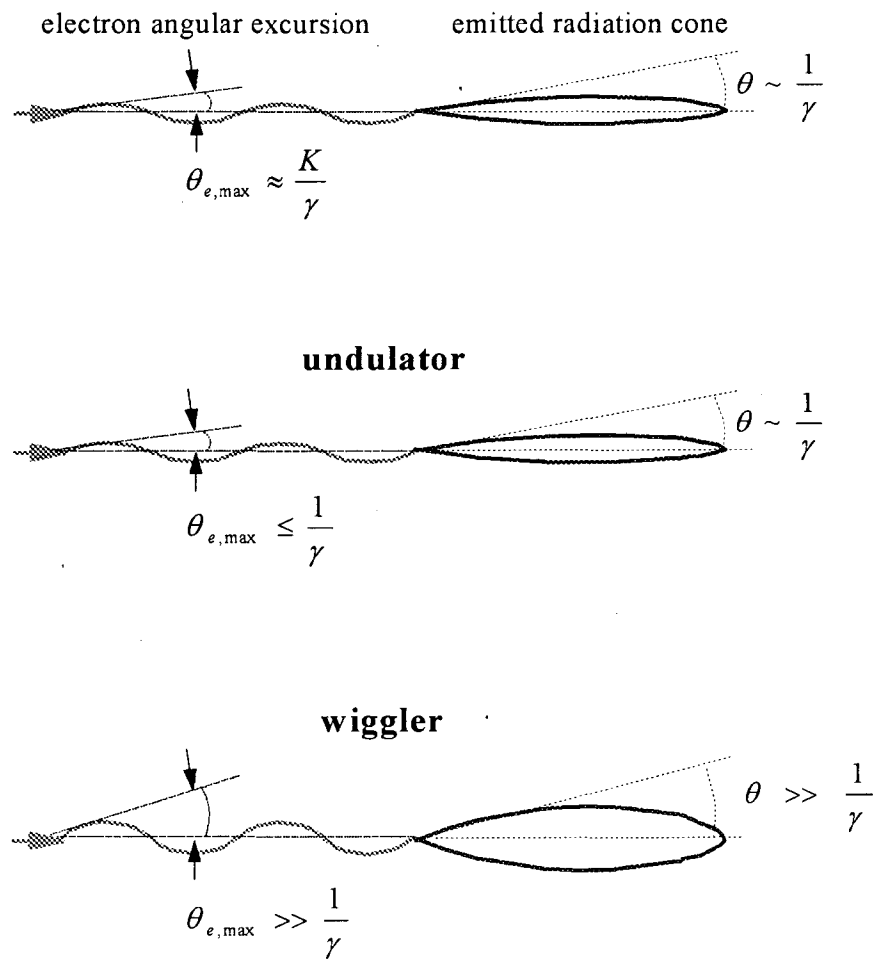
Figure 2.2: Differences between wiggler and undulator radiation.

Again referring to Figure 2.2, when $K < 1$, the electrons undergo a small angular

12

excursion relative to the emission angle of the radiation [47]. The radiation emitted per oscillation adds coherently, and is emitted in a narrow cone with emission angle $\sim 1/\gamma$, where γ is the energy of the electrons relative to the electron rest mass energy. Radiation emitted in such a manner is known as undulator radiation. If the deflection parameter is large ($K \gg 1$), the ponderomotive potential is large enough for the acceleration caused by the laser to be relativistic. This causes the angular excursion of the electrons to be so large that the radiation emitted can be viewed as the addition of radiation from a number of bend magnets [47]. The radiation is emitted in a larger emission angle than $1/\gamma$, due to the large excursion of the electrons. This is known as wiggler radiation. The wiggler flux is higher than for undulator radiation, but the radiation is broadband. For our source, $K < 1$, so that the undulator picture is valid and a narrow spectrum is expected.

Perhaps the most intuitive description of the x-ray source is the Thomson scattering picture [33, 48, 49], where the scattering is viewed in the rest frame of the electrons (i.e. the frame of reference moving with the relativistic electrons). In this frame of reference, the electrons see the incident laser radiation as higher frequency radiation, due to the relativistic Doppler shift. In the Thomson scattering geometry shown in Figure 2.1, the frequency of the laser light seen by the electrons is given by

$$\omega' = \gamma \left(1 - \beta \cos\psi\right)\omega_{laser} \tag{2.7}$$

where the relativistic parameter β is defined as the velocity relative to the speed of light

$$\beta = \frac{v}{c} = \sqrt{1 - \frac{1}{\gamma^2}} \approx 1 - \frac{1}{2\gamma^2} \tag{2.8}$$

with the approximation being valid for highly relativistic electrons ($\gamma \gg 1$). For electron and laser photon energies needed to produce hard x-rays, the photon energy in the rest

13

frame of the electron is much less than the rest mass of the electron. When this relatively low energy radiation is scattered by the electrons, elastic or Thomson scattering occurs. The electrons scatter the radiation in the usual dipole pattern in this frame of reference. As schematically shown in Figure 2.3, this dipole radiation pattern is once again Doppler shifted when viewed in the lab frame. Using the relativistic Doppler shift relationship, the frequency of the Thomson scattered radiation in the lab frame has the angular dependence given by

$$\omega = \frac{1}{\gamma(1 - \beta \cos \theta)} \omega' = \left(\frac{1 - \beta \cos \psi}{1 - \beta \cos \theta} \right) \omega_{laser}.$$ (2.9)

Due to the relativistic angular transformations, the dipole emission pattern of the Thomson scattered radiation seen in the rest frame of the electron becomes highly collimated along the electron beam propagation direction when viewed in the lab frame. The highly collimated nature of the radiation can be understood by considering the angular extent of the dipole emission pattern, and obtaining the corresponding angular extent in the laboratory frame using any of the relativistic angular transformation relations (see Figure 2.3). One of these angular transformations is given by

$$\sin \theta = \frac{\sin \theta'}{\gamma(1 + \beta \cos \theta')}$$ (2.10)

where the primed angles are measured in the rest frame of the electron. Equation 2.10 clearly shows that $\sin \theta$ has a maximum of $\sim 1/\gamma$, and therefore for highly relativistic electrons ($\gamma \gg 1$), $\sin \theta \approx \theta \sim 1/\gamma \ll 1$.

Because the x-rays are limited to small angles θ, one may make some simplifying approximations. For small angles $\theta \sim 1/\gamma \ll 1$,

relativistic Doppler shift

$$\omega = \frac{1}{\gamma(1 - \beta \cos\theta)}\omega'$$

rest frame of the electron

dipole radiation

ω'

laboratory frame

$V_{electron}$ x-rays

θ

$V_{electron} \sim c$

relativistic angular transformation

$$\sin\theta = \frac{\sin\theta'}{\gamma(1 + \beta\cos\theta')}$$

electron rest frame

θ'

laboratory frame
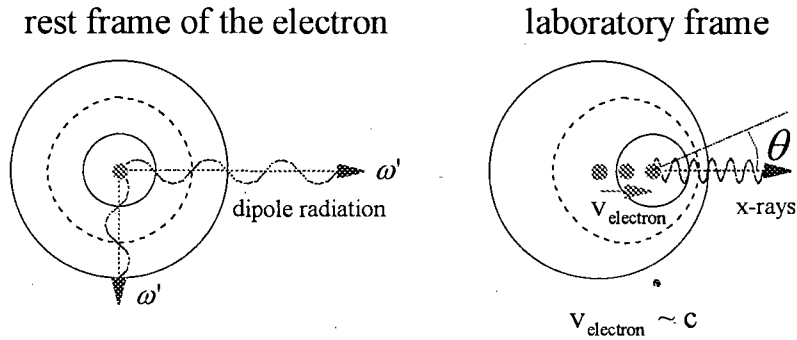
$\theta \sim \frac{1}{\gamma}$
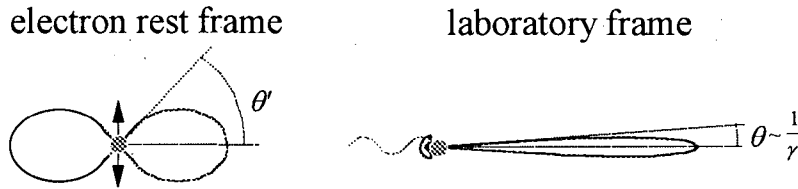
Figure 2.3: Relativistic transformations.

$$\cos\theta \approx 1 - \frac{\theta^2}{2} \qquad (2.11)$$

which, upon substitution into Equation 2.9, using Equation 2.8 for β, and dropping higher

order terms, yields the expression for the energy of the emitted radiation by Thomson

scattering (see Appendix A):

$$E = \hbar\omega = 2\gamma^2 E_{laser}\left(\frac{1 - \cos\psi}{1 + \gamma^2\theta^2}\right) \qquad (2.12)$$

where $E_{laser} = \hbar\omega_{laser}$ is the laser photon energy, ψ is the interaction angle between the

electron and laser beams, and θ is the x-ray emission angle relative to the electron beam

trajectory (see Figures 2.1 and 2.3).

The number of photons scattered per unit solid angle in the lab frame can be

obtained by assuming Thomson scattering in the rest frame of the electron, and

transforming the dipole distribution using the relativistic angular transformation into the

lab frame. With the electric field polarization of the laser perpendicular to the electric field

trajectory, the theory of magnetic undulators may be directly transferred to describe the

radiation resulting from Thomson scattering off of relativistic electrons [48]. Using the

definition of angles relative to the electron beam propagation direction and the laser

electric field direction shown in Figure 2.4 (for $\psi = 90°$), the Thomson scattered x-ray

photon distribution (both x-ray polarizations) in the lab frame is given by [48]

$$\left.\frac{dn}{d\Omega}\right|_1 = 2\alpha K^2 \gamma^2 N_u \chi^2 \left[\frac{1}{2} + \chi(\chi - 1)(\cos 2\phi + 1)\right] \qquad (2.13)$$

where α is the fine structure constant, N_u is the number of periods in the laser pulse, ϕ is

the azimuthal angle measured relative to the laser electric field polarization, and

$$\chi = \frac{E}{E_0} = \frac{1}{1 + \gamma^2 \theta^2} \qquad (2.14)$$

as obtained from Equation 2.12, where

$$E_0 = 2\gamma^2 E_{laser}(1 - \cos\psi) \qquad (2.15)$$

is the maximum energy of the scattered photons. Note that Equation 2.13 is valid for any

incident angle ψ, as long as the electric field vector of the laser beam is perpendicular to

the propagation axis of the electron beam. The angular dependence changes when the

electric field has a component along the electron beam trajectory, and no radiation is

emitted on-axis if the electric field is aligned with the axis of trajectory of the electron beam (for $K \leq 1$).

For this undulator-like radiation ($K \leq 1$), at each angle θ, the bandwidth of the radiation is determined by N_u, i.e. the number of oscillations that the electrons undergo. Due to the angle dependent Doppler shift (see Figure 2.3), the largest Doppler shift occurs along the relativistic electron trajectory. As a result, the shortest wavelength (highest photon energy) x-rays are generated along the propagation axis of the electron ($\theta = 0$), and longer wavelength components of the x-ray beam are emitted at larger emission angles θ. Because of the relativistic angular transformations (see Figure 2.3), most of the x-ray photons are in a small cone around the axis of trajectory of the electron.
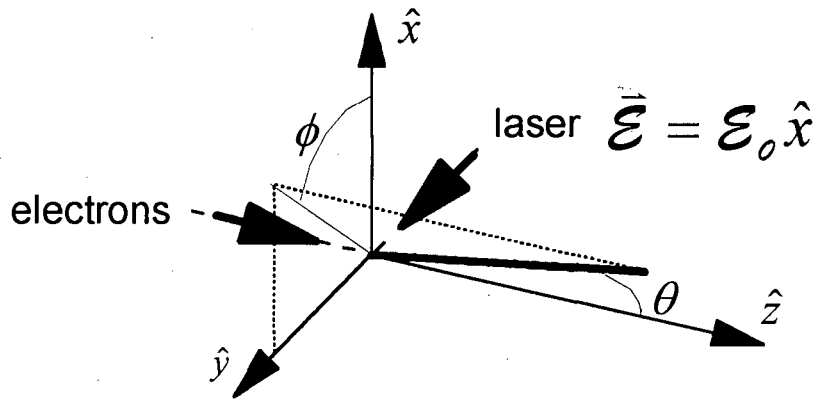
Figure 2.4: Right-angle Thomson scattering geometry.

Electron beam emittance effects

As described above, the angle-dependent Doppler shift causes the scattered x-ray wavelength to be angle dependent. This angular correlation between x-ray wavelength (or energy) and angle relative to the electron beam propagation direction is less apparent for an electron beam with a large emittance. Electron beam emittance is the distribution in

spatial and angular coordinates (relative to the electron beam propagation axis) that the electrons occupy (see Figure 2.5). Because electron beams have finite emittance, a large spread in angles (electron trajectories) results when the electron beam is focused to a small spot size. For a distribution of angles that is comparable to the angular extent of x-rays emitted from single electrons ($\theta \sim 1/\gamma$), the direct correlation between x-ray wavelength and angle will be less apparent for the ensemble of electrons. In this case, a convolution between the Doppler shifted radiation pattern and the distribution of electron trajectories yields a spectrum that is relatively broad band throughout the angular extent of the x-ray beam [33]. However, the general feature of having longer wavelengths at larger emission angles relative to the electron beam trajectory is still valid.

Electron Beam Emittance
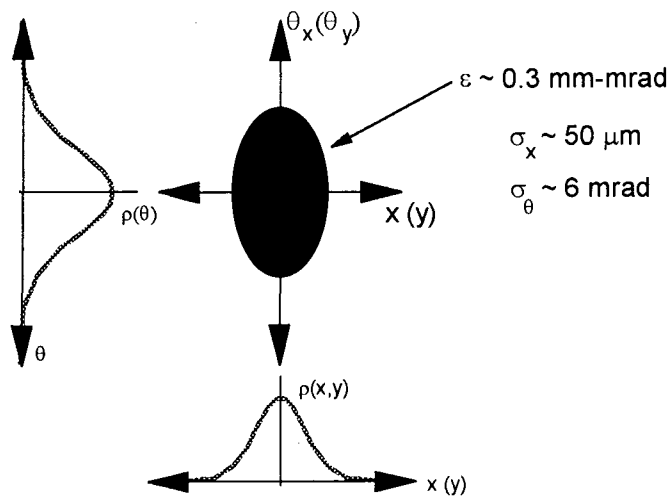
Figure 2.5: Electron beam emittance.

To account for electron beam emittance effects, one can assume that the number of electrons in the bunch contributing to Thomson scattering, $N_e = N_{electron}$ (given by Equation 2.3 in the right angle geometry), has a distribution of trajectories at the focus

given by $P_e(\theta)$. Due to this distribution of trajectories, at a given observation point these electrons tend to contribute photons with a broader range of energies than in the single electron case. The resulting photon distribution is obtained by convolving the electron trajectory distribution with the single electron photon distribution (Equation 2.13). To be more precise, we define the solid angle over which the x-rays are observed to be $d\Omega_{obs} = \sin\theta_{obs}\, d\theta_{obs}\, d\phi_{obs}$ ($\approx \theta_{obs}\, d\theta_{obs}\, d\phi_{obs}$, since $\theta_{obs} \sim 1/\gamma \ll 1$). The number of photons in the observation solid angle becomes

$$\frac{dn}{d\Omega_{obs}} = \frac{dn}{d\Omega}\bigg|_1 \otimes P_e(\theta,\phi) = 2\alpha K^2 \gamma^2 N_u N_e$$

$$\int_0^{2\pi}\int_0^{\pi} \chi_1^2\left[\frac{1}{2} + \chi_1(\chi_1 - 1)(\cos 2\phi'+1)\right] P_e(\theta_1 - \theta_{obs}, \phi'-\phi_{obs})\sin\theta_1 d\theta_1 d\phi' \quad (2.16)$$

where $\chi_1 = 1/(1+\gamma^2\theta_1^2)$. Angular integration is converted (see Figure 2.6) from the ϕ_1 frame (referenced at the observation point) to the ϕ' frame (referenced at the electron under consideration) to account for the proper ϕ dependence of the single electron photon distribution (see Equation 2.13).

Due to the direct correlation between energy and angle away from the electron trajectory, integration along a path of constant θ_1 is necessary in order to obtain the number of photons of a given energy at the observation point. The relative angle θ_1 is determined by the photon energy under consideration using Equation 2.14. Solving for the angle in terms of the photon energy, the radius of the path of integration for constant energy (see Figure 2.6) becomes

$$\theta_1 = \theta' = \theta_x = \frac{1}{\gamma}\sqrt{\frac{E}{E_0} - 1}\,. \quad (2.17)$$

19

Taking the derivative of Equation 2.17, one can express the angular integration in

Figure 2.6: Defining the constant energy path of integration. The angle θ from the electron beam axis (z) corresponds to a distance on the x-y plane at a fixed distance from the generation point.

Equation 2.16 in terms of an integration over energy. Solving for dE, the differential form of Equation 2.17 becomes

$$dE = -\frac{2\gamma^2 \chi^2}{E_0}\theta_1 d\theta_1 . \tag{2.18}$$

The negative sign merely indicates the inverse relationship between x-ray photon energy and angle from the electron trajectory, and can be dropped for our purposes. Using $\sin\theta_1$ $d\theta_1 \approx \theta_1\, d\theta_1$ (since $\theta_1 \sim 1/\gamma \ll 1$), dropping the integration over θ_1 (since we are considering constant energy), and using Equation 2.18, Equation 2.16 becomes [33]

$$\frac{d^2 n}{dEd\Omega_{obs}} = \alpha K^2 N_u N_e \frac{1}{E_0}\int_0^{2\pi}\left[\frac{1}{2} + \chi(\chi - 1)(\cos 2\phi' + 1)\right]P_e(\theta)d\phi' . \tag{2.19}$$

This is a convolution of the electron trajectory distribution, $P_e(\theta)$, with the single electron photon distribution given by Equation 2.13, using a coordinate system (θ', ϕ'), where now

$\theta_1 = \theta' = \theta_x$ (see Figure 2.6). In this coordinate system, the angles are shifted by the observation angles $(\theta_{obs}, \phi_{obs})$ so that only those components of the electron beam which yield a given energy at the observation point are considered. This provides a relationship between the convolution and spatial coordinate systems given by [33],

$$\theta^2 = \theta_{obs}^2 + \theta'^2 - 2\theta_{obs}\theta'\cos(\phi' - \phi_{obs}) \qquad (2.20)$$

where $\theta' = \theta_1 = \theta_x$ (given by Equation 2.17) is determined by the Thomson scattered photon energy under consideration. As shown in Figure 2.6, Equation 2.20 is obtained by using simple trigonometry.

For a distribution of electron trajectories greater than the angular extent of undulator radiation from single electrons ($\sim 1/\gamma$), the x-ray energy spectrum can become significantly broadened. This results in a more uniform distribution of photon energy over the angular spread of the beam. A uniformly distributed spectrum may be useful for applications such as Extended X-ray Absorption Fine Structure (EXAFS) experiments, where having a range of photon energies around the absorption edge of an atomic species is necessary. However, this broadening due to electron beam emittance causes more of the useful x-rays to be spread out over a larger emission angles, causing an overall reduction in source brightness.

Experimental Setup

Although conceptually simple, generating x-rays via right angle Thomson scattering is not trivial and requires a large amount of apparatus. Two major components of the Thomson scattering x-ray source are a terawatt laser system, needed to produce

ultrashort, high-intensity laser pulses, and a linear accelerator (linac), needed to generate

pulses of relativistic electrons with a large amount of charge per pulse. Large numbers of

electrons and photons are necessary in order to overcome the small Thomson scattering

cross-section and generate a reasonable number of x-ray photons. Timing and

synchronization electronics are necessary to ensure the temporal overlap of the electron

and laser pulses. Diagnostics are required to ensure that spatial overlap between the small

laser and electron beam foci is achieved. Finally, x-ray diagnostics are necessary to

characterize the ultrashort x-ray pulses generated.

Terawatt laser system

Passively modelocked lasers are now routinely used to generate ultrashort laser

pulses [50]. The first femtosecond modelocked lasers were based on dye gain media, and

relied upon the saturable gain in the gain media in conjunction with the saturable loss in a

saturable absorber placed in the laser cavity [1, 2]. Saturable gain tends to shorten the

trailing edge of the laser pulse traversing the laser cavity, and saturable loss tends to

shorten the leading edge of the pulse. With appropriate compensation of linear dispersion

of the material in the cavity, this process shortens the laser pulse each round trip. The

pulse shortening continues until higher-order dispersion that cannot be compensated

determines the pulse duration.

More recently, femtosecond modelocked lasers based on solid state gain media

have been developed [50]. The pulse shortening mechanism for these lasers is known as

Kerr lens modelocking. During the Kerr lens modelocking process, laser pulse shortening

occurs because the cavity is arranged in such a way that the cavity loss is reduced for a

mode in which self-focusing in the gain medium occurs. Thus, in such a cavity, a higher

intensity, ultrashort laser pulse is preferred over a continuous wave. As in the case of

modelocked dye lasers, material dispersion in the gain medium must be compensated by

some negative dispersion element in order to achieve the shortest pulses. Schematically

shown in Figure 2.7 is the cavity of the Titanium doped sapphire (Ti:sapphire)

modelocked laser used in our terawatt laser system.
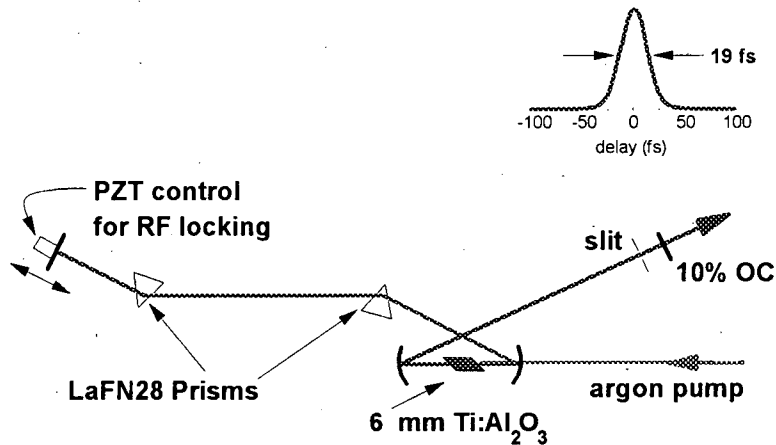
Figure 2.7: Ti:Sapphire based Kerr lens modelocked laser.

The high damage threshold and large gain bandwidth of some solid state media

(e.g. Ti:sapphire) allows for the amplification of ultrashort pulses to high pulse energies

[51, 52]. To amplify ultrashort pulses to the terawatt level, the intensity of the laser pulse

must be reduced in the gain medium to avoid nonlinear damage due to self-focusing. In the

past, increasing the laser diameter reduced the laser beam intensity, which required very

large and expensive crystals. Now, a technique known as chirped-pulse amplification

(CPA) is routinely used to avoid self-focusing of the amplified pulses in the gain medium

[53]. By introducing a linear chirp (i.e. a direct correlation between the laser frequency

and temporal profile) on the pulse, thereby temporally stretching the pulse, the intensity in

the gain medium is reduced. This permits amplification of ultrashort laser pulses to very high pulse energies in relatively small and inexpensive crystals. The amplified laser pulses are then recompressed by sending them through an optical element that introduces the opposite linear chirp on the pulse, resulting in a high-energy, ultrashort laser pulse. The laser pulse duration becomes limited by higher-order dispersion terms, some of which can be reduced by using appropriate tricks [54, 55]. Laser pulses with peak power in the terawatt range are now routinely generated, and laser pulses with petawatt peak power are beginning to be realized [51, 52, 56].

Our terawatt laser system is similar to one designed by C. LeBlanc et al. [57], and is shown schematically in Figure 2.8. It is based on a home-built Ti:Sapphire modelocked laser following the design of H. C. Kapteyn and M. M. Murnane, and has generated pulses as short as ~ 20 fs. Individual pulses from the modelocked laser are selected at a 10 Hz rate using a Pockel's cell. The triggering of the Pockel's cell is synchronized to both the pulses from the Ti:Sapphire modelocked laser and from the frequency doubled Nd:YAG laser (10 Hz repetition rate) which pumps the amplifiers. A synchronization circuit performs this task as follows: 1) the signal from modelocked laser pulses incident on a photodiode is used as a clock, 2) counters are set to put out pulses at a 10 Hz repetition rate, based on a fixed number of clock cycles, 3) appropriately spaced pulses are generated – one to trigger the Nd:YAG flashlamps, and one to trigger the Nd:YAG Q-switch and the Pockel's cell (~ 260 μs after the flashlamp trigger), and 4) a delay generator is used for fine individual adjustments of the triggering of the Q-switch and the Pockel's cell.
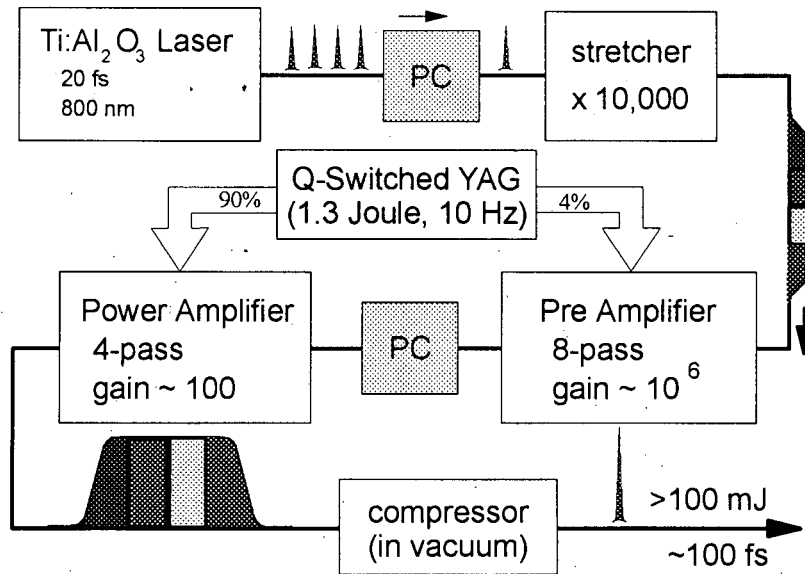
Figure 2.8: Terawatt laser system.

These laser pulses selected by the Pockel's cell are sent through a pulse stretcher

to temporally stretch the pulse by introducing positive dispersion. In order to provide

significant positive dispersion, a grating pair with a 1:1 telescope in between is used [58].

This combination, with the gratings placed within the focal length of the lenses, is reduced

in size by using reflective optics (parabolic mirror) for the telescope lens and using a

mirror at the symmetry plane to provide the other half of the lens and grating pair (see

Figure 2.9). A parabolic mirror is used to reduce spherical aberrations that lead to higher

order dispersion. The stretcher lengthens the pulse duration from ~ 20 fs to ~ 200 ps -

about 10,000 times longer. The stretched pulse duration was verified by using a fast

photodetector (Picometrix) and a sampling oscilloscope.

input ~40 fs

output ~250 ps

1800 g/mm grating

parabolic reflector
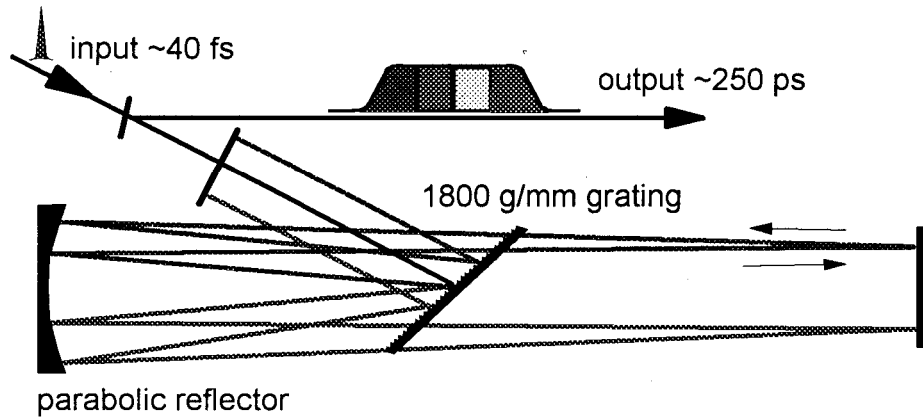
Figure 2.9: Pulse stretcher using all reflective optics.

After the stretcher, the long laser pulse is sent through two amplification stages.

The preamplifier is a multi-pass amplifier with 8 passes in a unique bow-tie configuration,

as shown in Figure 2.10. On each pass through the Ti:Sapphire crystal gain medium, the ~

2mm diameter beam is focused by a 50 cm mirror onto the crystal, and then recollimated

after passing through the gain medium. The amplifier gain medium is pumped by a fraction

of the output (~ 5 mJ out of ~ 1.3 J per pulse) of a frequency doubled (532 nm) Nd:YAG

laser (Spectra-Physics, GCR 350). This light is relay imaged from the Nd:YAG laser

amplifier rod to the gain medium to a spot size of ~ 1 mm diameter in order to: 1) have the

appropriate pump fluence, and 2) image a good spatial profile onto the gain medium. The

preamplifier increases the laser pulse energy from ~ 1 nJ to ~ 2 mJ - about 10^6 times

greater.

After the preamplifier, the amplified pulses are then sent through another Pockel's

cell to reduce amplified spontaneous emission (ASE). ASE that propagates from the

power amplifier into the preamplifier and eventually back to the modelocked laser can stop

the modelocking process. After the Pockel's cell, the pulses then go through an expanding

telescope to increase the beam size to ~ 4 mm diameter, as well as to control the divergence of the beam going into the power amplifier. It is necessary to have the beam slightly diverging going into the power amplifier in order to correct for thermal lensing in the Ti:Sapphire crystal. Thermal lensing is caused by the thermal expansion of the crystal due to the large amount of power absorbed while it is being pumped.
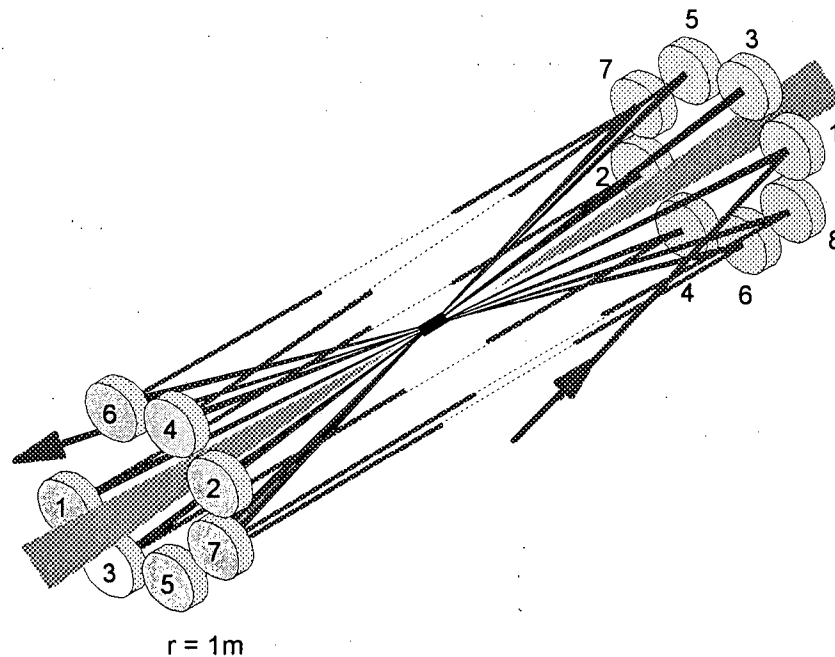
Figure 2.10: Novel preamplifier configuration in the terawatt laser system.

The expanded beam is then sent through 4 passes in the power amplifier, which is pumped by the majority of the Nd:YAG output. As shown in Figure 2.11, the pump beam is split into two beams, each of which is relay imaged to a spot size ~ 5 mm in diameter, and which pumps both sides of the Ti:Sapphire gain medium. The amplified beam goes through each pass approximately collimated (slightly diverging). After 4 passes, the beam

has up to 200 mJ per pulse in a reasonable spatial mode. Higher pulse energy can be extracted, but the mode becomes significantly shaped by the astigmatic beam profile of the Nd:YAG laser. The poor Nd:YAG beam profile is mainly due to poor collimation of the laser output, resulting in poor phase-matching in the frequency-doubling KDP crystal. The elliptical Nd:YAG laser beam mode can be compensated by offsetting the two pump beams. This results in a more uniform gain volume and a better amplified beam mode, at the cost of reduced extraction efficiency.
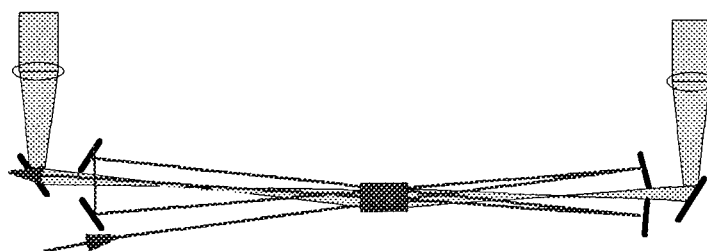
Figure 2.11: Four-pass power amplifier.

After the power amplification stage, the beam is once again expanded using a telescope to ~ 30 mm diameter before going into the compressor. This expansion is necessary to avoid damage to the gratings in the compressor (~ 200 mJ/cm^2 damage threshold). Schematically shown in Figure 2.12, the compressor is basically a pair of gratings that have almost the same angle of incidence as the stretcher grating. The separation of the gratings and the incident angle of the gratings are adjusted to reduce the amount of dispersion introduced in the laser beam from the pulse stretcher as well as from the gain medium and lenses (material dispersion). After compression, the result is an amplified laser beam that has a very high peak intensity (~ 1 terawatt). Because of this high intensity, the compression is performed under vacuum to eliminate laser beam filimentation and breakup due to self-focusing that would result from the propagation of

28

the terawatt laser pulse through air.

input ~ 250 ps   output ~ 100 fs

1800 g/mm
grating

1800 g/mm
grating
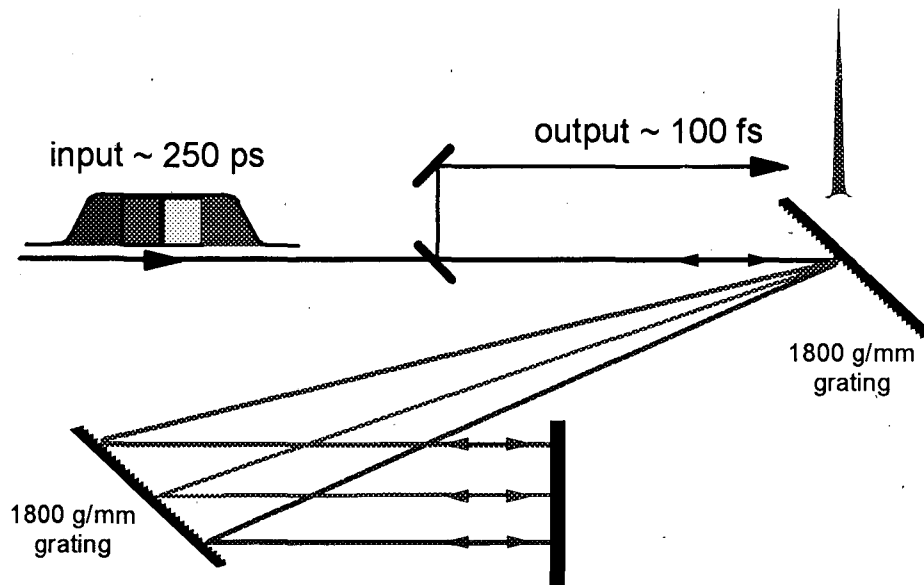
Figure 2.12: Pulse compressor.

Linear accelerator

To generate relativistic electrons, we use the linear accelerator (linac) at the

Advanced Light Source (ALS) in between fill periods. This linac can produce 50 MeV

electron bunches with ~ 1 nC of charge at a repetition rate from 1 Hz up to 5 Hz. These

pulses are transported and focused into the Beam Test Facility (BTF) through a series of

bend magnets and quadrupole magnets (BTF line), and are ultimately focused to ~ 90 μm

(FWHM) in diameter at the interaction point. Efficient transport of charge through the

BTF line to the interaction point is achieved and monitored by beam position monitors

(button-type RF pickup) and retractable phosphor screens [31]. Typically, about 80% of

the charge reaches the interaction point, with the rest generating background radiation due

to electrons scraping the walls of the vacuum transport line.
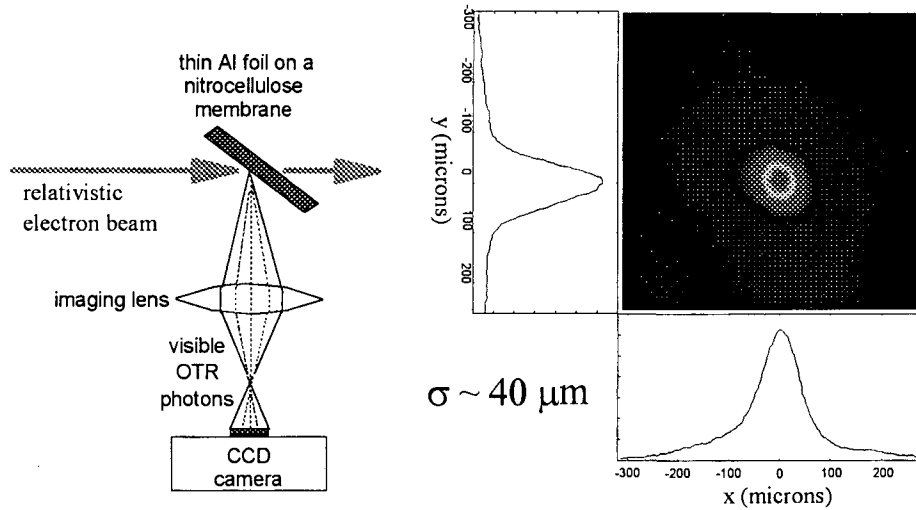
Figure 2.13: Optical transition radiation (OTR) electron beam profile diagnostic.

As the x-ray pulse duration in the right angle Thomson scattering geometry is determined by the transit time of the ultrashort laser pulse across the electron beam waist, the electron beam profile must be determined and monitored. To measure the electron beam waist at the interaction point, optical transition radiation (OTR) is utilized [31]. OTR is the emission of light as relativistic electrons encounter a change in dielectric constant. This radiation is proportional to the amount of charge in the electron beam, and therefore can be used to monitor the spatial profile of the beam at the focus. The OTR electron beam diagnostic is schematically shown in Figure 2.13, with a typical electron beam image at the focus.

Interaction apparatus

In order to generate x-rays via Thomson scattering, the laser and electron pulses

must be synchronized to within the electron pulse duration (~ 30 ps). To perform this

synchronization, the frequency of pulses emitted by the Ti:Sapphire modelocked laser is

synchronized to the 500 MHz RF used as the basis for the RF electronics used to drive the

- a phase-locked loop synchronizes the pulses
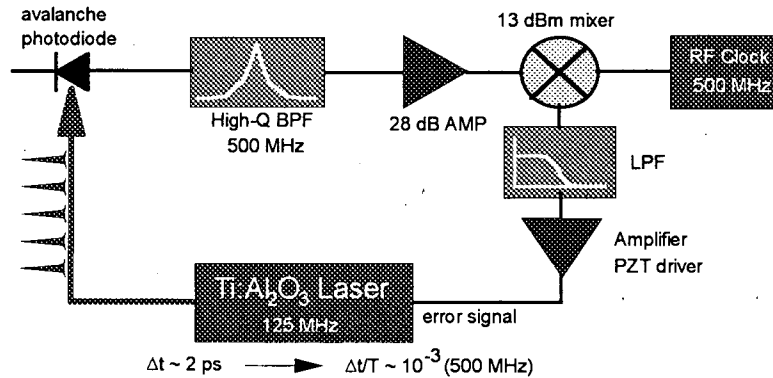
- less than ~ 2 ps timing jitter measured
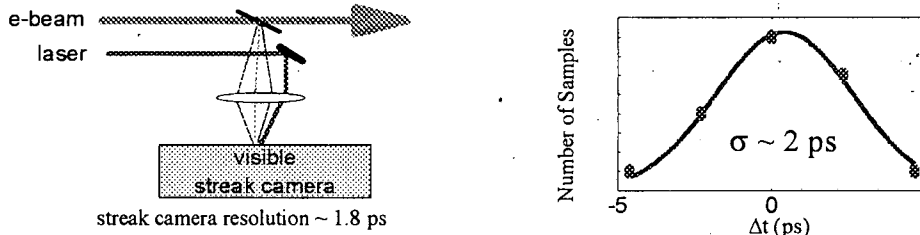
Figure 2.14: Synchronization of laser and electron pulses using a phase-locked loop.

linac. The synchronization is performed using a phase-locked loop [59] as follows: 1) the

signal from laser pulses detected on an avalanche photodiode is used to determine the

frequency of the laser pulse train (the cavity length of the laser is set to generate laser

pulses at a repetition rate of 125 MHz), 2) the fourth harmonic (500 MHz) of the

photodiode signal is mixed with the 500 MHz from the linac RF electronics in a RF mixer,

3) the difference frequency is used as feedback to control the voltage applied to a

piezoelectric stack attached to one of the end mirrors in the laser cavity, and 4) the

piezoelectric stack adjusts the cavity length to keep the laser repetition rate locked to the

500 MHz linac master oscillator. Schematically shown in Figure 2.14 are the RF

synchronization system and the optical streak camera measurements of OTR light and

laser light used to put an upper bound on the timing jitter.
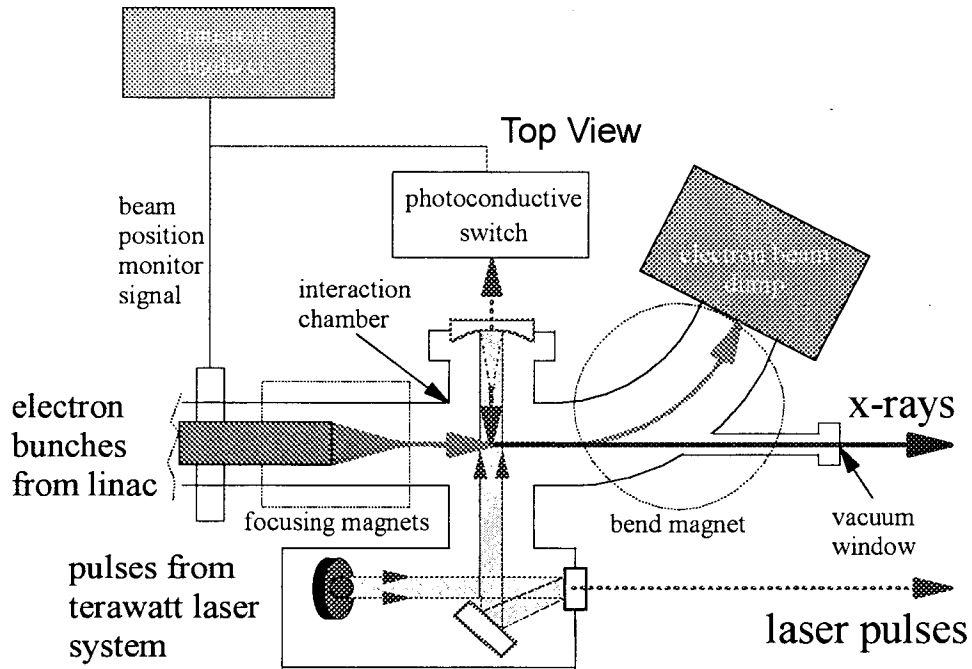
Figure 2.15: Beam Test Facility.

Not only do the electron and laser pulses have to be synchronized, but the

amplified laser pulses must be temporally overlapped with the electron bunches as well.

Temporal overlap of the electron and laser pulses is determined by using a fast

photodetector to determine the laser pulse arrival time at the interaction point, and a beam

position monitor (button-type RF pickup) is used to determine the electron pulse arrival

time. The laser beam first passes through the interaction point, then is reflected back and

focused by a focusing mirror to the interaction point. Leakage from this focusing mirror is

used to monitor the arrival of the laser pulse. By observing the two fast signals on a

transient digitizer (Tektronix SCD 5000), and knowing the difference in path lengths and signal arrival times (see Figure 2.15), the temporal overlap of electron and amplified laser pulses can be monitored.

In order to amplify the correct laser pulse that will overlap with the electron bunch at the interaction point, another level of synchronization is necessary. This synchronization involves triggering the Nd:YAG laser and the Pockel's cells when the linac generates an electron bunch (see Figure 2.16). Because it takes some time for the laser pulse to travel through the laser system and down into the interaction chamber, triggers that are generated before the firing of the linac (pre-triggers) are necessary to ensure that the amplified laser pulse has enough time to reach the interaction point when the electron bunch does. Fortunately, the booster ring at the ALS also requires pre-triggers for beam injection. The Utility trigger and the Anti-magnet pre-trigger (specially created to suit our needs) are combined through an OR gate, and are generated sufficiently early to be used to trigger the Nd:YAG flashlamps. The ~ 2 μs jitter in this trigger does not affect the performance of the Nd:YAG laser. The Injection Sync trigger is used to trigger the Q-switch and Pockel's cells. When these triggers arrive, the counters in the synchronization circuit (described in the terawatt laser system section above) reset, and the appropriate flashlamp and Q-switch triggers are output. The resulting amplified laser pulse can be adjusted to within ~ 8 ns (spacing between modelocked laser pulses) of arriving simultaneously with the electron bunch at the interaction point by means of a delay generator. To get within 2 ns, the laser has to be synchronized to the correct phase of the 500 MHz RF master oscillator. This is achieved by turning the RF synchronization circuit on and off until the appropriate phase is chosen. Finally, to achieve temporal overlap

33

within the electron bunch duration (~ 30 ps, FWHM), the bias voltage at which the 500 MHz RF master oscillator and the 500 MHz signal derived from the avalanche photodiode signal are synchronized can be adjusted. This adjustment is performed while monitoring the signals on the transient digitizer, and ultimately while monitoring the x-ray yield.
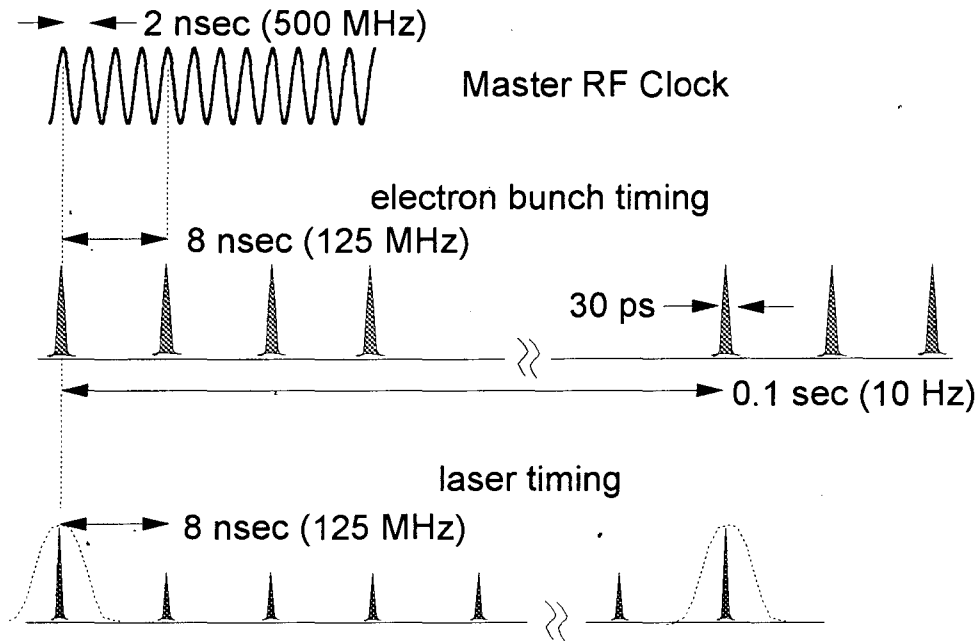
Figure 2.16: Laser and electron bunch timing.

Spatial overlap of the pulses is determined by sending unamplified laser pulses through one hole in an alignment cube, and by sending an alignment laser beam (HeNe laser) for the electrons through the orthogonal hole in the cube. The electron beam is aligned using beam position monitors and removable phosphor screens to ensure that the beam follows the trajectory of the alignment laser. The unamplified laser beam is sent through the orthogonal holes, and the reflected beam is sent back through the cube. The focused beam going back through the cube is imaged onto a camera to ensure the alignment of the focusing mirror.

X-ray diagnostics

When temporal and spatial overlap of the laser and electron pulses is achieved, x-ray pulses are generated. In order to verify that the characteristics of these x-ray pulses agree with theory, diagnostics are needed to measure quantities such as flux, divergence, and energy spectrum. The spatial profile of the x-ray beam is obtained by imaging the fluorescence created by the x-rays striking an x-ray phosphor screen (see Figure 2.17 a) [60]. Knowing the distance between the interaction point and the phosphor, the divergence of the x-ray beam can be obtained. Calibrating the number of fluorescent photons per x-ray photon using a calibrated radioactive source (^{129}I), the x-ray flux can also be determined. For x-ray photon energies around 30 keV, ~ 1 CCD count corresponds to 1 x-ray photon striking the phosphor.

To measure the energy spectrum of the x-ray pulse, a Ge detector is used in photon counting mode (see Figure 2.17 b). The pulse height of the voltage generated per photon in the detector can be calibrated to determine the x-ray photon energy. Because the detector operates in the photon counting mode, radiation shielding is essential to reduce the x-ray background in the Beam Test Facility. This is accomplished by placing a thick lead aperture in front of the detector (several lead bricks with ~ ½ " hole in the middle), and layers of lead bricks around the sides. For spectral measurements of the source, the x-ray flux is further reduced by using a long (~ 8 ") tantalum slit, ~ 200μm wide. This aperture and the detector are moveable, which permits the measurement of the spectrum of the source at different emission angles.

• calibration: ~ 1 CCD count per x-ray photon
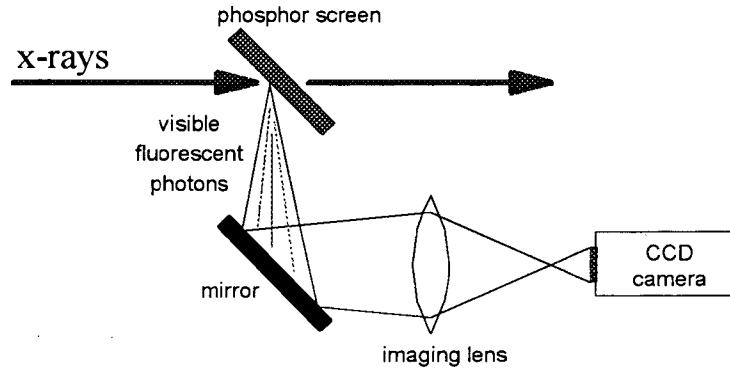
(a)
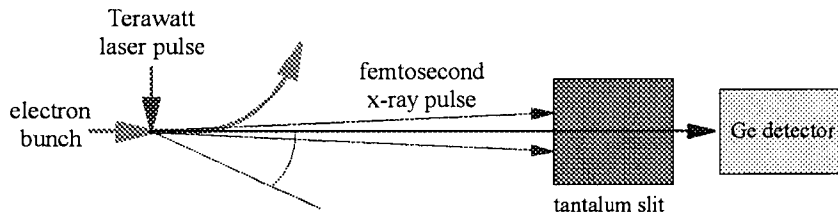
(b)

Figure 2.17: X-ray diagnostics: (a) phosphor imaging system, (b) Ge detector system.

Measured X-Ray Characteristics

When spatial and temporal overlap of the focused electron and laser pulses is

ensured and the pulses are synchronized, ultrashort x-ray pulses are generated by right

angle Thomson scattering. As described earlier, these x-ray pulses should be emitted in a

narrow cone, and the flux per pulse should be proportional to the overlap density of

electrons and photons. In this chapter, the experimentally measured beam characteristics

are described and compared to the Thomson scattering theory [33]. These measurements

were performed at the Center for Beam Physics Beam Test Facility at the Advanced Light Source.

Beam divergence and flux

If the electric field of the laser is not too strong, i.e. if $K = a_0 < 1$, then the undulator characteristics described in the Thomson scattering theory section are applicable. 800 nm, 100 mJ, 100 fs laser pulses focused to a 30 μm (FWHM) diameter spot at the interaction point were used to generate the x-rays. The focused laser intensity at the interaction point was $\sim 1.4 \times 10^{17}$ W/cm^2. This intensity corresponds to a normalized laser field strength of $a_0 = 0.25 < 1$. This indicates that the laser field is not strong enough to accelerate the electrons to relativistic velocities. Therefore, the Thomson scattering source produces an x-ray beam with undulator characteristics.

One method of measuring the x-ray beam divergence is to measure the beam profile at a known distance from the x-ray generation point (interaction point). As described in the previous chapter, we can measure the spatial profile of the x-ray beam by imaging the fluorescence from an x-ray phosphor. The phosphor used to measure the spatial profile was ~ 80 cm from the interaction point. The x-ray beam profile is elliptical, with horizontal and vertical beam sizes (FWHM) of ~ 12 mm and ~ 8 mm respectively (see Figure 2.18). This information yields a beam divergence of ~ 10 mrad.

As described in the Thomson scattering theory section, the divergence of the x-ray beam from an undulator-like source is expected to be $\sim 1/\gamma$. For the 50 MeV electrons used in the x-ray source, $\gamma \sim 97$. Thus, the expected divergence is ~ 10 mrad, which agrees with the experimentally measured divergence. Part of the asymmetry in the spatial profile

of the x-ray beam is due to the asymmetry in the dipole emission pattern in the rest frame of the electron. In the rest frame, due to the transverse nature of electromagnetic radiation, the scattered photon flux approaches zero as the propagation direction approaches the electric field vector of the laser. When viewed in the lab frame, this asymmetric distribution results in a photon distribution that is narrower along the laser electric field direction (vertical axis in Figure 2.18). This asymmetry is seen in the $\cos 2\phi$ term of Equation 2.13. In our case, the majority of the asymmetry is due to the asymmetric focusing of the electron beam [31]. Because a quadrupole magnet mainly focuses along one axis, a pair of quadrupole magnets is needed to focus the electron beam along two axes. The vertically focusing quadrupole magnet was ~ 1.5 times farther from the interaction point than the horizontally focusing one. To achieve a symmetric spot at the interaction point, the vertical beam divergence is ~ 1.5 times less than the horizontal beam divergence. The result is an x-ray beam that has an asymmetric beam profile, ~ 1.5 times larger horizontally (~ 12 mm) than vertically (~ 8 mm).

The x-ray flux is determined by integrating the number of fluorescent photons and using the calibrated number of CCD counts from fluorescent photons resulting per x-ray photon (~ 1 CCD count per x-ray photon at ~ 30 keV photon energy). The image x-ray pulse image shown in Figure 2.18 corresponds to ~ 5×10^4 photons with energies around 30 keV. These x-rays were generated from an electron beam with a focused diameter of ~ 90 μm (FWHM), which corresponds to an x-ray pulse duration of ~ 300 fs. The laser focal spot was imaged, and is estimated to be ~ 30 μm (FWHM), smaller than the electron beam diameter. Using the measured electron beam and laser beam diameters, the measured electron bunch charge and laser pulse energy, and the Thomson scattering cross section,

an estimate of the expected x-ray flux can be made. The number of photons in a 60 mJ pulse at 800 nm is ~ $(0.06 \text{ J})/((1.6 \times 10^{-19} \text{ J/eV})(1.5 \text{ eV/photon})) = 2.5 \times 10^{17}$ photons.
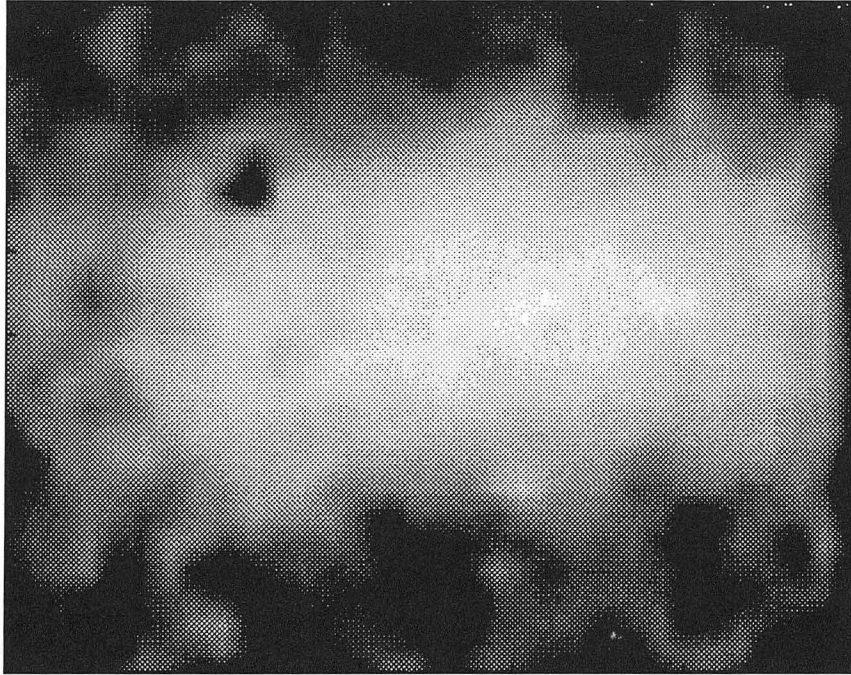
Figure 2.18: Spatial image of the Thomson scattered x-ray beam. The vertical axis is parallel to the electric field of the generating laser pulse.

The number of electrons in a ~ 1.3 nC pulse, is ~ $(1.3 \times 10^{-9} \text{ coulombs})/(1.6 \times 10^{-19}$ coulombs/electron$) = 8.1 \times 10^{9}$ electrons. From Equation 2.5, the estimated number of scattered laser photons per pulse for a 30 ps (FWHM) electron bunch focused to a ~ 90 μm (FWHM) diameter is ~ $(2.5 \times 10^{17})(8.1 \times 10^{9})(6.65 \times 10^{-25} \text{ cm}^2)(300 \times 10^{-15}$ sec$)/((\pi/4)(9 \times 10^{-3} \text{ cm})^2(30 \times 10^{-12} \text{ sec})) = 2 \times 10^{5}$ photons. This estimate is about a factor of 4 higher than the experimentally measured flux of ~ 5×10^{4} photons per pulse. Part of the discrepancy is due to the fact that some of the scattering events result in lower

energy photons in the lab frame, with laser photons losing energy to the electrons. Half of the scattering events should result in lower energy photons. Another factor contributing to the difference is the fact that significant absorption of x-rays with lower photon energy (~ 10 keV) occurs as the x-ray beam passes through the vacuum window (Lexan) and through air before hitting the phosphor.

Energy spectrum

Using a moveable slit and a Ge detector, the x-ray energy spectra can be measured at different angles of observation relative to the electron beam propagation axis. The angles of observation are in a plane perpendicular to the electric field of the laser used to generate the x-rays. The slit limits the angular acceptance of the Ge detector to 50 μrad perpendicular to the electric field of the laser, and 1 mrad parallel to the electric field of the laser. The measured spectra for three different emission angles are shown as crosses in Figure 2.19. The spectra are broad (~ 10% relative bandwidth) with the spectrum on axis having the narrowest bandwidth and the highest energy x-rays. The general trends in the spectra are that the peak shifts to lower energy, the spectra are broader, and the number of photons decreases with increasing emission angle. Using a quadrupole scan technique [32], the electron beam emittance is measured to be ~ 0.3 mm·mrad. With a focused beam diameter of ~ 50 μm (sigma), the angular divergence of the electron beam is ~ 6 mrad (sigma). Since the electron beam divergence is comparable to the x-ray beam divergence (~ $1/\gamma$ = 10 mrad), the x-ray spectrum is expected to be broadened.

Also shown in Figure 2.19 are the predicted spectra (solid curves). The predicted spectra are calculated using the measured electron beam emittance and results from the

Thomson scattering theory section of this chapter. These theoretical curves also take into account the x-ray absorption of the x-ray window (Lexan) used for the spectral measurements. The agreement is quite good, demonstrating that the source characteristics are well understood.
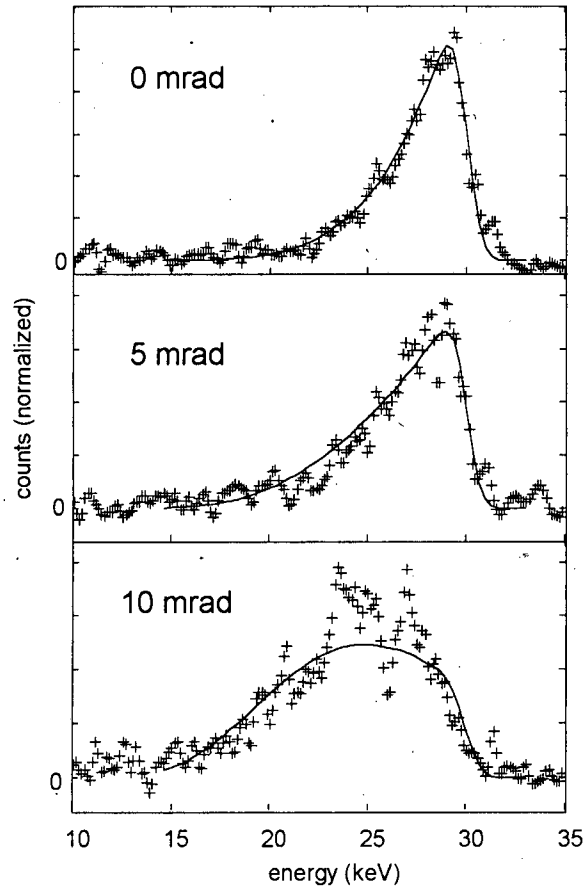
Figure 2.19: Normalized x-ray spectra at observation angles of 0 mrad, 5 mrad, and 10 mrad from the center of the beam.

Using the measured source spectrum, divergence, and photon flux, the spectral brightness of the source can be estimated. Spectral brightness, in units of photons per second per unit source area per unit solid angle in a 0.1% relative bandwidth ($\Delta E/E$), is typically used to described synchrotron radiation. It is a good measure of the useful x-ray

flux for experiments requiring small beam divergence and a small spot size. An average spectral brightness of $\sim 10^{18}$ photons/sec/mm^2/mrad^2/(0.1% bandwidth) can be achieved using undulators at third-generation synchrotrons, such as the Advanced Light Source. From the measured characteristics above, $\sim 5 \times 10^4$ photons are generated in ~ 10 mrad cone in $\sim 15\%$ relative bandwidth from a spot ~ 30 μm (FWHM, laser spot size) by ~ 90 μm (FWHM, electron beam spot size) at a 5 Hz repetition rate. This leads to an average spectral brightness of $\sim 2 \times 10^3$ photons/sec/mm^2/mrad^2/(0.1% bandwidth) for the right-angle Thomson scattering x-ray source. The main sources of the large discrepancy in average spectral brightness between storage ring synchrotron sources and the Thomson scattering x-ray source are the repetition rate (~ 300 MHz versus 5 Hz, or a factor of $\sim 10^8$), the beam divergence ($1/\gamma \sim 1/3000$ versus 1/100, or a factor of $\sim 10^3$), the reduction in the number of electrons used per bunch due to the need for a short pulse duration (~ 300 fs/ 30 ps, or a factor of 10^2), and the electron beam emittance broadening effect on the relative bandwidth ($\sim 15\%$ relative bandwidth for the Thomson scattering source). The peak spectral brightness of the right-angle Thomson scattering x-ray source is ~ 400 photons/pulse/mm^2/mrad^2/(0.1% bandwidth). Because of this relatively poor spectral brightness, the right-angle Thomson scattering x-ray source is appropriate for only those experiments that can utilize a relatively large x-ray spot size and/or a relatively large spectral bandwidth.

Electron Beam Characterization Using Thomson Scattered X-Ray Properties

Not only is right angle Thomson scattering a promising source of ultrashort x-ray pulses, but it can also be used as a technique for probing structure in electron bunches

from accelerators [31, 32]. By analyzing the divergence and spectrum of the x-rays with the laser pulses interacting with various sections of the electron bunch, the small-scale emittance of the electron beam can be mapped out. The x-ray yield as the laser is scanned spatially across the beam diameter, and temporally along the electron bunch duration can be used to determine the electron bunch diameter and any small scale dynamic focusing of the beam. Such microprobing of electron bunches may be used to study electron beam dynamics within the bunch, rather than average behavior over the entire bunch.

Emittance measurement.

As seen in the previous section, the spectrum and the spatial profile of the x-rays generated by Thomson scattering depends on the emittance of the electron bunch, through the divergence of the electron beam at the focus. For a given beam emittance, a more tightly focused beam yields a more divergent beam. Thus, if the electron beam spot size is determined by some other means, the emittance of the beam can be obtained by determining the electron beam divergence by analyzing either the spatial profile or the energy spectrum of the Thomson scattered x-rays.

Because the laser only interacts with a small portion of the relatively long electron bunch, the emittance over the entire electron bunch can be mapped out. Measuring the emittance in this manner is also a more direct method than currently used methods. Also, performing an emittance measurement by analyzing the spatial profile of the Thomson scattered x-rays can be done in a single shot, only requiring a single electron bunch. Currently used emittance measurements, such as quadrupole scans, take the average emittance over the entire electron bunch, and need to take measurements over many

bunches [32].

Divergence measurements using the spatial profile of the x-ray pulse may not be very sensitive to the divergence of the electron bunches at the focus. If the electron beam divergence is on the order of the intrinsic x-ray beam divergence for perfectly collimated electrons, $\sim 1/\gamma$, the spatial broadening due to the large electron beam emittance is not readily apparent. As a result, this type of divergence measurement is best suited for higher energy electron beams, or to observe if an electron beam has extremely poor emittance. Analyzing the energy spectrum of the Thomson scattered x-rays is much more sensitive to the divergence of the electron beam, as a readily evident broadening of the spectrum is observed. This broadening is most evident at larger emission angles, but the x-ray flux is much lower in this region.

In either case, both of these measurement techniques actually measure the electron beam divergence. Since the electron beam emittance is determined by the divergence and spot size along each transverse axis, a sensitive means of measuring the electron beam spot size is necessary to determine the emittance. Imaging the spatial profile of OTR generated by the electron bunch going through a foil is one means of measuring the electron beam spot size. As shown below, analyzing the yield of Thomson scattered x-rays under different degrees of laser and electron beam overlap can also be used to determine the spatial size of the electron bunch.

Transverse and longitudinal profiles

Because the flux of Thomson scattered x-rays depends linearly on the number of electrons, monitoring the x-ray yield as a function of laser focus position in the electron

bunch determines the charge density profile of the bunch. As stated above, knowledge of
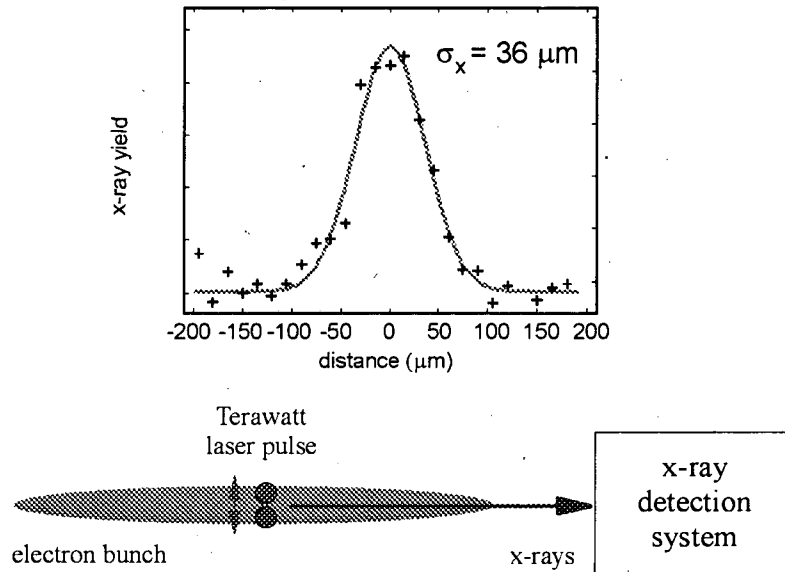
Figure 2.20: Transverse scan using the Thomson scattering electron beam diagnostic technique.

the electron beam spatial profile in conjunction with the Thomson scattering divergence measurements is necessary to determine the emittance of the beam. By scanning the laser focus across the transverse (perpendicular to the electron beam propagation direction) profile of the beam and monitoring the x-ray yield, the electron beam spot size may be determined, as shown schematically in Figure 2.20. OTR measurements of the electron beam spot size agree well with the Thomson scattering transverse scan. As a result, an emittance measurement technique based solely on Thomson scattering may be used.

Current electron beam diagnostics can only yield averages over larger beam slices (e.g. streak camera measurements of OTR), or average over the entire bunch. By measuring the x-ray yield as the laser beam is scanned across longitudinal (along the beam

propagation direction) profiles of the electron bunch, the electron bunch duration can be determined. If any nonuniformities in charge distribution exist, these can be located using the Thomson scattering x-ray probe.

OTR streak camera measurements of electron beams going through magnetic lattices with differing chromatic behavior do not appear to have any substantial structure [31]. However, as shown in Figure 2.21, longitudinal scans of the laser beam through the electron bunch for both of these lattices yield significantly different behavior. The large spike in the yield for the lattice with higher chromatic sensitivity may be explained by dynamic focusing caused by energy dependent focusing [31].
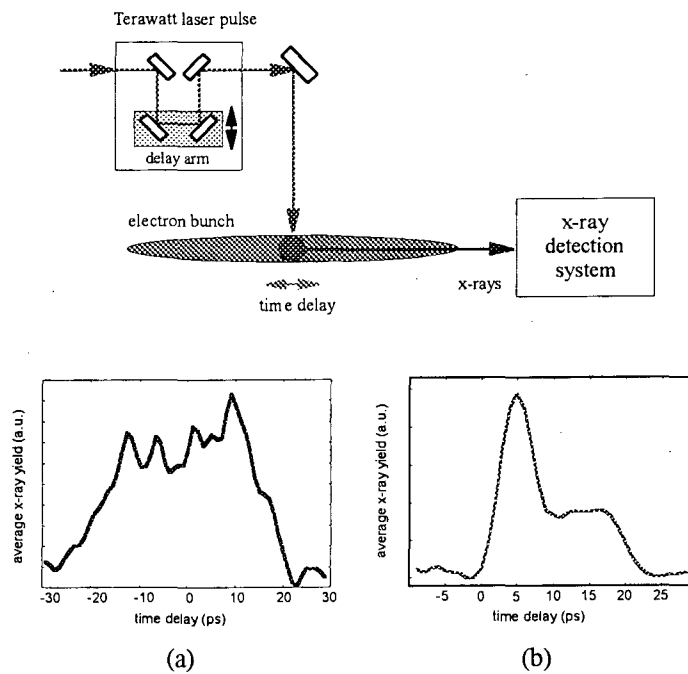
Figure 2.21: Longitudinal scans using the Thomson scattering diagnostic probing electrons transported through magnetic lattices with (a) low energy dispersion, and (b) high energy dispersion.

The ability to microprobe electron beam phase space using the Thomson scattering

diagnostic will lead to better understanding of electron beam dynamics in accelerators. As shown above, right-angle Thomson scattering off of electron bunches from the ALS linac propagated through a highly dispersive magnetic lattice permits the probing of electron beam energy structure. This small scale energy structure is not seen with time-averaging diagnostics. It is also not seen with OTR viewed on a visible streak camera (~ 2 ps resolution) [31]. Going to a magnetic lattice with low energy dispersion permits both longitudinal and transverse profiling of the electron bunch. This diagnostic is equivalent to imaging OTR and viewing OTR on a streak camera. Thus, the Thomson scattering diagnostic can be used for both conventional and non-conventional electron bunch characterization.

Chapter 3: Time-Resolved X-Ray Diffraction

X-ray diffraction is a very useful and well-established technique for studying long-range order in crystals. By performing time-resolved x-ray diffraction, structural dynamics in condensed matter may be observed. For example, the time-resolved x-ray diffraction technique has been used to study laser annealing of semiconductors on the nanosecond time scale [36, 37, 61]. By using intense femtosecond laser pulse excitation, ultrafast structural dynamics in semiconductors can be studied. Optical studies of Si [10, 11, 62, 63], GaAs [46, 64-69], graphite [70], and InSb [71] irradiated with femtosecond laser pulses suggest that disordering can occur on a subpicosecond time-scale. However, optical probes interact with valence electrons, which are extended states in condensed matter. As a result, optical probes are only indirectly sensitive to atomic positions. A more direct probe of long-range order in crystals is x-ray diffraction, because x-rays scatter off of core shell electrons. When the Bragg condition is satisfied, the scattered x-rays add coherently due to the periodic nature of the atomic positions in crystals. Determination of atomic position is achieved by spatial Fourier transform of the x-ray diffraction pattern. Because x-ray diffraction is a direct probe of long-range atomic order in crystals, ultrafast disordering in semiconductors may be studied using the Thomson scattering x-ray source by performing a time-resolved x-ray diffraction experiment. In this chapter, the theory of x-ray diffraction in strained crystals will be introduced, followed by a description of time-resolved x-ray diffraction experimental setup and results, and time-resolved x-ray diffraction studies on laser-perturbed semiconductors.

X-Ray Diffraction

X-ray diffraction has long been used to study atomic structure in condensed matter. The theory of x-ray diffraction is now quite established, and can predict diffraction efficiencies from perfect crystals quite accurately. The theory used to describe x-ray diffraction in perfect crystals, where interference between the incident and diffracted beams and multiple scattering of both beams are taken into account, is known as dynamical x-ray diffraction [15, 72]. Using only information about the particular atomic x-ray scattering [73], one can use the dynamical x-ray diffraction theory to accurately predict the x-ray reflectivity of a solid.

Theory

The most basic description of x-ray diffraction in crystals is that planes of atoms "reflect" incident x-rays. In analogy to optical reflection from multilayer dielectric structures, constructive interference of these "reflected x-rays" occurs when the path length difference for x-rays reflecting off of different planes is an integer multiple of the x-ray wavelength. As shown in Figure 3.1, this constructive interference occurs when

$$2d \sin \theta = n\lambda \qquad\qquad (3.1)$$

which is the Bragg condition for x-ray diffraction to occur, where d is the spacing between lattice planes. As the spacing between lattice planes are typically ~ 3 Å, x-rays with photon energies ~ 12 keV (wavelength ~ 1 Å) are suitable for x-ray diffraction.

Of course, x-rays incident upon a crystal do not interact with planes, but scatter off of individual atoms. Let us consider a small crystal (i.e. $< 10^4$ atomic layers) and assume x-ray absorption is negligible (or equivalently, a crystal made of weakly scattering atoms). In

this case, most of the incident x-rays pass through the crystal, and one only needs to consider how the small amount of x-rays scattered from the individual atoms interfere with each other at a given observation angle. The following explanation will closely follow the explanation of W. H. Zachariasen [15].
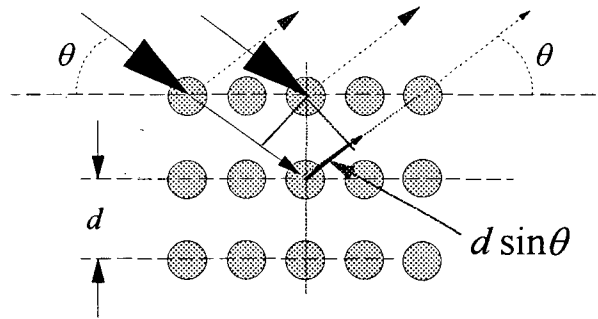
Figure 3.1: Bragg condition for x-ray diffraction.

To first order, x-ray scattering from an atom can be regarded as the sum of scattered x-rays from free electrons. Due to the greater mass ($\sim 10^3$ times greater), the nucleus contributes a negligible amount to the x-ray scattering compared to the electrons. The intensity of scattered x-rays from a single free electron is given by the familiar Thomson scattering formula,

$$I_{scattered} = I_0 \left(\frac{e^2 \sin \phi}{mc^2 R} \right)^2 = r_e^2 I_0 \left(\frac{\sin \phi}{R} \right)^2 \tag{3.2}$$

where I_0 is the incident x-ray intensity, $r_e = 2.82 \times 10^{-13}$ cm is the classical electron radius, ϕ is the angle between the electric field of the incident x-rays and the direction of scattering, and R is the distance to the point where the scattered x-rays are observed. The scattered x-rays are emitted in a dipole pattern, which is a fairly uniform distribution around the electron. Integrating over a sphere of radius R around the electron, the total flux of

scattered x-ray photons becomes

$$F_{scattered} = \frac{8\pi}{3} r_e^2 I_0 = \sigma_T I_0 \qquad (3.3)$$

where σ_T is the Thomson scattering cross-section.

A proper treatment of x-ray scattering from atoms takes into account the fact that the electrons in atoms are bound and occupy a finite volume [74, 75]. The fact that the electrons are in an attractive potential leads to absorption resonances and dispersion. The finite extent of the electrons causes relative phase shifts from different electrons in an atom, resulting in a change in the interference of the scattered fields from each electron. The net effect is that the x-ray scattering from electrons in atoms is modified relative to x-ray scattering from the equivalent number of free electrons. This modification is accounted for by the atomic scattering factor, f, which is defined as the amplitude of the x-ray electric field scattered by an atom relative to a free electron. In addition to being dependent upon atomic properties, the atomic scattering factor is dependent upon the scattering angle (angle between incident and scattered x-rays) and x-ray photon energy.

As crystals consist of repeated arrangements of atoms, one may consider the relative phases of the scattered x-rays from a section of a crystal that is repeated throughout the crystal, and then determine how the scattered x-rays interfere from the sum over all of the sections scattering x-rays. Each repeated section is known as a unit cell. The amplitude of scattered x-rays from a unit cell relative to a free electron is known as the structure factor, F. The structure factor, solely determined by the constituent atoms and their positions in the crystal (i.e. the crystal structure), is given by

$$F = \sum_j f_j \exp\left(i\vec{s} \cdot \vec{r}_j\right) \qquad (3.4)$$

51

where $\vec{r}_j$ is the position of the jth atom in the unit cell (referenced to one corner of the unit cell), f_j is the atomic scattering factor of the jth atom in the unit cell, and

$$\vec{s} = \vec{k} - \vec{k}_0 \qquad (3.5)$$

is the difference between the scattered ($\vec{k}$) and incident ($\vec{k}_0$) x-ray wavevectors, defined by

$$k = |\vec{k}| = k_0 = |\vec{k}_0| = \frac{2\pi}{\lambda}. \qquad (3.6)$$

Note that this definition of wavevector differs from the definition used by W. H. Zachariasen by a factor of 2π [15]. The photon recoil is very small for x-ray energies under consideration, and are neglected (i.e. the scattering is elastic). Using the same reference corner used for the atomic positions within a unit cell, the positions of one unit cell relative to another unit cell is given by a lattice vector, $\vec{A}_{hkl}$, defined by

$$\vec{A}_{hkl} = h\vec{a}_1 + k\vec{a}_2 + l\vec{a}_3 \qquad (3.7)$$

where h, k, and l range from 0 to the number of unit cells along each lattice vector direction, N_1, N_2, and N_3 respectively. For simplicity, assume the whole crystal is a parallelopiped with edges of length $N_1 a_1$, $N_2 a_2$, and $N_3 a_3$, making $N = N_1 N_2 N_3$ the total number of unit cells in the crystal. The scattered x-ray amplitude (relative to the scattered x-ray amplitude from a free electron) of an arbitrary unit cell relative to the unit cell at the origin is given by

$$\frac{\mathcal{E}_{hkl}}{\mathcal{E}_1} = F \exp\left(i\vec{s} \cdot \vec{A}_{hkl}\right) \qquad (3.8)$$

where $\mathcal{E}_1$ is the electric field amplitude of x-rays scattered by a single electron. The total scattered x-ray amplitude is then given by summing over all of the unit cells, with the

appropriate phases taken into account:

$$\frac{\mathcal{E}_{crystal}}{\mathcal{E}_1} = F \sum_{hkl} \exp\left(i\vec{s} \cdot \vec{A}_{hkl}\right). \tag{3.9}$$

It is here that we see the spatial Fourier transform nature of the x-ray diffraction technique in determining atomic order in crystals. Using the fact that each summation is a geometric series,

$$\sum_{x=0}^{n} \exp\left(ix\alpha\right) = \frac{\exp\left(in\alpha\right) - 1}{\exp\left(i\alpha\right) - 1} \tag{3.10}$$

Equation 3.9 becomes

$$\frac{\mathcal{E}_{crystal}}{\mathcal{E}_1} = F \prod_{n=1}^{3} \frac{\exp\left(iN_n \vec{s} \cdot \vec{a}_n\right) - 1}{\exp\left(i\vec{s} \cdot \vec{a}_n\right) - 1}. \tag{3.11}$$

Multiplying the amplitude ratio by its complex conjugate, one obtains the intensity ratio

$$\frac{I_{crystal}}{I_1} = |F|^2 \prod_{n=1}^{3} \left[\frac{\sin\left(\frac{1}{2} N_n \vec{s} \cdot \vec{a}_n\right)}{\sin\left(\frac{1}{2} \vec{s} \cdot \vec{a}_n\right)}\right]^2. \tag{3.12}$$

Maxima occur when the momentum change of the scattered x-rays relative to the incident x-rays equals a reciprocal lattice vector:

$$\vec{s} = \vec{B}_{hkl} = 2\pi \left[\left(\frac{h\vec{a}_1}{|\vec{a}_1|^2}\right) + \left(\frac{k\vec{a}_2}{|\vec{a}_2|^2}\right) + \left(\frac{h\vec{a}_3}{|\vec{a}_3|^2}\right)\right] = 2\pi\left(h\vec{b}_1 + k\vec{b}_2 + l\vec{b}_3\right), \tag{3.13}$$

i.e. when the Laue equations are satisfied. Note the factor of 2π difference between this definition of the reciprocal lattice vector and that of W. H. Zachariasen [15]. Under conditions of strong x-ray diffraction, the resulting x-ray scattered intensity from the crystal relative to a single electron becomes

$$\frac{I_{crystal}}{I_1} = |F_{hkl}|^2 N^2. \tag{3.14}$$

53

where

$$F_{hkl} = \sum_j f_j \exp\left(\vec{B}_{hkl} \cdot \vec{r}_j\right).$$ (3.15)

is the structure factor under conditions of strong x-ray diffraction.

As most x-ray sources have a beam divergence that is greater than the angular acceptance for strong x-ray diffraction, a useful measure of the diffraction efficiency of a crystal is the integrated intensity. The integrated intensity is the total diffracted power integrated over the entire solid angle that the diffracted beam subtends. Taking into account the appropriate geometrical factors, the integrated intensity for a small crystal becomes

$$\frac{P_{crystal}}{P_0} = \frac{r_e^2}{A_0} \frac{\lambda^3 V_{crystal} |F_{hkl}|^2}{V_{cell}^2} \left(\frac{1 + \cos^2 2\theta}{2 \sin 2\theta}\right)$$ (3.16)

where A_0 is the area of the incident x-ray beam, V_{cell} is the unit cell volume, and the total crystal volume $V_{crystal} = N\, V_{cell}$. The $1 + \cos^2 2\theta$ term is due to averaging over x-ray polarizations, assuming the incident x-ray beam is unpolarized, and becomes 1 if the x-ray polarization is perpendicular to the plane of diffraction. For a mosaic crystal, i.e. a crystal consisting of randomly oriented blocks of small crystals, x-ray diffraction from each block is described by Equation 3.16. Averaging over the distribution of orientations leads to an increase in the rocking curve width of a mosaic crystal. The number of small crystals that the x-rays interact with is limited by the photoelectric absorption depth, $1/\mu$, where μ is the photoelectric absorption coefficient. The resulting averaging leads to the following integrated intensity for mosaic crystals:

$$\frac{P_{mosaic}}{P_0} = r_e^2 \frac{\lambda^3 |F_{hkl}|^2}{2\mu V_{cell}^2} \left(\frac{1 + \cos^2 2\theta}{2\sin 2\theta} \right). \qquad (3.17)$$

The main difference between Equation 3.17 and 3.16 is that the number of diffracting unit cells is determined by the photoelectric absorption depth, rather than the crystal thickness.

When x-ray scattering from each atom is strong, or the number of atoms coherently adding to the diffracted x-ray beam is large (ideal crystal), i.e. when the scattering of the diffracted wave must also be taken into account, the small crystal picture above does not apply. Theories that self-consistently take into account multiple scattering are known as dynamical x-ray diffraction theories. In dynamical x-ray diffraction, electromagnetic fields propagating in a medium with a periodic dielectric function (due to the atoms in an ideal crystal) are considered. The dielectric constant of the crystal can be expressed as

$$\varepsilon = \varepsilon_0 \left(1 + \psi \right) \qquad (3.18)$$

where ε_0 is the dielectric constant of vacuum, and

$$\psi = \sum_{hkl} \psi_{hkl} \exp\left(-i\vec{B}_{hkl} \cdot \vec{r} \right) \qquad (3.19)$$

where

$$\psi_0 = -\frac{\lambda^2 r_e}{\pi V_{cell}} F_0, \; \psi_{hkl} = -\frac{\lambda^2 r_e}{\pi V_{cell}} F_{hkl} \qquad (3.20)$$

with F_{hkl} given by Equation 3.15, and with the average structure factor given by

$$F_0 = F_{000} = \sum_j f_j \exp\left(\vec{B}_{000} \cdot \vec{r} \right) = \sum_j f_j. \qquad (3.21)$$

The distance along incident and diffracted beam paths is given by

$$x_0 = -\frac{\lambda A_0}{\pi \psi_0'}, \quad x_{hkl} = -\frac{\lambda A_{hkl}}{\pi \psi_{hkl}'} \tag{3.22}$$

where the average and periodic part of the dielectric constant due to the crystal is given by

$$\psi_0 = \psi_0' + i\psi_0'', \quad \psi_{hkl} = \psi_{hkl}' + i\psi_{hkl}'' = \psi_{hkl}'(1 + ik). \tag{3.23}$$

With $\vec{n}$ defined as a unit vector perpendicular to the incident crystal surface, the direction cosines for the incident and diffracted beams is given by

$$\gamma_0 = \vec{n} \cdot \vec{S}_0, \quad \gamma_{hkl} = \vec{n} \cdot \vec{S}_{hkl}, \tag{3.24}$$

and the ratio of the direction cosines is

$$b = \frac{\gamma_0}{\gamma_{hkl}}. \tag{3.25}$$

Note that b is negative for x-ray diffraction in the Bragg geometry (reflection), and b is positive for x-ray diffraction in the Laue geometry (transmission). For symmetric x-ray diffraction (incident angle = diffracted angle, relative to the surface), $b = \pm 1$ for the Laue/Bragg geometries, respectively. The reduced depth into the crystal becomes

$$A = -\frac{\gamma_{hkl} A_{hkl} + \gamma_0 A_0}{\sqrt{|\gamma_0 \gamma_{hkl}|}}. \tag{3.26}$$

The reduced absorption factor (accounting for photoelectric absorption in the crystal) is given by

$$g = -\frac{1}{2}\frac{(1-b)\psi_0''}{\psi_{hkl}'\sqrt{|b|}}, \tag{3.27}$$

and the reduced deviation from the Bragg condition for strong x-ray diffraction from the crystal (the Bragg condition is met for $-1 \le y \le 1$), is given by

$$y = -\frac{1}{2}\frac{(1-b)\psi_0' + b\alpha_{hkl}}{\psi_{hkl}'\sqrt{|b|}}, \qquad (3.28)$$

where

$$\alpha_{hkl} = 2\sin 2\theta_B(\theta_B - \theta). \qquad (3.29)$$

Finally, the scattering efficiency per reduced unit distance is given by

$$X(A) = \frac{D_{hkl}(A)\sqrt{|\gamma_{hkl}|}}{D_0(A)\sqrt{|\gamma_0|}}, \qquad (3.30)$$

where D_0 and D_{hkl} are the electric field of the incident and diffracted waves, respectively. There are two points to note from these equations. One is that the reduced depth A represents the depth into which strongly diffracted x-rays penetrate the crystal (attenuation depth). The other is that we can see from Equations 3.28 and 3.29 that the incident x-rays experience refraction (albeit small) in the crystal, resulting in a slight shift of the Bragg angle than that expected from Equation 3.1.

Strong x-ray diffraction (attenuated propagation into the crystal) occurs for certain propagation directions (when the Laue conditions are satisfied), analogous to bandgaps for electronic wavefunctions in crystals. Details of the theory can be found in *Theory of X-Ray Diffraction in Crystals*, by W. H. Zachariasen [15]. The results are that when strong x-ray diffraction occurs, the x-ray reflectivity (in the Bragg geometry) per unit reduced depth of an ideal crystal can be determined by the following differential equation (expressed in reduced units):

$$i\frac{dX}{dA} = X^2(1+ik) - 2X(y+ig) + (1+ik), \qquad (3.31)$$

and the resulting x-ray reflectivity of the ideal crystal is determined by (after integrating

Equation 3.31)

$$R(\theta) = |X(0)|^2 \qquad (3.32)$$

where $X(0) = X(\theta, A = 0)$.

X-ray diffraction from crystals with strained layers

For laser perturbed samples, heating and disordering is not necessarily uniform across the x-ray attenuation depth. A theory that takes into account a spatially varying strain profile has been developed [76], and used quite successfully in analyzing nanosecond annealing of semiconductors [61]. To account for the effects of thermal randomization of atomic positions, the Debye-Waller factor e^{-M} is included, with M given by

$$M = \left(\frac{6h^2 T}{mk_B \theta_D^2} \right) \Phi \left(\frac{\theta_D}{T} \right) \left(\frac{\sin(\theta_B)}{\lambda} \right)^2 \qquad (3.33)$$

where $\Phi(x)$ is the Debye function, and the temperature $T = T(A)$, is a function of the depth into the crystal. Because thermal strain causes the crystal planes to shift in spacing, the Bragg angle needs to be modified to account for different amounts of strain as a function of depth. Taking the derivative of the Bragg condition (Equation 3.1, with $n = 1$)

$$2\Delta d = -\frac{\lambda}{\sin^2(\theta_B)} \cos(\theta_B) \Delta \theta_B = -\frac{2d}{\tan(\theta_B)} \Delta \theta_B \qquad (3.34)$$

and utilizing the strain relationship, one obtains

$$\varepsilon = \frac{\Delta d}{d} = -\frac{1}{\tan(\theta_B)} \Delta \theta_B \qquad (3.35)$$

which may be a function of depth, e.g. through a thermal gradient. The strain as a function

of depth may be determined by [61]

$$\varepsilon(T) = \int_{T_0}^{T} \alpha(T')\eta_{hkl}dT' \tag{3.36}$$

where the temperature T is a function of depth into the crystal, $\alpha(T)$ is the thermal expansion coefficient, and η_{hkl} is a factor accounting for the one dimensional nature of the strain, and the elastic anisotropy of the crystal [61]. For elastically anistotropic crystals with surfaces parallel to the (111) or (100) planes, η_{hkl} is given by

$$\eta_{111} = \frac{3(1 + 2C_{12}/C_{11})}{1 + 2C_{12}/C_{11} + 4C_{44}/C_{11}} \tag{3.37}$$
$$\eta_{100} = 1 + 2C_{12}/C_{11}$$

where C_{11}, C_{12}, and C_{44} are elastic constants. Using Equations 3.35 and 3.36, the Bragg angle as a function of depth becomes

$$\theta_B(A) = \theta_B^0 - \varepsilon(A)\tan(\theta_B) \tag{3.38}$$

where θ_B^0 is the non-perturbed Bragg angle, and $\varepsilon(A) = \varepsilon(T)$ is an implicit function of depth. Equation 3.38 determines the Bragg angle in Equation 3.29 for a crystal with a strained layer. Note that the strained crystal theory only applies if the strain and the variation of the strain between atoms is small [76].

Equation 3.31 may be solved numerically (e.g. using the Runge-Kutta integration method) to solve for the x-ray scattering amplitude at the surface, $X(0)$, using the boundary condition $X(A_{max}) = 0$. This boundary condition simply states that there is no scattering beyond the bottom of the crystal. Once the scattering amplitude at the surface is obtained, the x-ray reflectivity as a function of incident angle of the x-rays is determined by Equation 3.32. The reflectivity curve as a function of angle may be fitted to experimental data to yield a temperature distribution, or a theoretically based temperature

59

distribution may be used to determine a reflectivity curve that may be compared with experiment to test models of laser perturbed crystals. This was done in the case of nanosecond laser annealing of silicon [36, 61].

X-Ray Diffraction Using the Thomson Scattering X-Ray Source

Due to the relatively low flux per pulse in a fairly broad bandwidth, the number of diffracted photons per pulse is less than one. This allows for the use of the Ge detector in photon counting mode with pulse-height analysis to obtain spectral information on the diffracted x-rays. Such spectra obtained while tuning the angle of incidence on an unperturbed crystal of Si shows a shift in the energy of the diffracted spectrum with angle. This spectral shift can be used to obtain information about the strain in the sample under laser perturbation.

X-ray diffraction measurements performed on unperturbed crystals using the Thomson scattering x-ray source demonstrate that time-resolved experiments are possible. Figure 3.2 shows a schematic of x-ray diffraction using x-rays from the Thomson scattering x-ray source, with their divergent, polychromatic properties. Also shown are x-ray diffraction spectra at different sample angles, and the resulting shift in spectral peak position with crystal angle. The spectral peak shift follows the Bragg law, modified by geometrical factors to account for the stationary nature of the detector (see Appendix B). The bandwidth of the diffracted spectrum is mainly determined by the acceptance aperture of the detector ($\sim$ 1 mrad), due to the relatively large divergence of the x-ray beam compared to the acceptance divergence of the silicon crystal ($\sim$ 10 μrad), and the broad bandwidth of the x-rays. This broad bandwidth allows for matching of the Bragg condition

at different x-ray energies in the bandwidth over the divergence of the x-ray beam.

$$\frac{\Delta E}{E} = \frac{\Delta \lambda}{\lambda} = \frac{\Delta \theta}{\tan \theta_B}$$
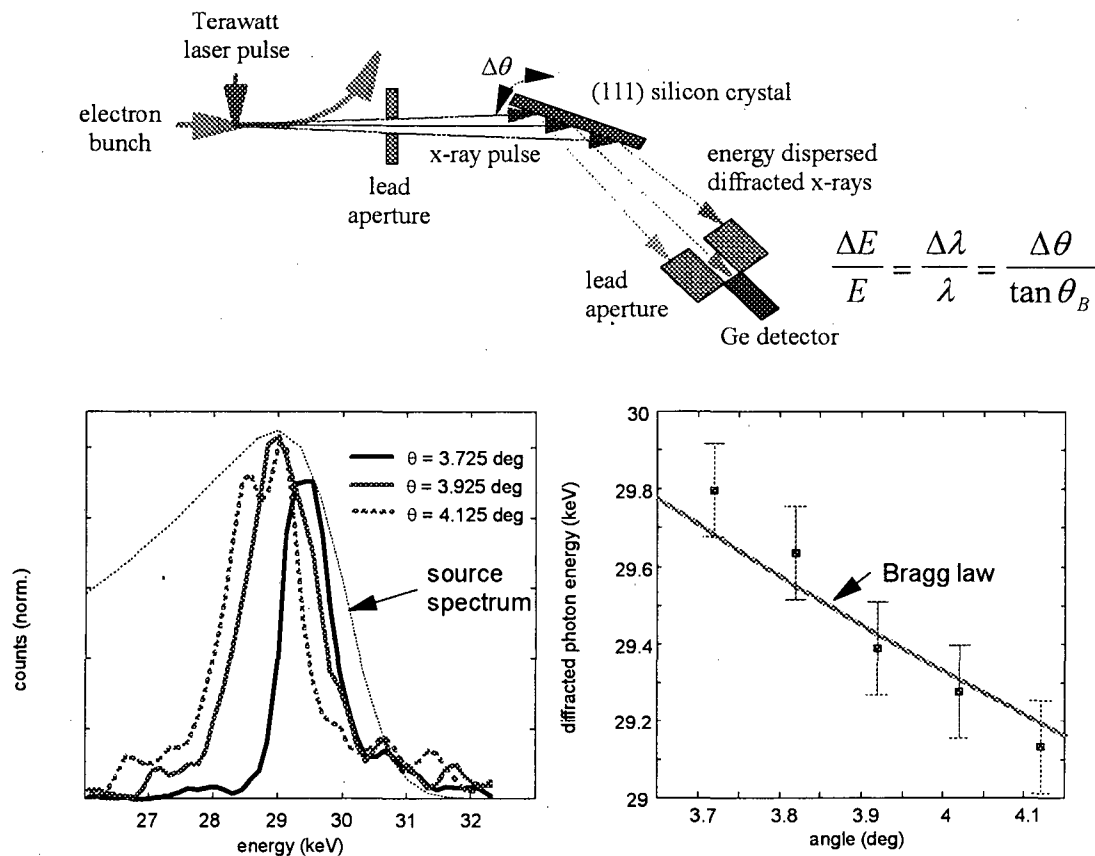
Figure 3.2: X-ray diffraction from Si (111) using the Thomson scattering x-ray source.

Time-Resolved X-Ray Diffraction Studies of Laser-Perturbed InSb

Time-resolved x-ray diffraction is a useful tool for the study of structural dynamics in condensed matter, allowing long-range order dynamics in crystals to be observed. For example, nonequilibrium electron-phonon dynamics may be studied by probing the resulting lattice expansion after intense laser excitation. Due to the high density electron-hole plasma formed, semiconductor dynamics under high-intensity laser excitation are difficult to study using optical techniques. In order to study the ultrafast structural

dynamics in InSb under high-intensity laser excitation, we performed femtosecond time-resolved x-ray diffraction using the right-angle Thomson scattering x-ray source.

Asymmetric x-ray diffraction

One of the factors that determines the observed modification of x-ray diffraction properties due to laser perturbation is the penetration depth of the laser and x-ray beams into the sample. If the x-ray penetration depth is much larger than the laser penetration depth, then only a fractional change in the diffraction signal is expected, even if the laser melts the crystal. Another factor to consider is the x-ray attenuation depth versus the x-ray absorption depth in the crystal. The x-ray attenuation depth is the depth penetrated into the crystal by x-rays that meet the Bragg condition. X-rays that undergo diffraction only penetrate a finite amount of the sample because diffraction takes energy away from the incident beam when the Bragg condition is satisfied. The attenuation depth is different than the absorption depth due to photoelectric absorption. If this attenuation depth is smaller than the absorption depth, then diffraction from both laser perturbed and unperturbed layers may be seen, even if a melted layer with a depth comparable to the attenuation depth is formed. One means of assuring that only the laser perturbed sample is probed by the x-rays is to choose an x-ray wavelength that provides an absorption depth that matches the laser penetration depth. Another means is to utilize crystals with atomic planes at an angle relative to the surface, so that x-ray diffraction occurs in the asymmetric geometry. This x-ray diffraction geometry allows for a smaller penetration depth due to the larger component of path length traversed parallel to the surface, as shown schematically in Figure 3.3.

$$\frac{1}{\alpha_{eff}} = \frac{\sqrt{\sin(\theta - \alpha)\sin(\theta + \alpha)}}{\pi\left(\frac{e^2}{mc^2}\right)|F_{hkl}|N\lambda}$$

absorption depth $\sim \sin(\theta - \alpha)$
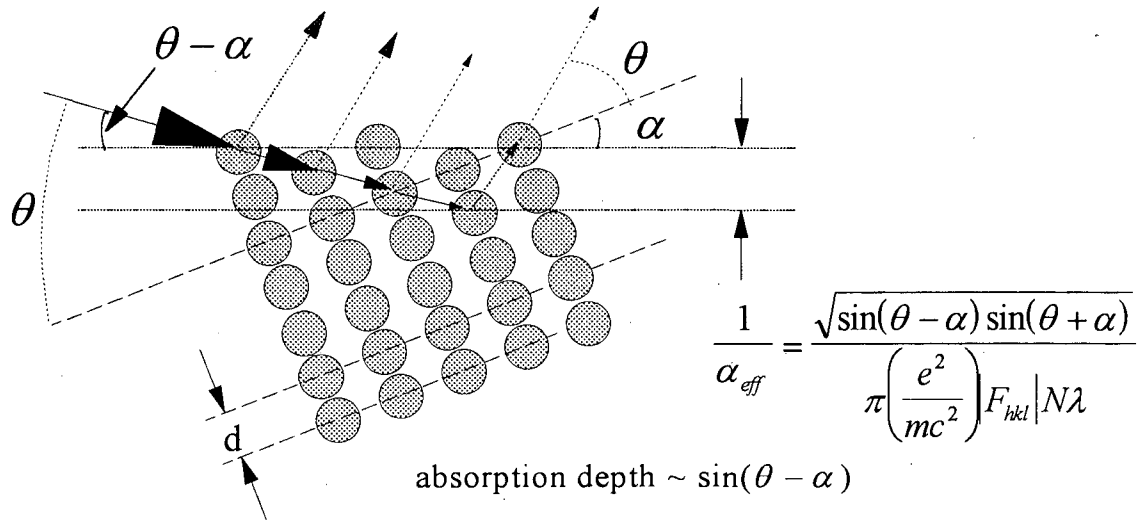
Figure 3.3: Asymmetric Bragg diffraction.

Experimental setup

Time-resolved x-ray diffraction studies of InSb were performed by using the x-ray

pulses along with synchronized femtosecond laser pulses involved in the x-ray generation.

The experimental setup is schematically shown in Figure 3.4. The InSb crystal used was

cut 3° off the (111) orientation to allow x-ray diffraction in the asymmetric Bragg

geometry (the x-ray beam is incident ~ 0.4° relative to the crystal surface). This geometry

provides a better match between the penetration depths of the x-rays (~ 500 nm) and laser

(~ 100 nm), measured perpendicular to the surface (note that the optical absorption depth

remains ~ 100 nm even for angles of incidence close to 90° from normal incidence, due to

the large refractive index of InSb.) The asymmetric Bragg diffraction geometry also

increases the x-ray diffraction acceptance bandwidth for x-rays incident at shallow angles

[15, 72].

A fraction (10%) of the laser beam used to generate the x-rays is split off and used

for sample excitation. As it is part of the laser used for x-ray generation, the sample

excitation laser beam is absolutely synchronized to the ultrashort x-ray pulses generated by
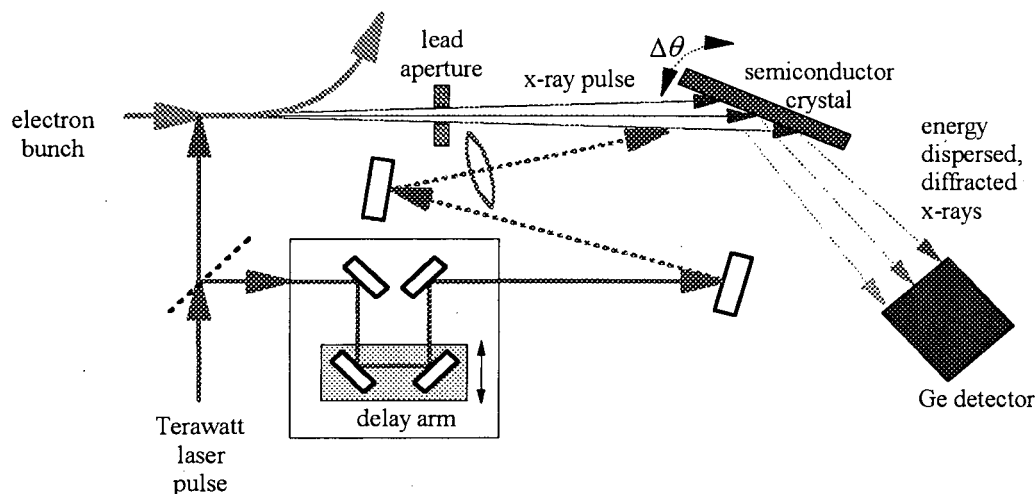
Figure 3.4: Time-resolved x-ray diffraction experimental setup.

the rest of the laser beam. The angle between the sample excitation laser beam and the x-

rays (~ 4°) is kept small in order to reduce the temporal walkoff (~ 500 fs) between the

beams. The temporal zero between the x-ray and laser pulses is obtained by sending

unamplified laser pulses through the system, and imaging the x-ray generation point

(interaction point) onto the sample (see Figure 3.5). This imaging is performed by using a

HeNe laser (the one used for electron beam alignment) to illuminate the alignment cube

(see Chapter 2, experimental setup section) placed at the interaction point, and imaging

the scattered light from the hole in the cube (200 μm diameter) with a lens onto a CCD

camera (Cohu, 33.3 μm by 27.0 μm pixel size). The alignment cube is removed, a

beamsplitter is placed at the electron-laser interaction point to allow part of the laser beam

to follow the x-ray beam path, and cross-correlation techniques are used with the two

beams. The uncertainty in the position of the beamsplitter is mainly determined by the size

of the hole in the alignment cube (since the smaller electron beam can be anywhere within the hole), as the beamsplitter can be reproducibly positioned to within 25 μm. Thus, the uncertainty in the beamsplitter position (± 100 μm) leads to a 300 fs temporal uncertainty.
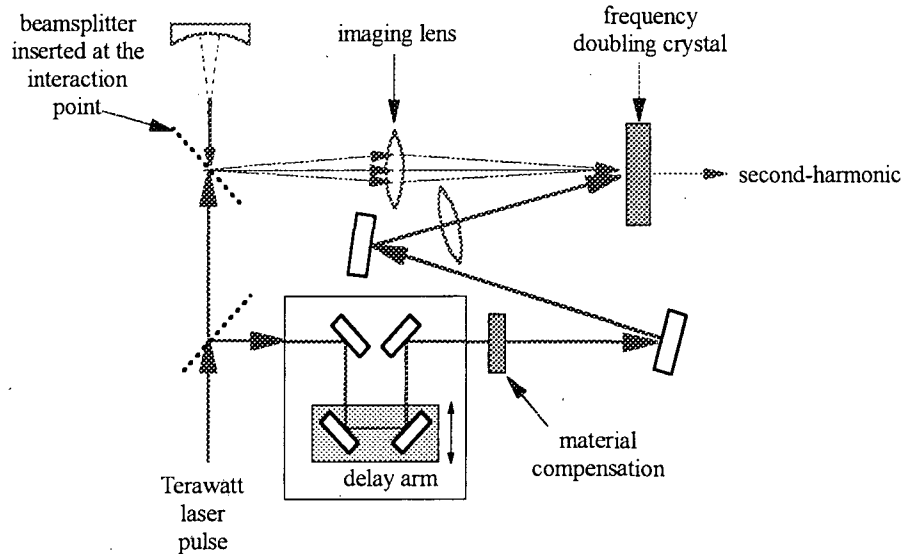
Figure 3.5: Determining the temporal zero.

Material dispersion compensation of the Lexan vacuum window and beamsplitter is achieved by placing the equivalent amounts of material in the delay arm path. The material dispersion in the imaging lens (Newport KPX 106, 200 mm focal length, BK7 glass, 3.78 mm ± 0.1 mm specified thickness) is accounted for by measuring the thickness of the imaging lens (t = 3.86 mm ± 0.01 mm) and calculating the appropriate delay introduced by the lens at the laser wavelength (index of refraction of BK7, n = 1.51 at 800 nm). The resulting delay introduced by the imaging lens is determined by the transit time through the glass relative to the transit time through air, given by $\tau_d = (n - 1) \, t/c$, where c is the speed of light in vacuum. The time delay introduced by the lens is τ_d = 6.57 ± 0.02 ps. Therefore, the estimated uncertainty in the zero position is ~ 300 fs, and is mainly determined by the

uncertainty position of the beamsplitter. The p-polarized (electric field perpendicular to the page in Figure 3.4) laser beam is focused by a 75 cm focal length lens to a 3 mm diameter spot at the sample, with the sample positioned before the laser focus. The laser beam illuminates an elliptical spot on the sample at a fluence of 20 mJ/cm^2, which is consistent with the laser fluence needed to see signs of disorder in optical experiments [71]. The laser spot on the sample is slightly larger than the x-ray spot to provide more uniform excitation of the area probed by the x-rays. The sample is moved after multiple ($\sim 10^4$) laser shots. While slight surface damage (monitored while collecting data by observing the scattered laser light from the sample) occurs after multiple shots, no significant degradation in the x-ray diffraction signal is observed. The damaged regions were smaller than the laser and x-ray spots on the sample. Inspection of the slightly damaged areas (visible as a white streak) under an optical microscope revealed flat regions mixed in with smaller raised spots, which may indicate recrystallized areas mixed with amorphous regions. Only the reversible changes in the sample are probed in our experiment.

The x-ray beam is apertured to ~ 200 μrad in the diffraction plane to allow for better spectral resolution and to allow the beam to cover a reasonable area on the InSb crystal. The aperturing reduces the number of diffracted x-ray photons to about 1 every 10 x-ray pulses. This allows for pulse-height analysis of the voltage signal from the diffracted x-ray photons detected by a LN$_2$ cooled Ge detector (~ 300 eV resolution at 30 keV) to obtain the diffracted photon energy spectrum. The unused portion of the x-ray beam is used to monitor the x-ray flux, via the phosphor detection system [31, 33]. A hole is placed in the phosphor to allow the central portion of the x-ray beam to reach the sample.

For each time delay, 100 x-ray shots are accumulated. Further accumulation of data is accomplished by repeating the sequence of time delays, thereby minimizing any systematic effects.

Experimental results

Representative x-ray diffraction spectra (averaged over $\sim 10^4$ x-ray shots) for –20 ps and +100 ps time delays (positive time delays indicate that x-ray pulses arrive after laser pulses on the sample) are shown in Figure 3.7. The peak of the x-ray diffraction spectrum at +100 ps is slightly shifted towards lower energy relative to the x-ray diffraction spectrum at –20 ps. This provides evidence that thermally expanded layers are formed near the surface on this time scale. The x-ray diffraction spectrum at +100 ps is also broader than the spectrum at –20 ps. This may be explained by the fact that x-rays

(a)   (b)
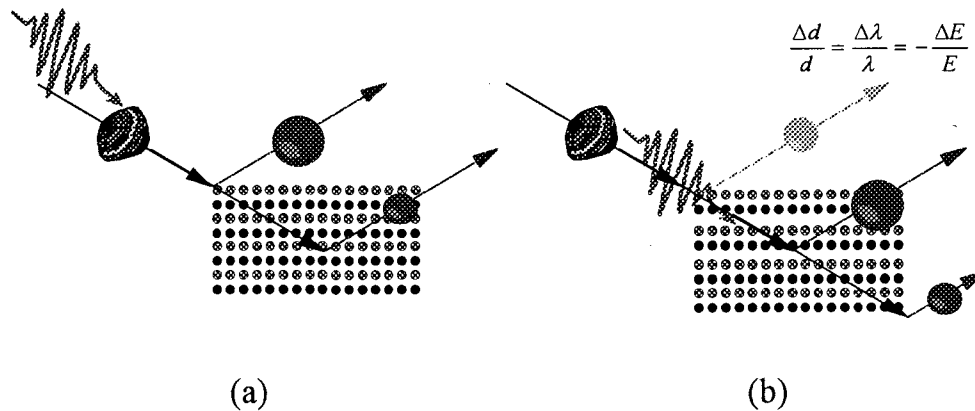
Figure 3.6: X-ray diffraction from (a) an unperturbed crystal, and (b) a crystal with thermally expanded layers.

diffracting off both an expanded layer and an unperturbed layer result in an increase in the bandwidth of the diffracted x-rays. As schematically shown in Figure 3.6, with our

collimated, polychromatic Thomson scattering x-ray source, the result is an increase in the integrated x-ray diffraction signal.

Laser-induced lattice expansion has also been observed in time-resolved x-ray diffraction experiments studying nanosecond laser annealing in Si [61], and more recently in femtosecond laser perturbed GaAs [34]. Our results are consistent with the ultrafast lattice expansion observed in the laser perturbed GaAs, where an increase in the x-ray diffraction angular acceptance is observed using a divergent, monochromatic laser-produced plasma x-ray source [34]. Using the thermal expansion coefficient of InSb $(5 \times 10^{-6}/K)$ and assuming the lattice is heated up to the melting temperature (803 K), the maximum spectral shift in diffracted x-rays due to increased lattice spacing is ~ 80 eV, which is on the order of the observed ~ 40 eV shift in the Gaussian fits to the spectra in Figure 3.7.
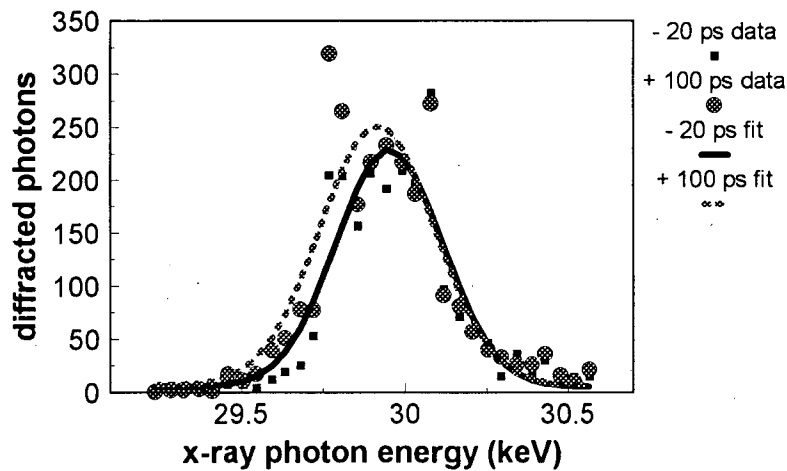
Figure 3.7: X-ray diffraction spectra from laser perturbed InSb at time delays of −20 ps and +100 ps.

The x-ray diffraction spectra integrated over the Bragg peak as a function of time

delay is shown in Figure 3.8. We call attention to two features of the data. First, there is a

rise in the integrated counts for long time delays. The rise is evidence of an increase in the

diffraction bandwidth caused by the growth of a thermally expanded layer near the surface.

Second, a delay (~ 10 ps) in the onset of the rise is observed, which may be attributed to

energy relaxation from the electron-hole plasma to acoustic phonons. Figure 3.9 shows the

corresponding spectral peak position and width (using Gaussian fits to the spectra) as a

function of time delay. The increasing shift in the spectral peak position and spectral width

of the x-ray diffracted photons as a function of time delay strongly suggests that the rise is

due to an expanded layer that is increasing in thickness.
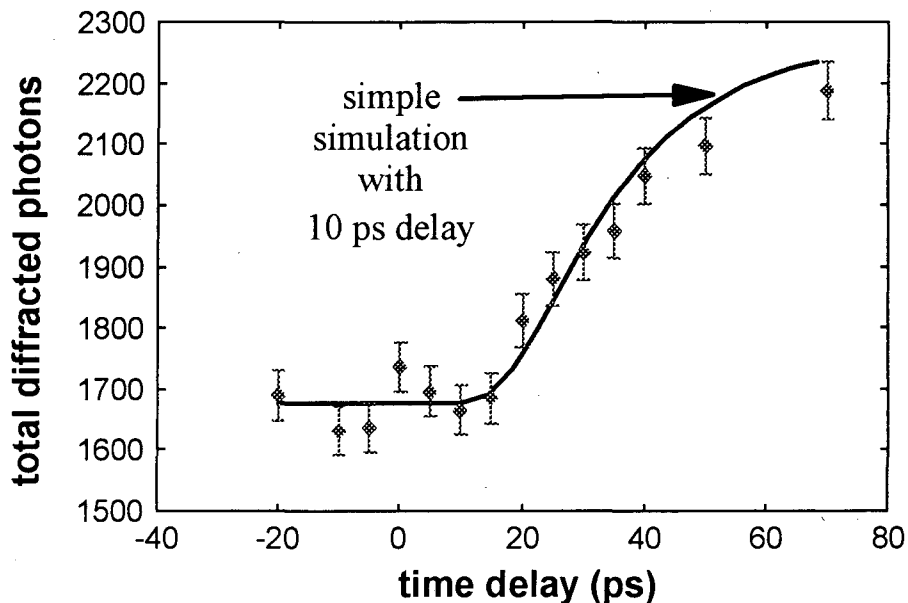
Figure 3.8: Total diffracted x-ray photons versus time delay from laser perturbed InSb. The curve is a fit to the data assuming an exponential strain profile growing in thickness at the speed of sound, and a 10 ps delay in the onset of growth.

X-ray diffraction from a crystal with a strain profile can be calculated following the

method used by B. C. Larson, et al. [61]. Using this method, a modeling of the rise in x-

ray diffraction signal is performed, including the x-ray source parameters and assuming an expanded layer at the surface. The expanded layer is assumed to be governed by the thermal expansion coefficient and an exponentially decreasing temperature profile (maximum temperature is assumed to be the melting temperature, 803K). The $1/e$ depth of the temperature profile is assumed to increase at the speed of sound (5×10^5 cm/s), simulating nonequilibrium acoustic phonon transport. As shown in the curve in Figure 3.7, with a 10 ps delay in the onset of expansion, the simple model fits the data well. The model also qualitatively fits the spectral peak and spectral width as a function of time
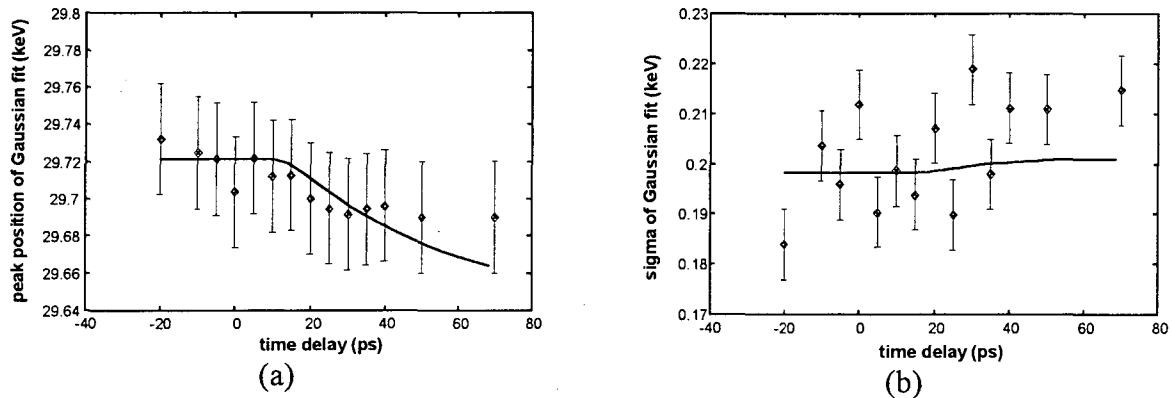
Figure 3.9: Parameters of Gaussian fits to x-ray diffraction spectra versus time delay: (a) spectral peak position, and (b) spectral width. The curve is from the same fit in Figure 3.7.

delay (see Figure 3.9). The error bars to the Gaussian fit parameters are estimated by using the shot noise limited errorbars for each point in the spectrum to be fitted. The simulation used assumed an x-ray photon energy peak ~ 230 eV above the experimental peak, so the curve in Figure 3.9 (a) is shifted by 230 eV. In Figure 3.9 (b), the spectral width of the simulation was convolved with a 195 eV sigma Gaussian, to account for detector broadening of the spectrum. Note that the data cannot be matched if the

thermally expanded layer is assumed to grow via a diffusion process (using the thermal diffusion coefficient).

Simulation of laser-heated semiconductors

While the simple model described above agrees with the data, it does not take into account all of the physical processes that are occurring. In order to better understand the nonequilibrium laser heating process, a more complex simulation (a modified version of the model of Lietoila and Gibbons [77]) was implemented. The simulation accounts for Auger recombination, longitudinal-optic (LO) phonon emission, acoustic phonon generation (accounted for as lattice heating), phonon propagation, and lattice expansion (governed by a temperature profile and the thermal expansion coefficient). Measured values of various parameters for InSb were used: Auger recombination coefficients, the ambipolar diffusion constant, the speed of sound, etc. The less well known (especially under high-excitation conditions) energy relaxation times were assigned reasonable values to try to better fit the data.
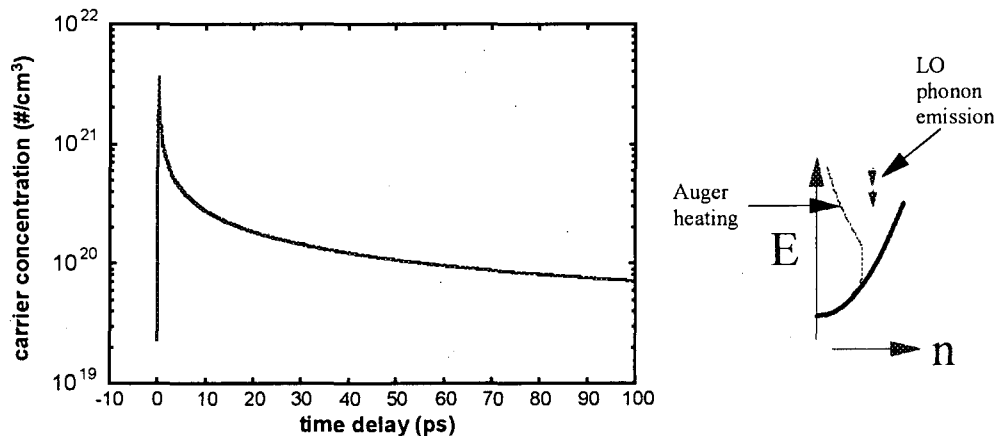
Figure 3.10: Delayed transfer of energy to the lattice due to Auger recombination and carrier heating, and subsequent LO phonon emission.

The laser heating process is assumed to proceed in the following manner. The absorbed laser pulse energy is absorbed in the semiconductor by creating electron-hole pairs. This results in the creation of a dense electron-hole plasma ($\sim 4\times10^{21}$ carriers/cm^3). The dense electron-hole plasma may remain dense for a relatively long time (~ 1 ps) due to ambipolar diffusion and bandgap renormalization, which tend to offset hot carrier transport [78]. Consequently, Auger recombination becomes the dominant recombination mechanism for the carriers, resulting in a lowering of carrier density while maintaining the energy in the carriers (see Figure 3.10). This energy is eventually transferred to the lattice through the emission of longitudinal-optic (LO) phonons [79]. The time scale for this energy relaxation has been recently observed to be ~ 10 ps in GaAs near the ultrafast melting threshold [64]. Delayed heating due to Auger recombination was also observed in Si at lower carrier density [80]. Because LO phonons involve relative motion between basis atoms in the zinc-blende structure, these phonons do not induce thermal expansion of the lattice. As acoustic phonons involve motion of one set of basis atoms relative to another, the relaxation of LO phonons into acoustic phonons and the propagation of these acoustic phonons is the likely cause of the lattice expansion. Since the surface is free to move, and most of the energy is deposited closest to the surface, significant lattice expansion is likely to occur at the surface first (see Figure 3.11). Expansion is expected to only occur in a direction perpendicular to the surface, as the lateral dimensions are confined. This confinement of expansion in the lateral dimension was observed in nanosecond time-resolved x-ray diffraction measurements on Si [81]. As more LO phonons relax into acoustic phonons, which then propagate into the sample at the speed of sound, lattice expansion moves deeper into the sample.

72
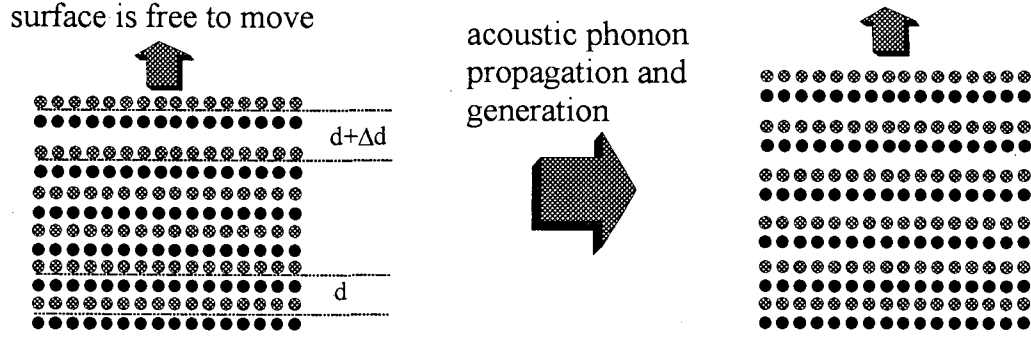
Figure 3.11: Nucleation of thermal expansion at the surface.

The processes described above are modeled using the following equations. One dimensional (along x, perpendicular to the surface) diffusion is assumed, as the area excited by the laser is orders of magnitude greater than the depth. Carrier generation, diffusion, and recombination are accounted for by

$$\frac{dN}{dt} - \frac{d}{dx}\left(D_a \frac{dN}{dx}\right) = S - (C_e + C_h)N^2(N - N_0) \tag{3.38}$$

where N is the carrier concentration (electrons and holes), N_0 is the intrinsic carrier concentration, D_a is the ambipolar diffusion coefficient, C_e and C_h are the electron-electron-hole and hole-hole-electron Auger recombination coefficients, and S is the source term (concentration of carriers generated per unit time) due to the laser

$$S = \frac{F_{laser}(1 - R_{laser})}{\sqrt{2\pi}\sigma_{laser}\, l_{laser}\, E_{laser}} \exp\left(-\frac{x}{l_{laser}} - \frac{1}{2}\left(\frac{t}{\sigma_{laser}}\right)^2\right) \tag{3.39}$$

where F_{laser} is the incident laser fluence, R_{laser} is the reflectivity, E_{laser} is the laser photon energy, σ_{laser} is the temporal pulse duration ($t_{FWHM} = 2\sqrt{2\ln 2}\,\sigma_{laser}$), and l_{laser} is the absorption depth of the laser light. The carrier relaxation and hot carrier transport are modeled by

$$\frac{dE_{carrier}}{dt} - \frac{d}{dx}\left(\frac{E_{carrier}}{N}D_a\frac{dN}{dx}\right) = E_{laser}S - E_{gap}(C_e + C_h)N^2(N - N_0) - \frac{E_{carrier} - 3Nk_BT_l}{\tau_{el-ph}} \quad (3.40)$$

where E_{gap} is the energy bandgap, T_l is the lattice temperature, τ_{el-ph} is the electron-phonon relaxation time (representing LO phonon emission), and

$$E_{carrier} = 2\left(\tfrac{3}{2}Nk_BT_e\right) \quad (3.41)$$

is the carrier energy, where T_e represents the carrier temperature. The factor of 2 in Equation 3.41 accounts for electron and hole energies. The carriers are assumed to thermalize on a very short time scale under high density excitation, due to carrier-carrier scattering [82]. This scattering thermalizes the electrons and holes to a common quasi-equilibrium temperature, well above the lattice temperature ($T_e \sim 10^4$ K). Equation 3.41 assumes that the carriers are distributed in a Boltzmann-like distribution [77]. Fermi-Dirac statistics should apply in principle [78]. However, the large photon energy (E_{laser} = 1.5 eV) compared to the energy bandgap of InSb (E_{gap} = 0.17 eV) makes the average deBroglie wavelength of the carriers at a quasi-thermalized temperature of $\sim 10^4$ K (~ 1.1 Å) smaller than the average inter-carrier spacing under high densities ($N^{-1/3} \sim 6$ Å, for $N \sim 5\times10^{21}$ carriers/cm^3). When the inter-carrier spacing is much greater than the deBroglie wavelength, the carriers act like an ideal gas, and Boltzmann statistics apply. Alternatively, the quasi-Fermi energy of the excited carriers is comparable to the average carrier energy, so that the Fermi-Dirac distribution ($f(E) = \{\exp[(E - E_F)/k_BT_e] + 1\}^{-1}$) is approximately a Boltzmann (or Maxwell) distribution ($f_B(E) = \exp(-E/k_BT_e)$) [83].

The carrier energy is transferred to the lattice by the combination of Auger

recombination and LO phonon emission. LO phonon emission is the dominant mechanism for transfer of energy in zincblende materials, due to strong Fröhlich coupling between electrons and the polar basis atoms [79]. While the LO phonon emission time is ~ 200 fs, the large number of phonon emissions (~ 50 meV) needed to reduce the carrier energy (~ 1 eV) makes the effective relaxation time longer (~ 2 ps) [79, 84]. Assuming no LO phonon propagation, the energy in LO phonons is given by

$$\frac{dE_{LO}}{dt} = \frac{E_{carrier} - 3Nk_BT_l}{\tau_{el-ph}} - \frac{E_{LO}}{\tau_{ph-ph}} \tag{3.42}$$

where E_{LO} is the energy in LO phonons, and τ_{ph-ph} is the LO phonon to acoustic phonon relaxation time. Although the LO phonon lifetime is ~ 4 ps [79, 85], τ_{ph-ph} is made longer to account for phonon thermalization as well. The lattice temperature evolution is then given by

$$\frac{dT_l}{dt} - \frac{d}{dx}\left(\frac{k_T}{C_l}\frac{dT_l}{dx}\right) = \frac{E_{LO}}{\tau_{ph-ph}} \tag{3.43}$$

where k_T is the lattice thermal conductivity, and C_l is the lattice heat capacity.

In order to simulate the nucleation at the surface and growth into the sample of the thermally expanded layer, an effective temperature profile used to determine lattice expansion is used. This effective temperature profile is simply modeled by the lattice temperature profile given by Equation 3.43 multiplied by a step function in x that has a width determined by the speed of sound in InSb ($c_s = 5 \times 10^5$ cm/s) multiplied by the time delay. The lattice thermal conductivity does not permit significant heat conduction into the sample on a ~ 100 ps time scale. In fact, phonon propagation under highly nonequilibrium conditions is expected to be quasi-ballistic, so that heat propagation into the sample

should travel at the speed of sound, and not be determined by diffusion. This quasi-ballistic propagation has been observed under low laser excitation ($<< 0.02$ W/cm^2) and at low temperature (1.2 K) in GaAs and InP [86].

Parameter	Reference	Value
Ambipolar diffusion coefficient, D_a	[88]	10^2 cm^2/s
Auger recombination coefficient, C_3	[89]	10^{-25} cm^6/s
Screened Auger recombination time constant (fixed above a carrier concentration of 10^{21}/cm^3)	[88]	2.6 ps
Laser fluence, F_{laser}		20 mJ/cm^2
Reflectivity, R_{laser}		0.3
Laser photon energy, E_{laser}		1.5 eV
Laser temporal pulse duration, σ_{laser}		50 fs (sigma)
Laser linear optical penetration depth, l_{laser}	[71]	100 nm
Bandgap energy, E_{gap}		0.17 eV
Electron-phonon relaxation time, $\tau_{el\text{-}ph}$	[79]	2 ps
Acoustic phonon generation and equilibration, $\tau_{ph\text{-}ph}$	[79]	10 ps
Lattice heat capacity, C_l	[90]	2 J/cm^3·K
Speed of sound, c_s	[90]	5×10^5 cm/s

Table 3.1: Parameters used in the simulation of laser heated InSb.

The coupled differential equations above are solved numerically. The parameters used in the simulation are summarized in Table 3.1. Equations 3.38 and 3.43 are solved using the Crank-Nicholson method [87], and Equations 3.40 and 3.42 are solved by inserting the appropriate values for coefficients at each time step and using the basic finite difference approach. The difference between the absorbed laser energy and the energy in the carriers, LO phonons, and lattice is monitored to ensure energy conservation in the calculations.

Shown in Figure 3.12 is an initial attempt to model the data, assuming a 2 ps

carrier energy relaxation time due to LO phonon emission and a 10 ps acoustic phonon

generation and equilibration time. The delayed onset of the increase in the signal is seen in

the simulation, although the magnitude of the delay does not quite match the

experimentally measured one.

Figure 3.13 shows the results of a similar simulation, but with screening of the

Auger recombination time constant taken into account. According to E. J. Yoffa [88],

screening should limit the Auger recombination time when the carrier density is $\sim 10^{21}$

carriers/cm^3. Using this, we assume that the Auger recombination coefficient is limited to

~ 2.4 ps above 10^{21} carriers/cm^3. The resulting simulation shows better agreement with the

data.
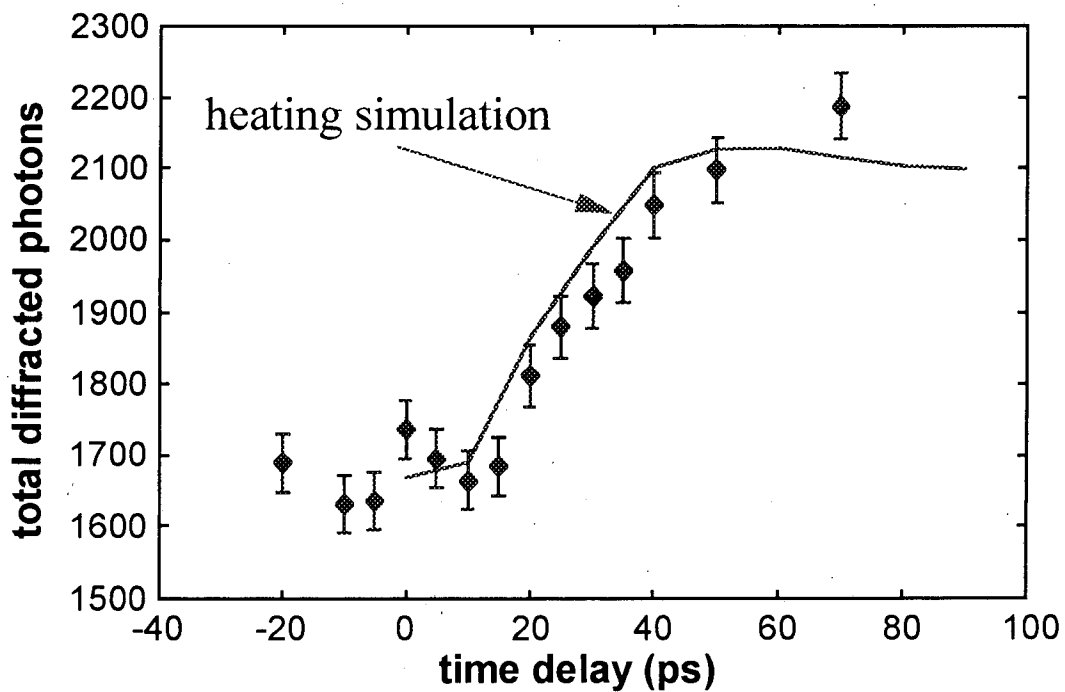
Figure 3.12: Laser heated InSb simulation compared to data.
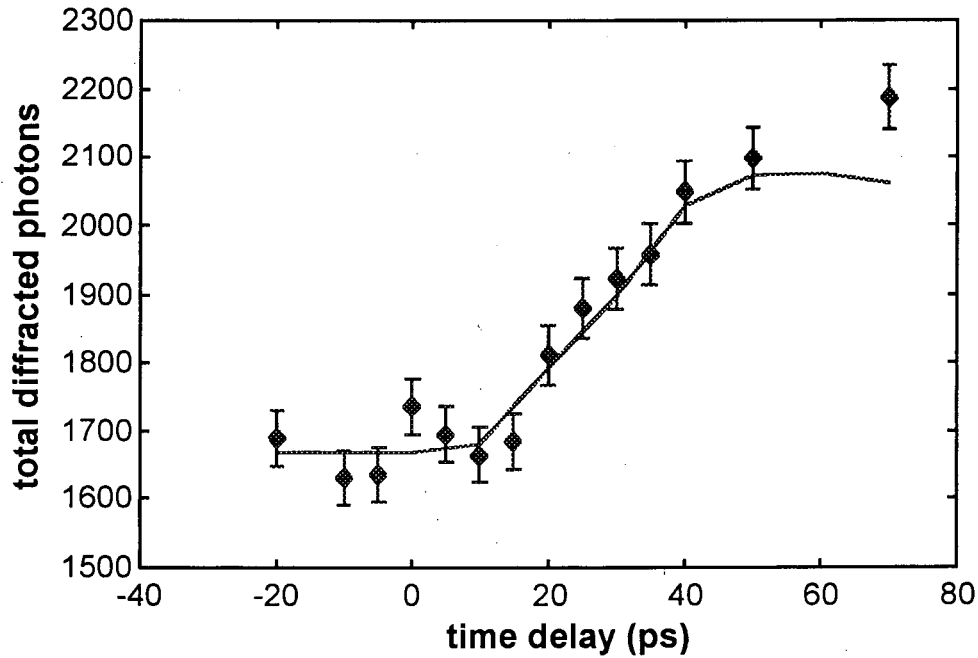
Figure 3.13: Laser heated InSb simulation accounting for a screened Auger recombination coefficient compared to data.

Indications of ultrafast disordering

Figure 3.14 shows finer time step data taken around zero time delay. The data

suggests a very abrupt (< 1 ps) transient reduction in the x-ray diffraction signal, as shown

in the fit to the data. A reduction in x-ray diffraction is indicative of disordering. Many

optical experiments have been performed on ultrafast disordering in Si [10, 11] and GaAs

[46, 64], all of which indicate that a high electron-hole plasma density induces lattice

instability [39-44, 91, 92]. The coherent phonon period in highly excited Tellurium show a

shift towards lower frequency with higher carrier density, indicating that bond softening is

beginning to occur [93]. A recent time-resolved x-ray diffraction cross-correlation

technique also indicates that disordering may be occurring in less than 2 ps [26]. At the

laser fluence used in our experiment, a carrier density of $\sim 4 \times 10^{21}/cm^3$ is estimated,

assuming the linear absorption depth (~ 100 nm) of 800 nm light in InSb. This should be

sufficient to induce ultrafast disordering in a thin layer at the surface [71]. This disordered layer does not contribute to the x-ray diffraction signal, but attenuates the number of x-rays entering and diffracting from the sample by photoelectric absorption. The magnitude of the decrease (~ 1.3%) indicates that ultrafast disordering is occurring in a very thin (~ 15 nm) surface layer due to the presence of a dense electron-hole plasma.
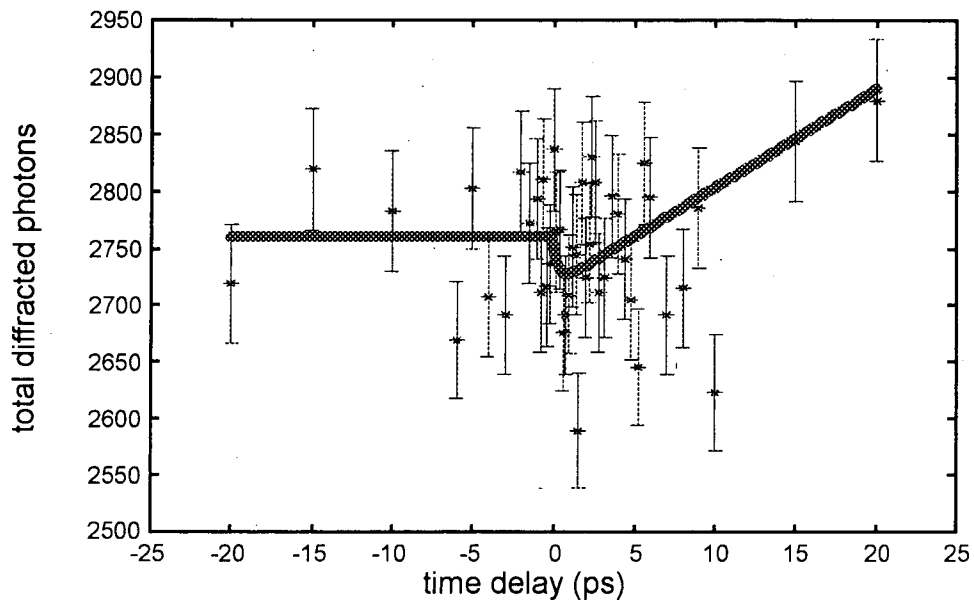
Figure 3.14: Indication of ultrafast disordering.

In order to achieve better overlap between the x-ray and laser penetration depths, we attempted to perform time-resolved x-ray diffraction using lower energy x-ray photon energy. The photon energy was lowered by reducing the electron beam energy. This was accomplished by turning off the second of two accelerating structures in the linac. The resulting reduction in electron beam energy (factor of 2 reduction in γ) resulted in a factor of 4 reduction in the x-ray photon energy (7.5 keV), along with a reduction in the x-ray flux (a factor of 4 reduction, due to a factor of 2 increase in beam divergence ~ $1/\gamma$). This decrease in x-ray flux, along with increased photoelectric absorption in air, caused the

number of diffracted x-rays to drop by about an order of magnitude. As a result, only a small amount of data could be obtained in a reasonable amount of time. Preliminary time-resolved x-ray diffraction data on InSb 12.8° off (111) (~ 0.5° angle of incidence for the 7.5 keV x-rays) is shown in Figure 3.15. The data is smoothed using a 1 point Gaussian smoothing function. The smoothed data seems to indicate that peak reduction and a low energy shoulder increase is present. This peak reduction would be consistent with the data of J. Larsson, et al. [26]. A peak reduction indicates disordering, while a low energy shoulder indicates lattice expansion. As a disordered layer is likely to introduce strain underneath it, the observation of both effects is certainly possible. Further improvements in the signal to noise are needed to make any conclusions.
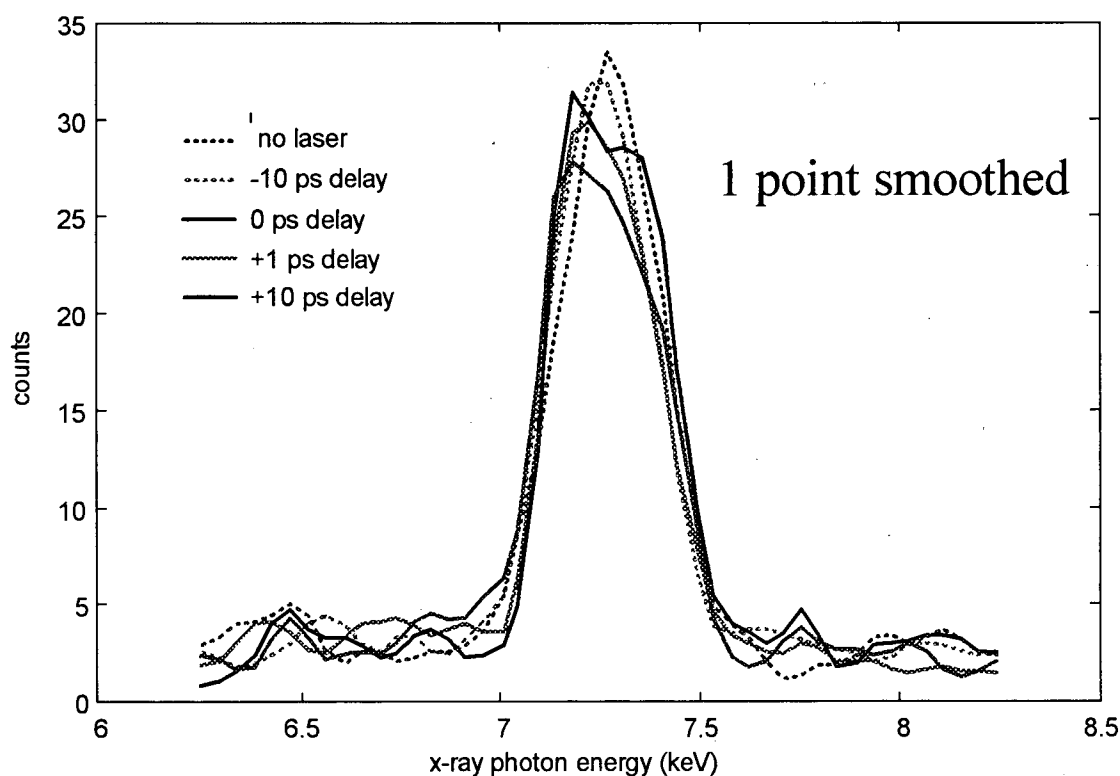
Figure 3.15: 7.5 keV x-ray photon energy time-resolved x-ray diffraction on InSb 12.8° off (111).

Laser-perturbed GaAs

In addition to the experiments performed on InSb, we also performed time-resolved x-ray diffraction (at 30 keV photon energy) on laser-perturbed GaAs crystals. As shown in Figure 3.16, the lattice dynamics of laser-perturbed GaAs 3.3° off (111) are very similar to those of laser-perturbed InSb 3.0° off (111). The fit to an exponential rise in Figure 3.16 shows that a delay (~ 10 ps) and a rise (~ 30 ps time constant) are present in the integrated x-ray diffraction spectrum from laser perturbed GaAs, indicating the presence of a thermally expanded layer propagating deeper into the sample. GaAs has a larger melting threshold than InSb, due to the larger laser penetration depth (~ 1 μm for GaAs at 800 nm). As a result, the laser excitation fluence used in the GaAs experiments was higher than the fluence used in the InSb experiments by about a factor of 5.
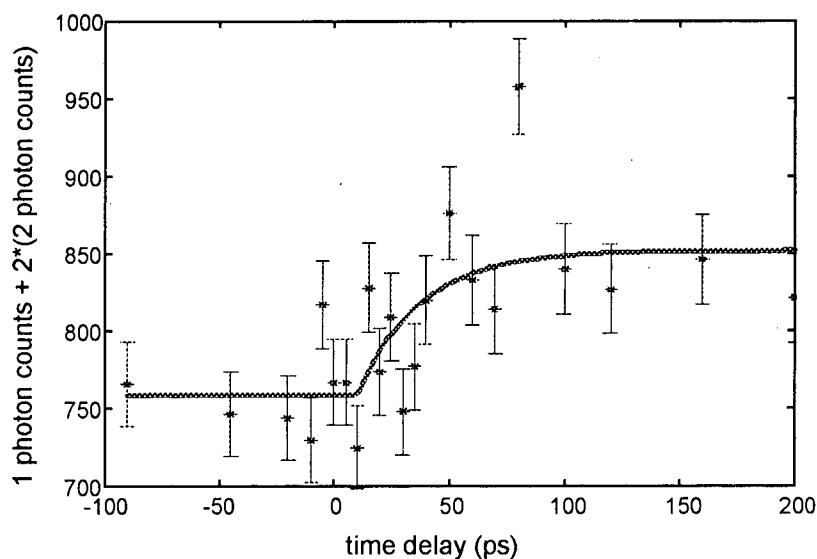
Figure 3.16: Laser-perturbed GaAs 3.3° off (111). The curve is a fit to an exponential rise, with a 10 ps delay and a 27.4 ps rise time.

In addition to performing time-resolved x-ray diffraction on asymmetric cut GaAs,

we attempted to observe lattice dynamics in symmetric GaAs (111). The data (shown in Figure 3.17) seems to show very similar dynamics to GaAs 3.3° off (111). This may be a consequence of the fact that the laser penetrates deeper into the sample. Although the x-rays penetrate more deeply into the sample in the symmetric crystal, because the laser is able to perturb a larger volume, the volume that the x-rays can probe still interacts with a large fraction of laser perturbed material.
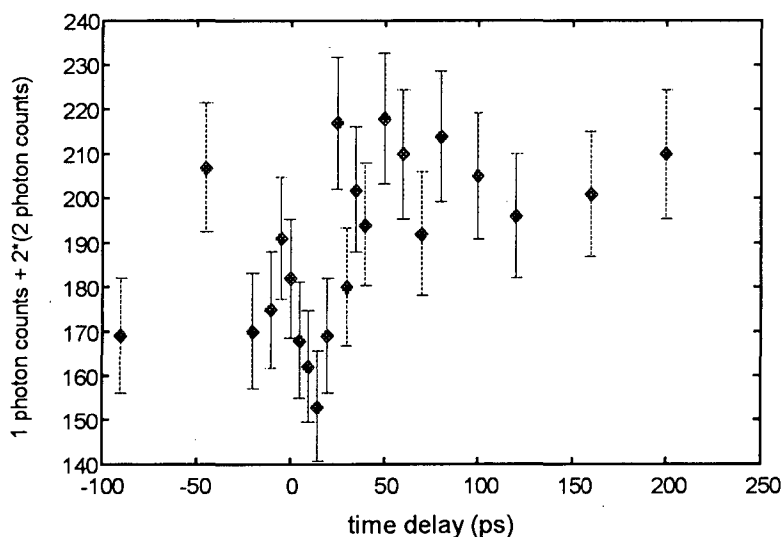
Figure 3.17: Laser-perturbed GaAs (111).

Using the right-angle Thomson scattering x-ray source, we obtained new insights into ultrafast lattice dynamics of laser-perturbed semiconductors. An interesting phenomenon of delayed lattice expansion is observed. This highly nonequilibrium condition can only be achieved using femtosecond laser pulse excitation, as carrier-phonon equilibration times are on the order of picoseconds. As a result, the right-angle Thomson scattering x-ray source is ideal for such studies. We also demonstrated the versatility of the source by performing time-resolved x-ray diffraction with lower x-ray photon energy.

Chapter 4: Femtosecond X-Ray Pulse Length Measurement

In order to perform time-resolved x-ray experiments using ultrashort x-ray pulses, the pulse duration must be known. To date, streak cameras have been used to measure x-ray pulse durations, but they typically have picosecond resolution [94, 95]. More recently, laser-assisted photoemission has been used to measure the duration of soft x-ray pulses from high-order harmonics with subpicosecond resolution [22]. This method is also a promising technique for measuring the duration of ultrashort hard x-ray pulses. A related method, laser-assisted Auger decay, has also been used to put an upper limit on the pulse duration of laser-produced plasma x-rays [96]. Autocorrelation of extreme ultraviolet high-order harmonic pulses by using two photon ionization in a gas can in principle be applied to x-ray pulses [97]. In this chapter, the laser-assisted photoelectric effect (LAPE) and its application to ultrashort x-ray pulse duration measurement will be discussed.

Laser-Assisted Photoelectric Effect

In the normal photoemission process, a bound electron is emitted from a solid, molecule, or atom by absorbing a photon with energy greater than the binding energy of the electron. The resulting photoelectron has a kinetic energy that is equal to the difference between the photon energy and the binding energy of the electron. The presence of a high-intensity laser pulse during the photoemission process can cause modifications to the photoelectron energy spectrum, which may be referred to as the Laser-Assisted Photoelectric Effect (LAPE) [22]. As shown in Figure 4.1, one modification is due to the ponderomotive potential of the intense laser field. Another modification is the absorption

and emission of laser photons, which causes sidebands to form in the photoelectron spectrum. Either of these modifications can be used to cross-correlate ultrashort x-ray and laser pulses, since they depend on the presence of both pulses.
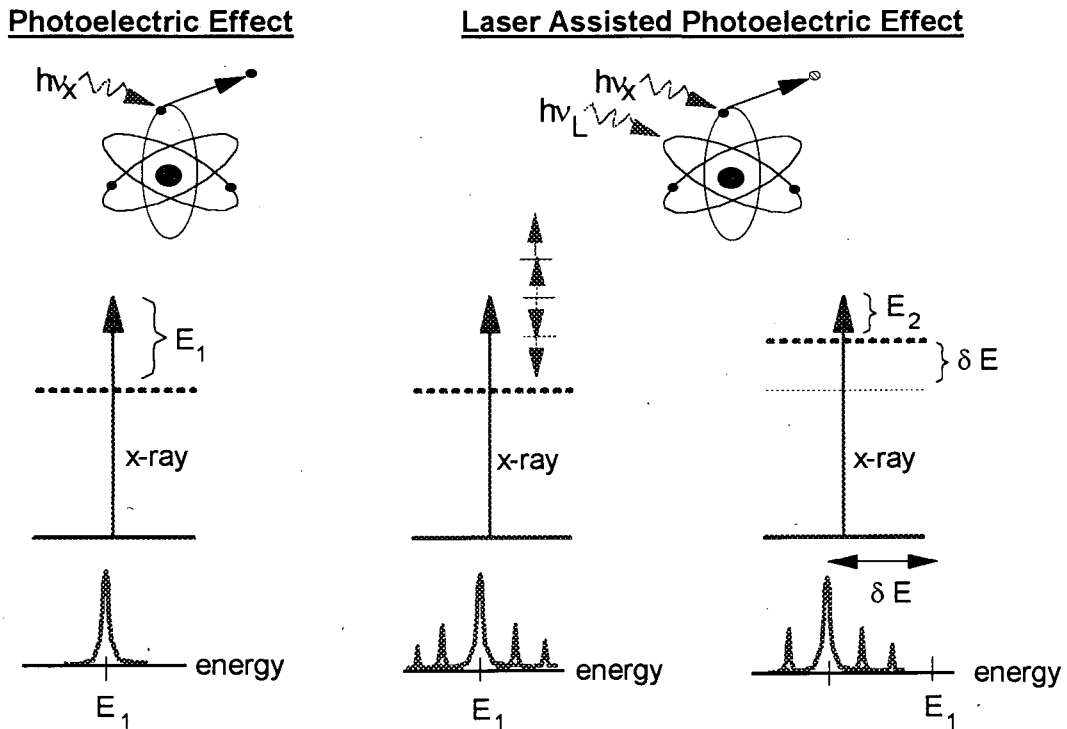
Figure 4.1: Laser-assisted photoelectric effect (LAPE).

Theory

The most apparent LAPE modification is the absorption and emission of laser photons caused by the intense laser field. An analytical expression for the probability of absorption (n > 0) or emission (n < 0) of laser photons may be obtained with the use of reasonable assumptions. One assumption is that the ground state of the electron is not significantly modified by the laser field, and is hydrogen-like in character. This assumption is reasonable for noble gases, because the outer shell electron essentially sees a uniform

single positive charge core. Also, the intensity at which absorption and emission of photons occurs is relatively small, so that the ponderomotive potential of the laser field is much less than the electron binding energy. The other assumption is that the final electronic states in the presence of the laser field are well described by Volkov states. As Volkov wavefunctions are free electrons in the presence of an electromagnetic field, and the photoemitted electrons are closer to free electron states for higher photoemission energies, this approximation becomes better for high-energy photoelectrons. The effect of the ponderomotive potential on the photoelecton spectrum is incorporated as a shift in the binding energy of the electron.

To simplify the expression for the probability of photoemission with absorption or emission of laser photons, the following electron momenta expressions are used (following T. E. Glover, et al. [22]):

$$p = \sqrt{2m(\hbar\omega_x + n\hbar\omega - E_b - U_p)} \tag{4.1}$$

and

$$p_0 = \sqrt{2m(\hbar\omega_x - E_b)} \tag{4.2}$$

where m is the mass of the electron, $\hbar\omega_x$ is the x-ray photon energy, $\hbar\omega$ is the laser photon energy, E_b is the electron binding energy without the presence of the laser field, and

$$U_p = \frac{e^2 A_0^2}{4mc^2} = \left(\frac{2\pi e^2}{mc}\right)\left(\frac{I}{\omega^2}\right) \tag{4.3}$$

is the ponderomotive potential of the laser field, where A_0 is the magnitude of the vector potential, I is the intensity of the laser field, e is the charge of the electron, c is the speed of light, and ω is the laser frequency. Equation 4.1 incorporates the effect of the

ponderomotive potential of the laser field as an additional binding energy, causing a reduction in the photoelectron kinetic energy. Using the above assumptions and definitions, the probability for absorption ($n > 0$) and emission ($n < 0$) of n laser photons during the photoemission process is given by (calculating the scattering matrix in the radiation gauge)

$$A_n = (3/2)\left(\frac{p}{p_0}\right)^3 \left[\frac{1+(ap_0/\hbar)^2}{1+(ap/\hbar)^2}\right]^4 \times \int_0^\pi \sin(\Theta)\cos^2(\Theta)J_n^2(\alpha,\beta)d\Theta \qquad (4.4)$$

where $a = a_{Bohr}/eZ_{core} = \hbar^2/m_e e^3 Z_{core}$, and eZ_{core} is the effective nuclear charge the photoemitted electron sees in its ground state. The arguments of the generalized Bessel function, $J_n(\alpha,\beta)$, are given by $\alpha = eA_0 p\cos(\Theta)/mc\hbar\omega$ and $\beta = - U_p/2\hbar\omega$.

Laser scattering probability
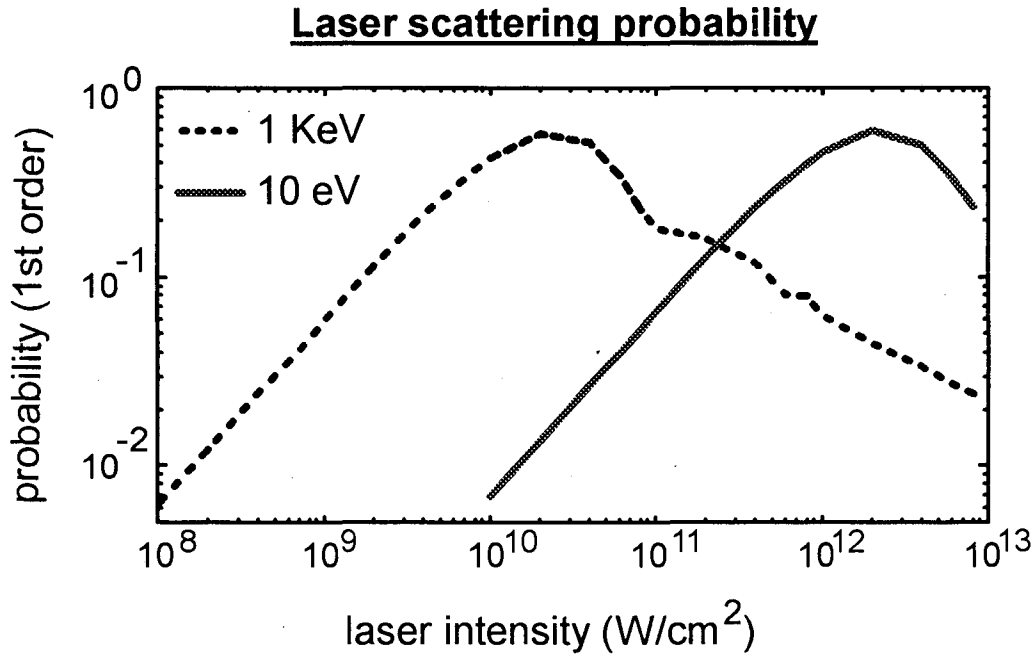
Figure 4.2: Laser scattering probability for one photon interaction as a function of laser intensity for 1 keV (dotted line) and 10 eV (solid line) photoelectrons.

Numerous sidebands may be observed with high enough laser intensity. However,

the appearance of multiple sidebands indicates the saturation of the LAPE laser photon absorption and emission modification. For x-ray pulse duration measurements, it is helpful to keep the sideband amplitude linear with laser intensity. This allows for direct extraction of the x-ray pulse duration from the amplitude of a sideband as a function of time delay between the laser and x-ray pulses. Otherwise, deconvolution of the intensity dependence of the sideband amplitude needs to be performed to extract the x-ray pulse duration.

Because the formation of sidebands is a result of the $\vec{p} \bullet \vec{A}$ term in the Volkov wavefunction, the laser scattering occurs with less laser intensity for photoelectrons with higher momentum. This scaling can be seen from Equation 4.4, and using the fact that $J_n(\alpha, \beta) \propto \sqrt{\alpha}$, for $\alpha \ll 1$. Since α is proportional to $A_0 p$ (from the $\vec{p} \bullet \vec{A}$ term), the scattering probability, A_n, is also proportional to $A_0 p$, for $\alpha \ll 1$. As shown in Figure 4.2 (n=1 case), for a given laser vector potential A_0 (i.e. a fixed ponderomotive potential, U_p, and therefore a fixed β), a higher photoelectron momentum results in a higher scattering probability. Therefore, harder x-rays pulses can be measured using this method. However, a higher x-ray flux may be needed to compensate for the smaller x-ray absorption cross-section of harder x-ray photons (the x-ray absorption cross-section scales as $(\hbar\omega_x)^{-3}$ for x-ray photon energies above an absorption edge).

The other LAPE modification to the photoelectron spectrum is the shift in the photoelectron energy due to the ponderomotive potential of the laser field. This shift can also be considered as the extra energy required for the photoemitted electron to be in a state of oscillation in the electric field of the laser. As seen in Equation 4.3, the ponderomotive potential is linear in the intensity of the laser field. Thus, the

ponderomotive potential shift can also be used as a simple way to extract x-ray pulse durations. Using the ponderomotive potential shift to measure x-ray pulse durations has the advantage of not being a saturable effect, making it applicable over a wide range of laser intensities. However, fairly large laser intensities ($\sim 10^{13}$ W/cm^2) are needed to produce reasonable photoelectron energy shifts (~ 1 eV). Therefore, either a photoelectron energy detector with good energy resolution or a very high laser intensity is needed to use the ponderomotive shift. These alternatives may not be as practical as monitoring the sideband amplitudes.

High-Order Harmonic X-Ray Pulse Duration Measurement

In order to test the LAPE method as a means of x-ray pulse measurement, a known source of ultrashort x-ray pulses is needed. The right-angle Thomson scattering source is a candidate, as it generates subpicosecond hard x-ray pulses. However, hard (> 10 keV) x-ray pulses have the problem of small absorption cross-section. Use of soft x-rays is therefore a better candidate for initial tests of the LAPE x-ray pulse duration method. As high-order harmonic generation is capable of producing ultrashort soft x-ray pulses, and the physics of the generation process is still under investigation, we chose to test the LAPE method of x-ray pulse measurement by measuring high-order harmonic x-ray pulse durations.

High-order harmonic generation

High-order harmonic generation has been studied for several years now. Harmonic photon energies > 100 eV can be generated by using high-intensity laser pulses

propagating in noble gases [98, 99]. High-order harmonics are the result of non-perturbative excitation of atomic electrons, i.e. the ponderomotive potential of the laser field, U_p, is on the order of the atomic binding energy. The harmonic generation process can be viewed in the semi-classical picture developed by P. B. Corkum [100]. In this picture, the intense laser field causes electrons to oscillate through the anharmonic atomic potential. The resulting electron motion has very high frequency components that result in the emission of many harmonics of the driving field. High-order harmonic spectra typically have a sharp decrease in intensity for harmonics up to the 9th harmonic, and a fairly constant intensity from there up to $\sim 3U_p$, where the harmonic yield dramatically drops off. The region of approximately constant harmonic yield is known as the plateau region or cutoff region.

One may expect that the high-order harmonics generated by ultrashort laser pulses also have ultrashort pulse durations. This can be seen by considering the atomic dipole response to an intense laser field. Using the simple atomic model of W. Becker, et al. [101], the single atom dipole response can be estimated. An example of such a calculation is shown in Figure 4.3 for the 23rd harmonic from intense 800 nm laser excitation of Argon. The nonlinearity of harmonic yield versus laser intensity, I_{laser}, is initially in the perturbative regime, and behaves as $(I_{laser})^q$, where q is the harmonic order (number of harmonics of the fundamental). As the laser intensity approaches the cutoff intensity, the effective nonlinearity, q_{eff}, reduces, and approaches a value ~ 5. Significant high-order harmonic yield for a single atom occurs when the laser intensity is greater than the cutoff intensity, i.e. when the harmonic in question lies in the plateau region. For *peak* laser intensities around the cutoff intensity, since the temporal profile of the harmonics should

be $\sim (I_{laser})^q$, the high-order harmonic pulse duration from a single atom is expected to be less than the laser pulse duration. When the peak laser intensity is around the ionization intensity, a quenching of harmonic yield occurs because ionization removes the electron
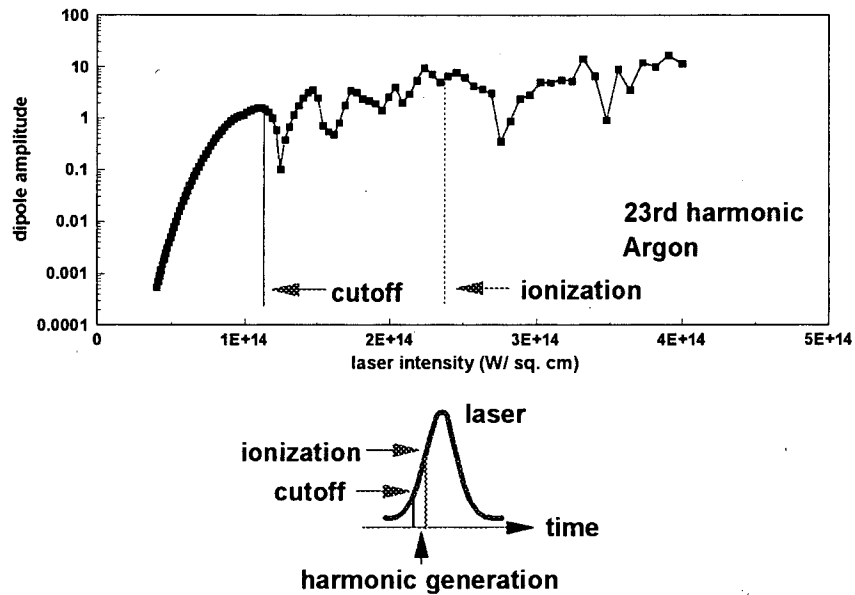
Figure 4.3: Calculated dipole amplitude of a high-order harmonic (23rd) as a function of driving laser intensity.

from the atom. Since the accelerated electron is no longer able to experience the anharmonic potential of the atom, harmonic production stops. Harmonics are then generated only during the leading temporal edge of the laser pulse, before ionization occurs. The net effect, schematically shown in Figure 4.3, is that when the *peak* laser intensity is above the ionization intensity, the pulse duration of high-order harmonics can be significantly shorter than the laser pulse duration, due to the narrow range of intensities where significant harmonic yield is produced.

Experimental setup

Using the laser assisted photoelectric effect, we measured the pulse duration of the 21st (33 eV) through 27th (42 eV) harmonics generated in argon gas by intense laser light [22]. The experimental apparatus is schematically shown in Figure 4.4. The terawatt laser system described in Chapter 2 is used to generate 800 nm, 70 fs pulses. These pulses are sent through a beamsplitter, with one beam (modifying beam) being sent out of the vacuum chamber, through a delay arm (to provide temporal overlap), focused with a lens, and sent back into the vacuum chamber to be overlapped with the high-order harmonics from the other beam. This other beam (generating beam) is focused to an intensity of ~ 10^{15} W/cm^2 in argon gas at the exit of a gas valve. The argon gas is pulsed through this gas valve to a density of ~ 10^{18} atoms/cm^3. Harmonics generated at this point propagate ~ 2 m through a 150 nm thick Al filter (to block the co-propagating generating beam) to a Mo:Si multilayer coated curved mirror. This multilayer mirror has a peak reflectivity of 22% at 38 eV, with a 4 eV (FWHM) bandpass.

The harmonics reflected by this multilayer mirror are focused to the output of another gas valve to a spot size ~ 20 μm. This gas valve outputs helium at a pressure between ~ 0.1 Torr to 1 Torr. This pressure is adjusted to yield the maximum photoelectron signal without broadening of the photoelectron peaks due to space charge effects. The photoelectrons generated by the harmonic photons absorbed in the helium gas are collected using a time of flight preserving pair of reflecting parabolic grids. These grids collect photoelectrons over a large solid angle and direct them through a ~ 1 m field-free flight tube to a microchannel plate detector. The photoelectron energy is determined by the time of flight of the photoelectrons through the flight tube using a 2 GS, 500 MHz
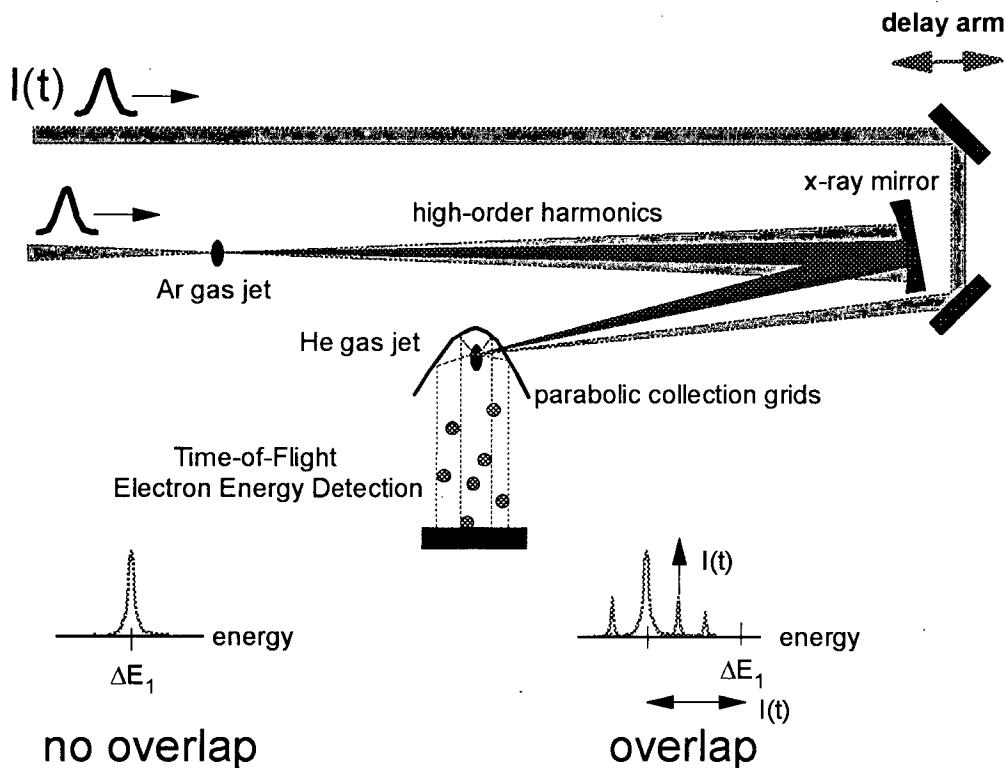
Figure 4.4: Laser-assisted photoelectric effect (LAPE) experimental setup.

digitizing oscilloscope (Tektronix TDS 620). The modifying beam, sent back into vacuum

through a 4 mm diameter window in the multilayer mirror, causes the LAPE modifications

to the photoelectron spectrum. The modifying beam is focused to a spot size of ~ 450 μm

at the exit of the helium gas valve, providing an intensity of up to $\sim 10^{13}$ W/cm^2.

Experimental results

Shown in Figure 4.5 are a typical unperturbed photoelectron spectrum along with

a spectrum showing the LAPE modifications caused by the high-intensity modifying laser

beam. For a modifying laser pulse with this intensity, both the laser scattering and

ponderomotive potential shift effects are present. Using the LAPE theory above, and

convolving the resulting scattering probabilities with the unperturbed photoelectron
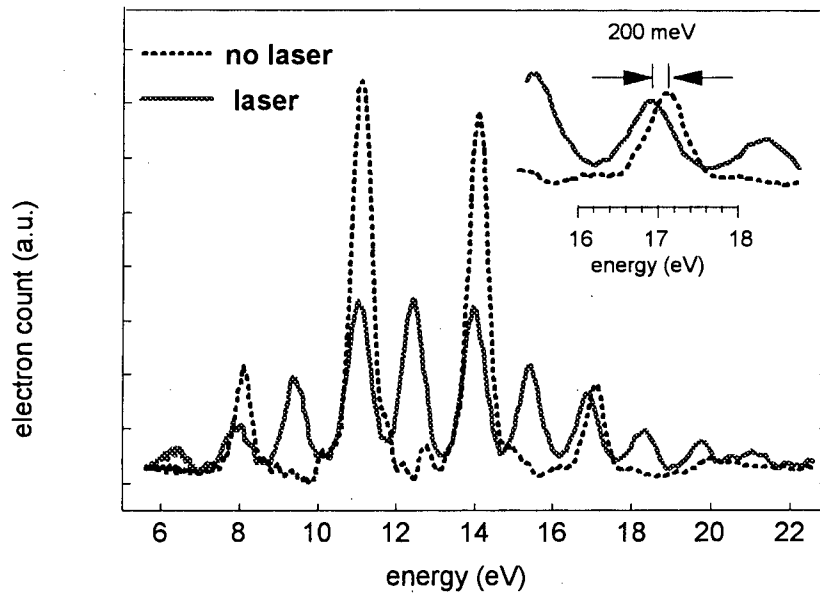
Figure 4.5: Photoelectron spectra without (dotted line) and with (solid line) LAPE modifications induced by an intense laser pulse.
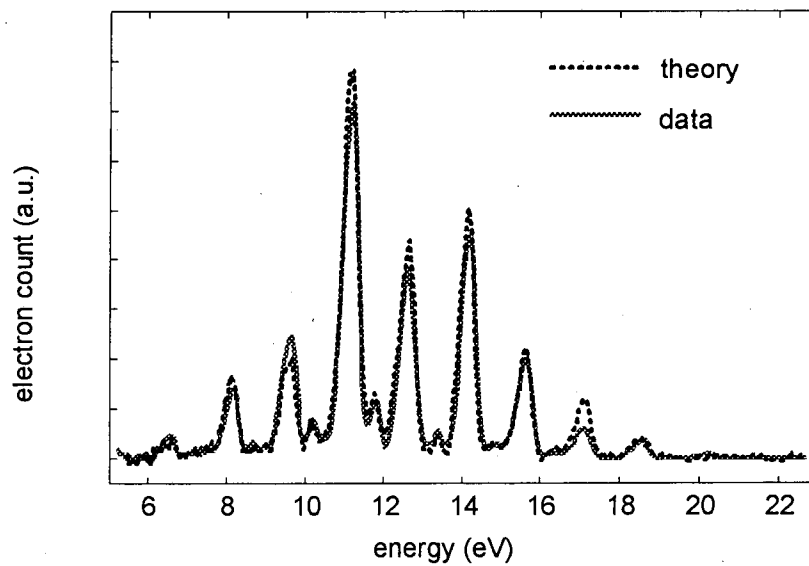
Figure 4.6: Comparison of LAPE theory (dotted line) to experimental data (solid line).

spectrum, a comparison of theory and experiment can be made. As shown in Figure 4.6, the agreement is quite good. This indicates that core potential effects can be neglected under these conditions. For lower photoelectron energies, i.e. for photoelectrons closer in

energy to the bound continuum states, core potential effects may play a more important

role, and the use of simple Volkov wavefunctions may no longer be valid.
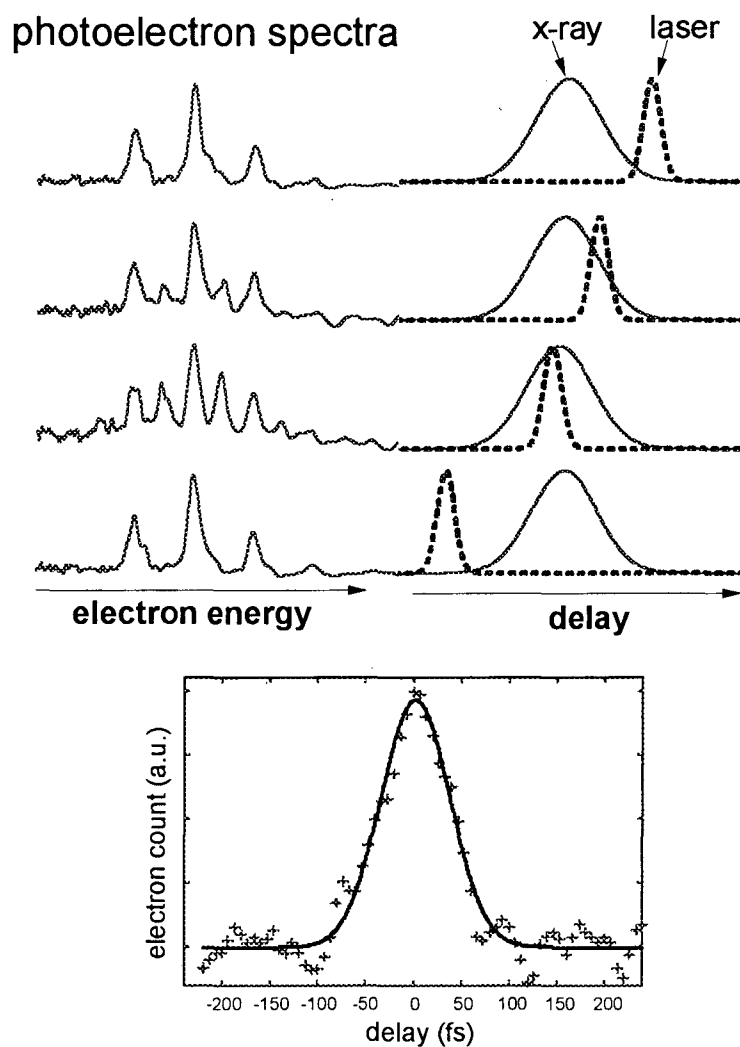
Figure 4.7: Cross-correlation of laser and high-order harmonic x-ray pulses. The first order sideband amplitude as a function of time delay is represented by crosses. The solid curve is a Gaussian fit to the data.

By measuring the magnitude of the sidebands or the ponderomotive shift as a function of

time delay between the x-ray pulse and the modifying laser pulse (i.e. by performing a

cross-correlation between x-ray and laser pulses), the pulse duration of the x-rays can be determined. This cross-correlation is shown schematically in Figure 4.7, with a typical cross-correlation (monitoring the sideband amplitude) between ultrashort laser and high-order harmonic pulses shown in the plot on the bottom of the figure. The pulse duration of the high-order harmonic x-rays are seen to be ultrashort, as expected. Extending this x-ray pulse measurement technique to the higher energy x-rays is possible in principle.

Macroscopic Effects in High-Order Harmonic Generation

Besides being a means of ultrashort x-ray pulse measurement, the LAPE effect can be used to elucidate some of the physics of high-order harmonic generation [22]. Ideal experiments would be able to measure the harmonic emission from a single atom in the presence of an intense laser field. Practically, reasonable harmonic yield is obtained by observing high-order harmonics from a macroscopic ensemble of atoms. Therefore, one needs to account for macroscopic effects in order to understand the single atom high-order harmonic generation process. For example, macroscopic phase-matching effects, such as propagation in an ionized medium, are important in determining the overall efficiency of the harmonic generation process. The relative importance of phase matching relative to the single atom response is not well known. The spatial and temporal profile of the generating laser pulse can also have a significant effect on the observed high-order harmonics. As mentioned earlier, significant high-order harmonic generation occurs in a limited intensity range - a minimum intensity is needed for harmonic generation, but ionization cuts off the generation. Because laser beams typically have Gaussian spatial profiles, there will be spatial and temporal dependence on laser intensity. The intensity in

the spatial wings of the laser beam will reach the high-order harmonic generation regime at

a later time than at the center of the beam. If the high-order harmonic generation and

phase matching processes are uniform across the laser beam, with only the intensity

dependence described above, then one expects that the high-order harmonic pulse duration

Importance of Spatial Laser Profile

(a)

Calculated harmonic pulses for laser with :

flattop laser spatial profile ———gaussian laser spatial profile

(b)
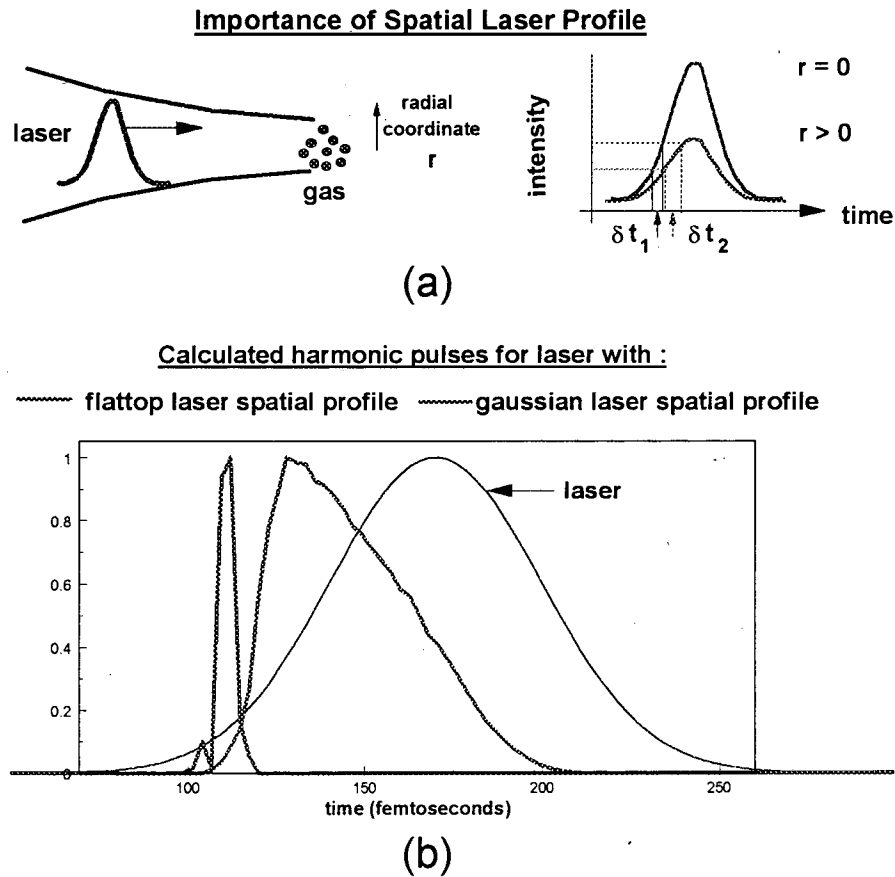
Figure 4.8: Spatial profile effects on the harmonic generation process. (a) illustrates temporal broadening due to spatial intensity variation. (b) compares high-order harmonic temporal profiles for Gaussian and flat-top laser spatial profiles.

will appear to be longer than the generation process actually allows it to be. Figure 4.8 (a)

illustrates the different positions in time for which the range of intensities harmonic

generation occurs (for a laser beam with a spatial profile that drops off radially). Figure

4.8 (b) compares the expected high-order harmonic temporal profile for a laser beam with a Gaussian spatial profile and a flat-top spatial profile.

Experimental results

One way to evaluate the temporal broadening effects of spatial wings in the driving laser pulse on the high-order harmonic pulse duration is to introduce an aperture that clips the spatial wings of the laser pulse. Cross-correlation measurements were performed without aperturing, and with apertured laser beams (800 nm, 110 fs) by imaging the aperture (90% diameter transmission) onto the harmonic gas jet. The experimental setup used for these experiments is a slightly modified version of the setup used for high-order harmonic pulse duration measurements described above. Measurements for a given laser intensity were taken under identical laser alignment and delay stage positions. The laser intensity was adjusted to keep the apertured and unapertured laser beam intensities the same at the harmonic generating gas jet (Argon) and at the cross-correlation gas jet (Helium). Cross-correlation measurements of the 25th harmonic taken at 2.4×10^{14} W/cm^2 (weakly ionized medium) are shown in Figure 4.9 (a), and at 1.1×10^{15} W/cm^2 (strongly ionized medium) in Figure 4.9 (b). The apertured data sets (open circles) are both shorter correlations and are shifted temporally compared to the unapertured cross-correlations (diamonds). Deconvolved harmonic pulse durations from an unapertured laser beam are 55 fs and 110 fs for the weakly and strongly ionized cases, respectively. The deconvolved harmonic pulse durations from an apertured laser beam are < 40 fs and 75 fs for the respective weakly and strongly ionized cases.

97
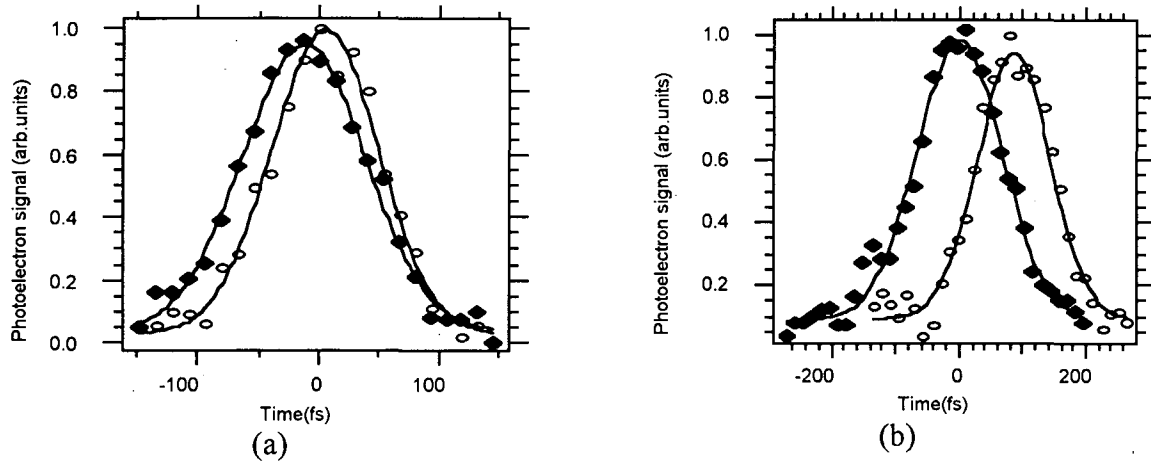
Figure 4.9: Spatial aperturing effects on the temporal broadening of high-order harmonics for laser intensities of (a) 2.4×10^{14} W/cm^2 (weakly ionized medium), and (b) 1.1×10^{15} W/cm^2 (strongly ionized medium). Diamonds = unapertured laser beam. Open circles = apertured laser beam.

The data indicate an increase in the effective harmonic pulse duration with intensity, contrary to the single atom response described above. This may be explained by the combination of two factors. First, temporal broadening is caused by the delayed increase in intensity in the spatial wings of the laser pulse. This effect can be calculated using the single atom response model of M. Lewenstein, et al. [102], and propagating the different atomic responses (due to the spatial and temporal laser profiles) using a fast Hankel transform algorithm to calculate the three-dimensional phase-matching integral. The calculation indicates that the curvature of the Gaussian wavefronts tend to spoil the phase-matching in the spatial wings. Therefore, another mechanism must be in effect to spoil the phase-matching on axis, thereby increasing the importance of the temporal broadening due to the spatial wings. This mechanism can be attributed to ionization on axis, where the laser intensity is highest. The significant pulse shortening with aperturing of the spatial wings supports this picture. The shift in the cross-correlation peak

corresponds to a shift earlier in time, which is also consistent with the fact that the spatial wings of the laser contribute to harmonic generation at later times relative to harmonics generated on axis. As the spatial wings are more important in the more strongly ionized medium, clipping the spatial wings has a larger effect on the pulse duration of the generated harmonics for the strongly ionized medium.

These experiments clearly show that macroscopic effects must be considered when interpreting high-order harmonic generation in terms of the single atom response. In particular, the temporal duration of high-order harmonics is thought to be sub-femtosecond in duration, but macroscopic phase matching and the spatial and temporal profiles of the generating laser pulse tend to mask this fact in the macroscopic high-order harmonic pulse. These macroscopic effects also need to be accounted for when interpreting the efficiency versus harmonic order.

Chapter 5: Future Prospects in Ultrashort X-Ray Pulse Science

In order to study a wide variety of ultrafast structural dynamics in condensed matter using x-ray spectroscopy, continued development of ultrashort x-ray pulse sources and ultrafast x-ray detectors will be required. This development will lead to x-ray sources with sufficient flux and/or x-ray detectors with sufficient temporal resolution to perform a wider variety of ultrafast x-ray spectroscopies. These time-resolved spectroscopies include x-ray diffraction, x-ray absorption techniques (e.g. EXAFS), and x-ray photoelectron diffraction.

Ultrashort X-Ray Pulse Source and Ultrafast X-Ray Detector Development

Several techniques are being considered to generate femtosecond x-ray pulses with higher peak or average spectral brightness. One possibility is to improve the laser and electron beam performance in the Thomson scattering x-ray source [33]. Another is to use a femtosecond laser pulse interacting with an electron bunch in a wiggler. The laser accelerates a femtosecond slice of electrons from the longer electron bunch, which is then spatially separated using an energy dispersive element, such as a bend magnet [25]. Slicing out x-ray pulses using a fast switch, such as x-ray diffraction from semiconductors undergoing ultrafast disordering is another means of utilizing storage ring facilities to provide ultrashort x-ray pulses [26]. Femtosecond electron bunch generation using advanced linear accelerators [103, 104] or using laser wakefield acceleration [105, 106] is also being pursued. These femtosecond electron bunches can be used to seed an x-ray free electron laser or for use in a Thomson scattering x-ray source. Laser-produced plasma and

high-order harmonic generation sources are still being developed. Some or all of these techniques may provide experimentally useful ultrashort x-ray pulses in the future.

An alternative to ultrashort x-ray pulse generation is to have ultrafast gating of the x-ray detector. One possibility for femtosecond gating is the laser assisted photoemission technique, which has already been demonstrated as a means of measuring ultrashort x-ray pulse widths. X-ray streak cameras have long been used to time resolve ultrashort x-ray processes, and are currently being developed to provide subpicosecond temporal resolution [94, 95]. These and other possible ultrafast gating techniques allow the use of longer x-ray pulses, such as from synchrotrons, which provide other benefits (highly collimated, tunable, high flux, etc.) that femtosecond x-ray sources may not be able to provide.

Scaling of the Thomson scattering x-ray source

As mentioned above, the small Thomson scattering cross-section requires the use of terawatt laser pulses and high-brightness electron beams in order to generate a reasonable number of x-rays. The number of x-ray photons generated scales linearly with the number of photons and the number of electrons interacting. The terawatt laser system in the current Thomson scattering x-ray source provides ~ 90 mJ of laser energy at the interaction point. Currently, terawatt laser systems can provide ~ 1 J of laser energy after compression [107], and future developments will provide even higher pulse energies. This leads to potential scaling of x-ray flux of at least an order of magnitude. The linear accelerator currently used to generate the electron bunches only operates at a maximum repetition rate of 5 Hz. State of the art linear accelerators can run at ~ 100 Hz repetition

rates, thereby providing another order of magnitude increase in flux. Using the linear accelerator at the ALS, the relatively large beam emittance causes a large angular spread at the electron beam focus that increases the bandwidth and divergence of the x-rays, thereby reducing the flux. Also, only a small portion of the long (~ 30 ps) electron bunch is involved in the x-ray generation process. With state of the art linear accelerators, lower emittance and shorter bunch lengths will provide additional increases in x-ray flux using Thomson scattering. Alternatively, higher flux may be obtained by using high-repetition rate laser and electron beams. A small storage ring and a high repetition rate laser system can be used to generate low peak flux, high average flux x-rays for experiments where high pulse energies are not acceptable for the sample under consideration.

Consider what might be done with state of the art laser and accelerator technology. Lasers generating 2 J, 100 fs laser pulses at a 10 Hz repetition rate are certainly possible. Current linac technology, with a photocathode generating the electrons, can produce ~ 1 nC, ~ 1 ps electron bunches at 10 Hz or higher repetition rates. Using these numbers, and Equation 2.5, assuming a 90 μm electron beam waist, the estimated number of scattered x-rays that can be generated is ~ (8 × 10^{18} photons)(6 × 10^9 electrons)(6.65 × 10^{-25} cm^2)(300 × 10^{-15} sec)/((π/4)(9 × 10^{-3} cm)^2(1 × 10^{-12} sec)) = 2 × 10^8 photons. Assuming an order of magnitude better electron beam emittance by using a photocathode injected linear accelerator compared to the thermionically injected ALS linac, the relative bandwidth should be ~ 3%, limited by the bandwidth of the laser pulses. Assuming a 50 MeV electron beam (~ 10 mrad x-ray divergence), this leads to a peak spectral brightness of ~ 6 × 10^6 photons/pulse/mm^2/$mrad^2$/(0.1% bandwidth). This is a significant improvement over the peak spectral brightness of 400 photons/pulse/mm^2/$mrad^2$/(0.1% bandwidth) for the

current right-angle Thomson scattering x-ray source. This increased peak spectral brightness would make the source ideal for single-shot time-resolved x-ray diffraction experiment. This type of experiment is particularly suited for studying irreversible laser-induced phase transitions in condensed matter. With pulses generated at 10 Hz, the average spectral brightness is expected to be ~ 6 × 10^7 photons/sec/mm²/mrad²/(0.1% bandwidth). At this level of spectral brightness, one can begin to consider performing time-resolved EXAFS experiments using the right-angle Thomson scattering x-ray source.

Femtosecond electron bunch slicing

Another possibility for generating ultrashort x-ray pulses in the future is femtosecond electron bunch slicing in a storage ring [25]. This source would take advantage of the desirable properties of synchrotron radiation from storage rings (high brightness, tunability, and existing beamline facilities) while providing femtosecond x-ray pulses at a high repetition rate (limited by the laser system). The idea is schematically shown in Figure 5.1. A femtosecond laser pulse co-propagates with the longer electron bunch in a wiggler. When the wiggler is adjusted to generate radiation at the laser wavelength, the laser can provide acceleration to a slice of the electrons interacting with the femtosecond laser bunch, as schematically shown in Figure 5.2. The resulting net acceleration that this slice of electrons experiences results in a change of electron energy for that slice, which can be spatially separated in a dispersive element, such as a bend magnet. This femtosecond electron beam slice can then be sent through a bend magnet, wiggler, or undulator to provide a femtosecond x-ray pulse. Because the slice of electrons generates x-rays in the same fashion as the longer pulse would, this femtosecond x-ray

pulse has all of the advantageous properties (small divergece, high brightness, high

repetition rate, etc.) of the longer storage ring synchrotron radiation.
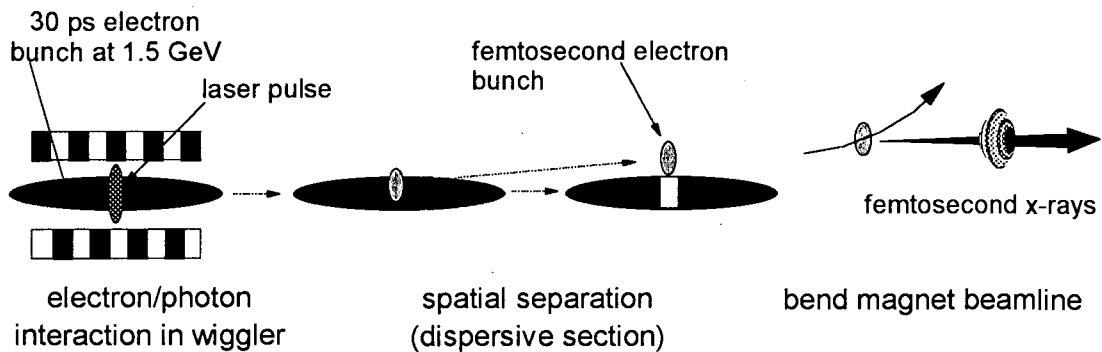
Figure 5.1: Electron bunch slicing in a storage ring.
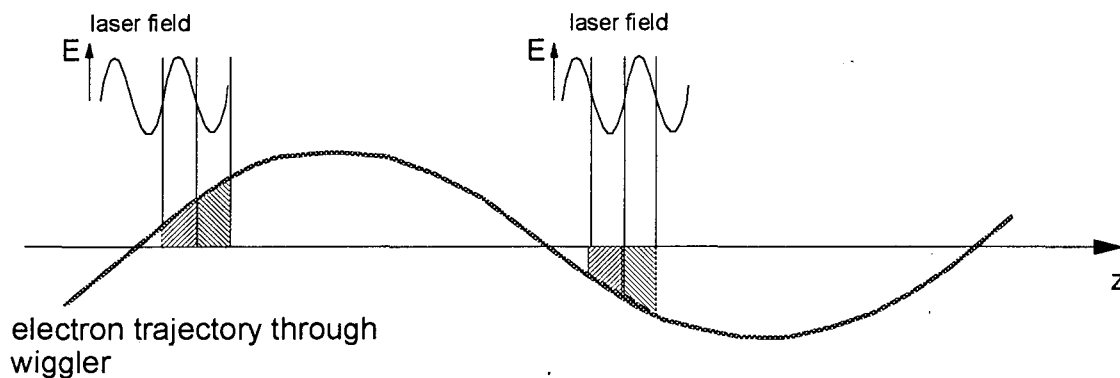
Figure 5.2: Acceleration of an electron slice in a wiggler with a co-propagating laser pulse.

Gated x-ray detection

Another way to utilize storage ring synchrotron radiation and provide femtosecond

time resolution is by using an x-ray detector gated on a femtosecond time scale. One way

to gate the x-ray detection is by using laser-assisted photoemission (LAPE). As seen

above, this technique can be used for ultrashort x-ray pulse measurement. The LAPE

modification can also be used to detect femtosecond changes due to a laser-perturbed sample in a longer x-ray pulse, such as from a storage ring. An example of an experiment using this gated x-ray detection is shown schematically in Figure 5.3. Here, the ultrafast modifications in the long x-ray pulse due to the laser-perturbed sample would be detected as changes in the sideband amplitude caused by the LAPE modifications, just as they are monitored for ultrashort x-ray pulse measurement.

Femtosecond Optical Sampling of Synchrotron X-rays
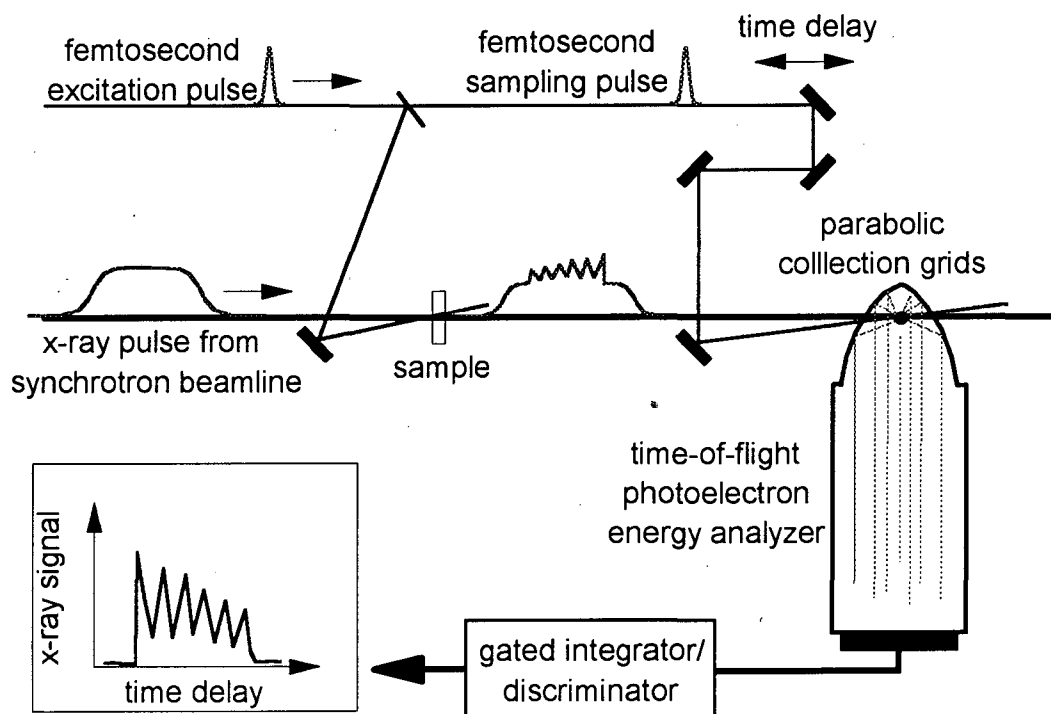
Figure 5.3: Laser-assisted photoelectric effect based gated x-ray detector.

Time-Resolved X-Ray Spectroscopies

Continued ultrashort x-ray pulse source development towards sources with higher peak or average spectral brightness will open up new possibilities for studying structural

dynamics in condensed matter. Similar source improvements were necessary in order to perform high-resolution structural studies in unperturbed crystals using x-ray diffraction techniques. Due to the small signal, extended x-ray absorption fine structure measurements and related techniques were not practical until x-ray sources with high spectral brightness became available [17]. Now, EXAFS is routinely used to study local order in amorphous materials or at surfaces, and x-ray diffraction techniques have made an impact in many fields over the years (e.g. protein crystallography [108]). X-ray techniques are now well established and yield vital structural information. Undoubtedly, improving the brightness of ultrashort x-ray pulse sources will have a similar impact on the study of ultrafast structural dynamics.

Time-resolved x-ray diffraction experiments

Using the right-angle Thomson scattering x-ray source, we have demonstrated that ultrafast time-resolved x-ray diffraction experiments are feasible. Ultrafast x-ray diffraction experiments have also been demonstrated using laser-produced plasma x-ray sources [34, 109]. With appropriate source development, a wide variety of time-resolved x-ray diffraction experiments should be able to be performed. One example is studying ultrafast disordering in semiconductors using single-shot time-resolved x-ray diffraction. Performing the experiment in a single-shot mode would eliminate any unwanted cumulative damage effects, and permit studies above the disordering threshold laser fluence. As metals behave in a simpler manner than semiconductors in some respects, it would be interesting to compare the heating [110] and melting dynamics [111] of metals versus those of semiconductors on the femtosecond time scale. Another exciting

possibility is time-resolved crystallography [112-115]. By studying the structural dynamics of proteins during photoexcitation, one may learn more about the connection between structure and function.

Time-resolved EXAFS experiments

Analyzing the extended x-ray absorption fine structure (EXAFS) around x-ray absorption edges has become an important tool for studying short-range order in condensed matter [16, 17]. Although recognized many years ago, because of the high spectral brightness needed to perform EXAFS experiments, the technique has only recently achieved wide-spread use. With continued development, ultrashort x-ray pulse sources with the necessary spectral brightness to perform time-resolved EXAFS experiments will become available.

One example of a future time-resolved EXAFS experiment is the study of ultrafast disordering. Because loss of long-range order does not necessarily mean that a crystal has melted, performing time-resolved EXAFS to study ultrafast disordering in semiconductors is an important, complementary technique to time-resolved x-ray diffraction. The feasibility of such experiments has been demonstrated by nanosecond resolution experiments using laser produced plasma x-rays to study the melting of Aluminum [116]. Another example is surface desorption [12, 117]. Surface EXAFS is a useful tool to understand the structural properties of surfaces, and applying the technique to study surface dynamics such as laser induced desorption should be possible. Time-resolved EXAFS can also be applied to the study of ultrafast photodissociation of molecules.

Chapter 6: Conclusion

Ultrashort x-ray pulse sources for the study of structural dynamics are just beginning to be developed. Until recently, ultrafast structural dynamics had to be studied using optical techniques, which indirectly probe atomic positions. Continued development of ultrashort x-ray pulse sources will lead to the development of the field of ultrafast structural dynamics in condensed matter. Ultrafast heating and/or disordering in semiconductors induced by laser pulses is already being studied using current sources. Other potential condensed matter physics applications include surface desorption, coherent phonons, and other forms of laser-induced phase transitions. In chemistry, atomic positions in molecules *during* photochemical reactions may be studied, instead of just observing the initial and final products. Another exciting possible application is in structural biology. As structure is related to function in proteins, one may be able to observe how a protein performs its function. These and other future applications make ultrafast x-ray spectroscopy of structural dynamics in condensed matter a promising field of research.

Of the several approaches towards ultrashort x-ray pulse generation, the Thomson scattering x-ray source may have the most attractive features. One of these features is the simplicity of the physics behind the x-ray generation, which results in reliable source performance. It also leads to the knowledge of the x-ray pulse duration, which is difficult to determine when the pulse duration is in the femtosecond range. The fact that the Thomson scattering source is tunable makes it applicable to a wide range of experiments. The highly collimated nature of the x-ray beam from the source makes it especially

attractive in the hard x-ray regime, where x-ray optics are difficult to make and expensive. Because an ultrashort laser pulse is used in the x-ray generation, the x-ray pulses are synchronized to laser pulses. This permits laser perturbed samples to be probed with the femtosecond x-rays with no timing jitter. The Thomson scattering x-ray source is also inexpensive compared to storage ring synchrotron sources of x-rays, as only a linear accelerator and a terawatt laser system are necessary. Finally, the Thomson scattering process is not only useful as a means of x-ray generation, but may be used as a probe of relativistic electron bunch properties.

Although it has many advantages, the Thomson scattering x-ray suffers from low x-ray flux, due to the small Thomson scattering cross-section for electron-photon scattering. As a result, many alternative schemes for ultrashort x-ray pulse generation are being pursued. These schemes range from laser-produced plasmas and high-order harmonic generation, to various means of modifying synchrotron radiation sources. For the most part, these alternative means of ultrashort x-ray pulse generation suffer from the fact that the actual pulse duration is not known. X-ray streak cameras may be used to determine the pulse duration, but their time resolution is generally in the picosecond range. One method of measuring the duration of femtosecond x-ray pulses is the laser-assisted photoelectric effect (LAPE). We have succesfully used the LAPE method to measure the pulse duration of soft x-rays generated by high-order harmonic generation, and it is in principle scaleable for use in the hard x-ray regime.

Of course, it is not enough to have a source of ultrashort x-ray pulses. In order to demonstrate that the Thomson scattering x-ray source is experimentally useful, we have performed time-resolved x-ray diffraction experiments on laser induced lattice dynamics in

semiconductors. Our experimental observations of ultrafast lattice expansion in laser perturbed InSb crystals using the Thomson scattering x-ray source show that time-resolved x-ray diffraction experiments can provide useful information about the transfer of energy from excited electrons to the lattice. The source development and time-resolved x-ray diffraction experiment represent some of the first steps in the development of ultrafast x-ray spectroscopy.

In order to perform a wider variety of time-resolved x-ray spectroscopy experiments, future ultrashort x-ray pulse sources need to have higher x-ray flux. One possibility is to improve the laser and linear accelerator performance. Because of the advantages that the Thomson scattering x-ray generation process possesses, and because laser and linear accelerator technologies are rapidly developing, making improvements to the Thomson scattering x-ray source may be the best option for a future source. Other likely candidates involve utilizing storage ring synchrotron sources to take advantage of the high flux, highly collimated, and tunable x-ray beams they provide. One of these is femtosecond electron beam slicing due to acceleration of a portion of the electron bunch interacting with a femtosecond laser pulse in a wiggler. Other methods involve modifying the x-ray pulses produced by the synchrotron. The modification of x-rays due to a laser perturbed sample may be time-resolved by gating the x-ray detection using laser-assisted photoemission. Femtosecond x-ray pulses may be switched out of the longer pulse by means of ultrafast disordering in semiconductors or some other ultrafast process. Some or all of these schemes may be used in the future to perform ultrafast x-ray spectroscopy.

Appendices

Appendix A: Relativistic Thomson Scattering Theory Mathematical Details

A number of approximations can be made when electrons are highly relativistic. Many of these involve the relativistic parameters $\beta = v/c \approx 1$ and $\gamma = E/mc^2 \gg 1$. Care must be taken when using these approximations in quantities involving ratios or other combinations of these relativistic parameters.

Equivalent deflection parameter

In cgs units, the force exerted on a relativistic electron by the periodic magnetic field of an undulator has a peak magnitude given by

$$F = e\beta B_0 \tag{A.1}$$

where e is the charge of the electron, and B_0 is the peak magnetic field in the undulator. The force on an electron in an electric field of moderate intensity (i.e. the electron is not accelerated to relativistic velocities in the electric field) has a peak magnitude given by

$$F = e\mathcal{E}_0 \tag{A.2}$$

where $\mathcal{E}_0$ is the peak electric field of the laser pulse. Therefore, the laser acts as an equivalent undulator, with an equivalent peak magnetic field given by (cgs units)

$$B_{equivalent} = \mathcal{E}_0/\beta \approx \mathcal{E}_0 \,. \tag{A.3}$$

All of the magnetic undulator formalism can be applied to the relativistic Thomson scattering case by simply replacing the undulator magnetic field with the electric field of the laser. Doing this for the deflection parameter, we obtain the equivalent deflection

parameter in Equation 2.6. As mentioned in Chapter 2, the equivalent deflection parameter (or dimensionless vector potential) can be thought of as the ratio of the ponderomotive potential of the electric field of the laser to the rest mass of the electron. To see this, let us start with the expression for the ponderomotive potential:

$$U_p = \frac{e^2 \mathcal{E}_0^2}{4m\omega^2}.$$

(A.4)

Using $\omega = 2\pi c/\lambda$, the ponderomotive potential can be expressed as

$$U_p = \frac{e^2 \mathcal{E}_0^2 \lambda^2}{16\pi^2 mc^2}.$$

(A.5)

Comparing this to Equation 2.6, we see that

$$K_{eq}^2 = \frac{U_p^2}{4mc^2}.$$

(A.6)

X-ray photon energy expression

To get from Equation 2.9 to Equation 2.12 using the approximations in Equations 2.8 and 2.11, care needs to be taken to keep terms of the appropriate order. Upon substitution of the approximate expressions, the denominator of Equation 2.9 becomes

$$1 - \beta \cos\theta \approx 1 - \left(1 - \frac{1}{2\gamma^2}\right)\left(1 - \frac{\theta^2}{2}\right).$$

(A.7)

Distributing the multiplication, we get

$$1 - \beta \cos\theta \approx 1 - \left(1 - \frac{1}{2\gamma^2} - \frac{\theta^2}{2} + \frac{\theta^2}{4\gamma^2}\right) \approx \frac{1}{2\gamma^2} + \frac{\theta^2}{2}$$

(A.8)

where the final expression is obtained when the highest order terms are kept. Equation 2.12 is obtained when Equation A.8 is substituted into Equation 2.9, and the factor of $2\gamma^2$

is factored out.

Appendix B: X-Ray Diffraction Using a Polychromatic, Divergent Source

Because of the polychromatic and divergent nature of the Thomson scattering x-ray source, a larger bandwidth of x-rays is diffracted than expected due to the intrinsic acceptance bandwidth of the crystal. This is due to the fact that different wavelengths satisfy the Bragg condition at different incident angles. In this way, matching of the Bragg condition can be achieved over a large range of the divergence of the source, assuming a uniformly distributed spectrum. This is schematically shown in Figure B.1.
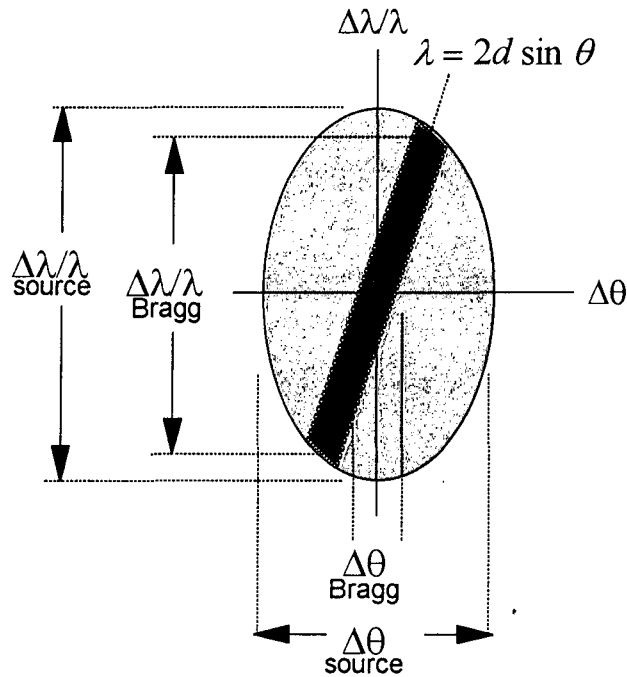

Figure B.1: Matching of the Bragg condition over the divergence of a polychromatic source.

For a beam divergence that is not too large (~ 1 mrad) so that matching within the source bandwidth can occur over the entire beam, the diffraction efficiency can be

estimated simply by the ratio of the intrinsic rocking curve width, $\Delta\theta_{Bragg}$, over the beam divergence, $\Delta\theta_{source}$. Rocking curve widths are typically ~ 10 μrad, so the diffraction efficiency for a 1 mrad divergence polychromatic source is ~ 10^{-2}. For the Thomson scattering x-ray source, aperturing the beam to a 1 mrad divergence in both transverse dimensions leads to a reduction of ~ 10^{-2} in the total number of photons per pulse reaching the sample. Therefore, an overall diffraction efficiency of ~ 10^{-4} is expected for the Thomson scattering x-ray source, apertured to ~ 1 mrad. Since ~ 5×10^4 photons per pulse are generated, about 5 diffracted photons per pulse should be diffracted over the 1 mrad angular range that is incident on the crystal.

Not only does matching of the Bragg condition for different wavelengths over the source divergence lead to a larger diffraction efficiency, it also results in a spectral shift that is less than expected for a given change in the sample angle, for a fixed detector. This is schematically shown in Figure B.2. The measured spectral shift with a fixed detector can be determined by considering which part of the divergence of the source the detector sees when the crystal is rotated, and calculating the expected spectral shift of that part of the beam. The net result is that the modified Bragg condition for the polychromatic source is given by

$$\frac{\Delta\lambda}{\lambda}\bigg|_{\mathrm{det}} = \frac{\Delta\theta}{\tan\theta_B}\left(1 - \frac{2d}{s+d}\right) \tag{B.1}$$

where s is the source to crystal distance, d is the crystal to detector distance, and θ_B is the Bragg angle for the unrotated crystal. From Equation B.1, we see that the spectral shift detected is less than the expected spectral shift using the derivative of the Bragg condition (Equation 3.1). Equation B.1 is used to fit the spectral shift in Figure 3.2.
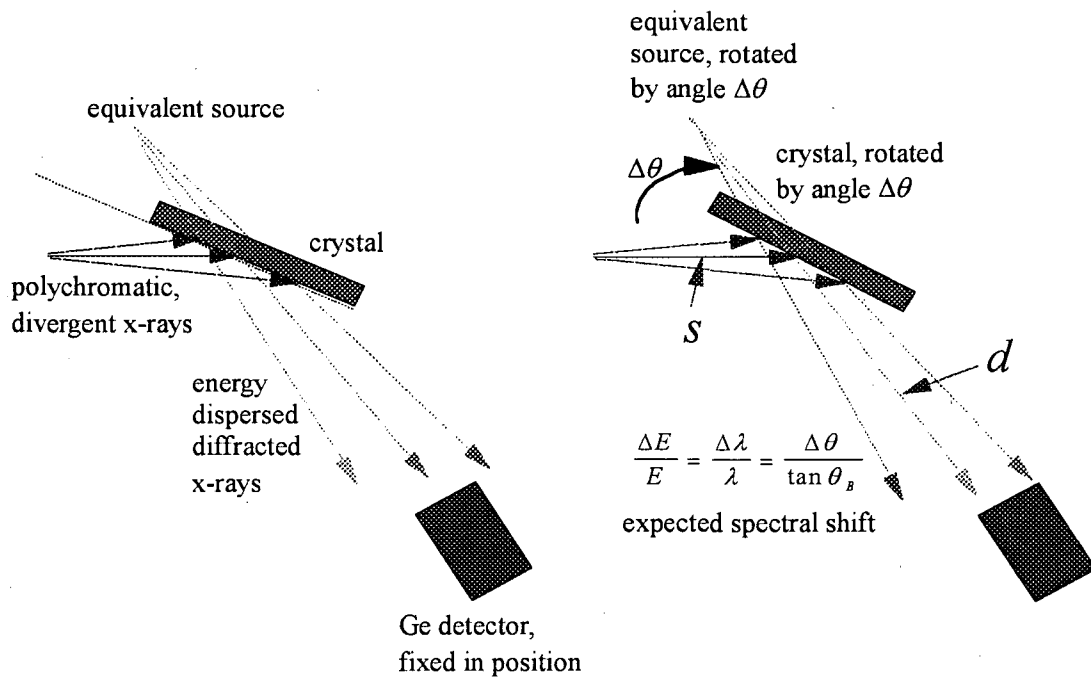
Figure B.2: Matching the Bragg condition with a fixed detector and rotating the crystal. The source to crystal distance is s, and the crystal to detector distance is d.

References

[1]   E. P. Ippen, C. V. Shank, and A. Dienes, "Passive Mode Locking of the CW Dye Laser," *Applied Physics Letters*, vol. 21, pp. 348-350, 1972.

[2]   R. L. Fork, B. I. Greene, and C. V. Shank, "Generation of optical pulses shorter than 0.1 psec by colliding pulse mode locking," *Applied Physics Letters*, vol. 38, pp. 671-672, 1981.

[3]   P. F. Barbara, J. G. Fujimoto, W. H. Knox, and W. Zinth, "Ultrafast Phenomena X," in *Springer Series in Chemical Physics*, vol. 62, F. P. Schafer, V. I. Goldanskii, and J. P. Toennies, Eds. Berlin Heidelberg New York: Springer-Verlag, 1996.

[4]   C. V. Shank, "Investigation of ultrafast phenomena in the femtosecond time domain," *Science*, vol. 233, pp. 1276-1280, 1986.

[5]   A. Baltuska, Z. Wei, M. S. Pshenichnikov, and D. A. Wiersma, "Optical pulse compression to 5 fs at a 1-MHz repetition rate," *Optics Letters*, vol. 22, pp. 102-104, 1997.

[6]   A. Baltuska, Z. Wei, M. S. Pshenichnikov, D. A. Wiersma, and R. Szipocs, "All-solid-state cavity-dumped sub-5-fs laser," *Applied Physics B*, vol. 65, pp. 175-188, 1997.

[7]   M. Nisoli, S. D. Silvestri, O. Svelto, R. Szipöcs, K. Ferencz, C. Spielmann, S. Sartania, and F. Krausz, "Compression of high-energy laser pulses below 5 fs," *Optics Letters*, vol. 22, pp. 522-524, 1997.

[8]   M. Nisoli, S. Stagira, S. D. Silvestri, O. Svelto, S. Sartania, Z. Cheng, M. Lenzner, C. Spielmann, and F. Krausz, "A novel-high energy pulse compression system: generation of multigigawatt sub-5-fs pulses," *Applied Physics B*, vol. 65, pp. 189-196, 1997.

[9]   P. F. Barbara, W. H. Knox, G. A. Mourou, and A. H. Zewail, "Ultrafast Phenomena IX," in *Springer-Verlag Series in Chemical Physics*. Berlin: Springer-Verlag, 1995.

[10]   C. V. Shank, R. Yen, and C. Hirlimann, "Time-resolved reflectivity measurement on femtosecond-optical-pulse-induced phase transitions on silicon," *Physical Review Letters*, vol. 50, pp. 454-457, 1983.

[11]   C. V. Shank, R. Yen, and C. Hirlimann, "Femtosecond-Time-resolved surface structural dynamics of optically excited silicon," *Physical Review Letters*, vol. 51, pp. 900-902, 1983.

[12]   J. A. Prybyla, T. F. Heinz, J. A. Misewich, M. M. T. Loy, and J. H. Glownia, "Desorption induced by femtosecond laser pulses," *Physical Review Letters*, vol. 64, pp. 1537-1540, 1990.

[13]   W. A. Kütt, W. Albrecht, and H. Kurz, "Generation of Coherent Phonons in Condensed Media," *IEEE Journal of Quantum Electronics*, vol. 28, pp. 2434-2444, 1992.

[14] R. E. Walkup, J. A. Misewich, J. H. Glownia, and P. P. Sorokin, "Time-Resolved Absorption Spectra of Dissociating Molecules," *Physical Review Letters*, vol. 65, pp. 2366-2369, 1990.

[15] W. H. Zachariasen, *Theory of X-ray Diffraction in Crystals*. New York: Wiley, 1945.

[16] D. C. Koningsberger and R. Prins, "X-ray absorption: Principles, applications, techniques of EXAFS, SEXAFS and XANES," in *Chemical Analysis*, vol. 92, J. D. Winefordner, Ed. New York: Wiley, 1988.

[17] P. Eisenberger and B. M. Kincaid, "EXAFS: New horizons in structure determinations," *Science*, vol. 200, pp. 1441-1447, 1978.

[18] M. M. Murnane, H. C. Kapteyn, S. P. Gordon, and R. W. Falcone, "Ultrashort X-Ray Pulses," *Applied Physics B*, vol. 58, pp. 261-266, 1994.

[19] M. M. Murnane, H. C. Kapteyn, M. D. Rosen, and R. W. Falcone, "Ultrafast X-ray Pulses from Laser-Produced Plasmas," *Science*, vol. 251, pp. 531-536, 1991.

[20] J. D. Kmetec, C. L. Gordon, J. J. Macklin, B. E. Lemoff, G. S. Brown, and S. E. Harris, "MeV x-ray generation with a femtosecond laser," *Physical Review Letters*, vol. 68, pp. 1527-1530, 1992.

[21] A. Rousse, P. Audebert, J. P. Geindre, F. Fallies, J. C. Gauthier, A. Mysyrowicz, G. Grillon, and A. Antonetti, "Efficient K alpha x-ray source from femtosecond laser-produced plasmas," *Physical Review E*, vol. 50, pp. 2200-2207, 1994.

[22] T. E. Glover, R. W. Schoenlein, A. H. Chin, and C. V. Shank, "Observation of laser assisted photoelectric effect and femtosecond high order harmonic radiation," *Physical Review Letters*, vol. 76, pp. 2468-2471, 1996.

[23] I. P. Christov, M. M. Murnane, and H. C. Kapteyn, "High-Harmonic Generation of Attosecond Pulses in the "Single-Cycle" Regime," *Physical Review Letters*, vol. 78, pp. 1251-1254, 1997.

[24] I. P. Christov, J. Zhou, J. Peatross, A. Rundquist, M. M. Murnane, and H. C. Kapteyn, "Nonadiabatic Effects in High-Harmonic Generation with Ultrashort Pulses," *Physical Review Letters*, vol. 77, pp. 1743-1746, 1996.

[25] A. A. Zholents and M. S. Zolotorev, "Femtosecond Pulses of Synchrotron Radiation," *Physical Review Letters*, vol. 76, pp. 912-915, 1995.

[26] J. Larsson, P. A. Heimann, A. M. Lindenberg, P. J. Schuck, P. H. Bucksbaum, R. W. Lee, H. A. Padmore, J. S. Wark, and R. W. Falcone, "Ultrafast structural changes measured by time-resolved x-ray diffraction," *Applied Physics A*, vol. 66, pp. 587-591, 1998.

[27] A. Ting, R. Fischer, A. Fisher, K. Evans, R. Burris, J. Krall, E. Esarey, and P. Sprangle, "Observation of 20 eV x-ray generation in a proof-of-principle laser synchrotron source experiment," *Journal of Applied Physics*, vol. 78, pp. 575-577, 1995.

[28] E. Esarey, P. Sprangle, A. Ting, and S. K. Ride, "Laser synchrotron radiation as a compact source of tunable, short pulse hard x-rays," *Nuclear Instruments and Methods in Physics Research A*, vol. 331, pp. 545-549, 1993.

[29] P. Sprangle, A. Ting, E. Esarey, and A. Fishher, "Tunable, short pulse hard x-rays from a compact laser synchrotron source," *Journal of Applied Physics*, vol. 72, pp. 5032-5038, 1992.

[30] K.-J. Kim, S. Chattopadhyay, and C. V. Shank, "Generation of femtosecond x-ray pulses by 90 degree Thomson scattering," *Nuclear Instruments and Methods in Physics Research A*, vol. 341, pp. 351-354, 1994.

[31] W. P. Leemans, R. W. Schoenlein, P. Volfbeyn, A. H. Chin, T. E. Glover, P. Balling, M. Zolotorev, K.-J. Kim, S. Chattopadhyay, and C. V. Shank, "X-ray based time resolved electron beam characterization via 90° Thomson scattering," *Physical Review Letters*, vol. 77, pp. 4182-4185, 1996.

[32] W. P. Leemans, R. W. Schoenlein, P. Volfbeyn, A. H. Chin, T. E. Glover, P. Balling, M. Zolotorev, K.-J. Kim, S. Chattopadhyay, and C. V. Shank, "Interaction of Relativistic Electrons with Ultrashort Laser Pulses: Generation of Femtosecond X-Rays and Microprobing of Electron Beams," *IEEE Journal of Quantum Electronics*, vol. 33, pp. 1925-1934, 1997.

[33] R. W. Schoenlein, W. P. Leemans, A. H. Chin, P. Volfbeyn, T. E. Glover, P. Balling, M. Zolotorev, K.-J. Kim, S. Chattopadhyay, and C. V. Shank, "Femtosecond X-ray Pulses at 0.4 angstroms Generated by 90° Thomson Scattering: A Tool for Probing the Structural Dynamics of Materials," *Science*, vol. 274, pp. 236-238, 1996.

[34] T. Guo, C. G. Rose-Petruck, R. Jimenez, F. Raksi, J. A. Squier, B. Walker, K. R. Wilson, and C. P. Barty, "Picosecond-milliangstrom resolution dynamics by ultrafast x-ray diffraction," *SPIE Proceedings*, vol. 3157, pp. 84-92, 1997.

[35] N. C. Woolsey and J. S. Wark, "Modeling of time resolved x-ray diffraction from laser-shocked crystals," *Journal of Applied Physics*, vol. 81, pp. 3023-3037, 1997.

[36] B. C. Larson, C. W. White, T. S. Noggle, and J. F. Barhorst, "Time-resolved x-ray diffraction measurement of the temperature and temperature gradients in silicon during pulsed laser annealing," *Applied Physics Letters*, vol. 42, pp. 282-284, 1983.

[37] B. C. Larson, C. W. White, T. S. Noggle, and D. Mills, "Synchrotron X-Ray Diffraction Study of Silicon during Pulsed-Laser Annealing," *Physical Review Letters*, vol. 48, pp. 337-340, 1982.

[38] J. R. Buschert, J. Z. Tischler, D. M. Mills, Q. Zhao, and R. Colella, "Time resolved x-ray diffraction study of laser annealing in silicon at grazing incidence," *Journal of Applied Physics*, vol. 66, pp. 3523-3525, 1989.

[39] P. Stampfli and K. H. Bennemann, "Time Dependence of the laser-induced femtosecond lattice instability of Si and GaAs - Role of longitudinal optical phonons," *Physical Review B*, vol. 49, pp. 7299-7305, 1994.

[40] P. L. Silvestrelli, A. Alavi, M. Parrinello, and D. Frenkel, "Structural, dynamical, electronic, and bonding properties of laser-heated silicon: An *ab initio* molecular-dynamics study," *Physical Review B*, vol. 56, pp. 3806-3812, 1997.

[41] P. L. Silvestrelli, A. Alavi, M. Parrinello, and D. Frenkel, "*Ab Initio* Molecular Dynamics Simulation of Laser Melting of Silicon," *Physical Review Letters*, vol. 77, pp. 3149-3152, 1996.

[42] P. Stampfli and K. H. Bennemann, "Theory for the laser-induced femtosecond phase transition of silicon and GaAs," *Applied Physics A*, vol. 60, pp. 191-196, 1995.

[43] P. Stampfli and K. H. Bennemann, "Theory for the instability of the diamond structure of Si, Ge, and C induced by a dense electron-hole plasma," *Physical Review B*, vol. 42, pp. 7163-7173, 1990.

[44] P. Stampfli and K. H. Bennemann, "Dynamical theory of the laser-induced instability of silicon," *Physical Review B*, vol. 46, pp. 10686-10692, 1992.

[45] H. W. K. Tom, T. F. Heinz, and Y. R. Shen, "Second-harmonic reflection from silicon surface and its relation to structural symmetry," *Physical Review Letters*, vol. 51, pp. 1983-1986, 1983.

[46] E. N. Glezer, Y. Siegal, L. Huang, and E. Mazur, "Behavior of $\chi^{(2)}$ during a laser-induced phase transition in GaAs," *Physical Review B*, vol. 51, pp. 9589-9596, 1995.

[47] D. T. Attwood, "Introduction to X-Ray Physics and Technology," , 1995.

[48] A. Hofmann, "Theory of Synchrotron Radiation," in *Synchrotron Radiation Sources and their Applications, Scottish Universities' Summer School in Physics*, C. N. Greaves and I. H. Munro, Eds. Edinburgh: Scottish Universities Summer School in Physics, 1985, pp. 28-38.

[49] A. Hofmann, "Quasi-Monochromatic Synchrotron Radiation from Undulators," *Nuclear Instruments and Methods*, vol. 152, pp. 17-21, 1978.

[50] C. Spielmann, P. F. Curley, T. Brabec, and F. Krausz, "Ultrabroadband Femtosecond Lasers," *IEEE Journal of Quantum Electronics*, vol. 30, pp. 1100-1114, 1994.

[51] G. Mourou, "The ultrahigh-peak-power laser: present and future," *Applied Physics B*, vol. 65, pp. 205-211, 1997.

[52] M. D. Perry and G. Mourou, "Terawatt to Petawatt Subpicosecond Lasers," *Science*, vol. 264, pp. 917-924, 1994.

[53] D. Strickland and G. Mourou, "Compression of amplified chirped optical pulses," *Optics Communications*, vol. 56, pp. 219-221, 1985.

[54] B. E. Lemoff and C. P. J. Barty, "Quintic-phase-limited, spatially uniform expansion and recompression of ultrashort optical pulses," *Optics Letters*, vol. 18, pp. 1651-1653, 1993.

[55] B. E. Lemoff and C. P. J. Barty, "Multiterawatt 30-fs Ti:sapphire laser system," *Optics Letters*, vol. 19, pp. 1442-1444, 1994.

[56] G. A. Mourou, C. P. J. Barty, and M. D. Perry, "Ultrahigh-Intensity Lasers: Physics of the Extreme on a Tabletop," *Physics Today*, pp. 22-28, 1998.

[57] C. LeBlanc, G. Grillon, J. P. Chambaret, A. Migus, and A. Antonetti, "Compact and efficient multipass Ti:Sapphire system for femtosecond chirped-pulse amplification at the terawatt level," *Optics Letters*, vol. 18, pp. 140-142, 1993.

[58] O. E. Martinez, "3000 Times Grating Compressor with Positive Group Velocity Dispersion: Application to Fiber Compensation in 1.3-1.6 μm Region," *IEEE Journal of Quantum Electronics*, vol. QE-23, pp. 59-64, 1987.

[59] M. J. W. Rodwell, D. M. Bloom, and K. J. Weingarten, "Subpicosecond laser timing stabilization," *IEEE Journal of Quantum Electronics*, vol. 25, pp. 817-827, 1989.

[60] P. Volfbeyn, W. Leemans, and L. Archambault, "Time integrated measurement techniques for the femtosecond x-ray experiment," Center for Beam Physics, AFRD, LBNL, Berkeley, CA CBP Tech Note Number 105, December 30, 1995 1995.

[61] B. C. Larson, J. Z. Tischler, and D. M. Mills, "Nanosecond resolution time-resolved x-ray study of silicon during pulsed-laser irradiation," *Journal of Materials Research*, vol. 1, pp. 144-154, 1986.

[62] M. C. Downer, R. L. Fork, and C. V. Shank, "Femtosecond imaging of melting and evaporation at a photoexcited silicon surface," *Journal of the Optical Society of America B*, vol. 2, pp. 595-599, 1985.

[63] H. W. K. Tom, G. D. Aumiller, and C. H. Brito-Cruz, "Time-resolved study of laser-induced disorder of Si surfaces," *Physical Review Letters*, vol. 60, pp. 1438-1441, 1988.

[64] L. Huang, J. P. Callan, E. N. Glezer, and E. Mazur, "GaAs under Intense Ultrafast Excitation: Response of the Dielectric Function," *Physical Review Letters*, vol. 80, pp. 185-188, 1998.

[65] E. N. Glezer, Y. Siegal, L. Huang, and E. Mazur, "Laser-induced band-gap collapse in GaAs," *Physical Review B*, vol. 51, pp. 6959-6970, 1995.

[66] Y. Siegal, E. N. Glezer, and E. Mazur, "Dielectric constant of GaAs during a subpicosecond laser-induced phase transition," *Physical Review B*, vol. 49, pp. 16403-16406, 1994.

[67] S. V. Govorkov, T. Schröder, I. L. Shumay, and P. Heist, "Transient gratings and second-harmonic probing of the phase transformation of a GaAs surface under femtosecond laser irradiation," *Physical Review B*, vol. 46, pp. 6864-6868, 1992.

[68] T. Schröder, W. Rudolph, S. V. Govorkov, and I. L. Shumay, "Femtosecond Laser-Induced Melting of GaAs Probed by Optical Second-Harmonic Generation," *Applied Physics A*, vol. 51, pp. 49-51, 1990.

[69] K. Sokolowski-Tinten, H. Schulz, J. Bialkowski, and D. v. d. Linde, "Two Distinct Transitions in Ultrafast Solid-Liquid Phase Transformations of GaAs," *Applied Physics A*, vol. 53, pp. 227-234, 1991.

[70] D. H. Reitze, X. Wang, H. Ahn, and M. C. Downer, "Femtosecond laser melting of graphite," *Physical Review B*, vol. 40, pp. 11986-11989, 1989.

[71] I. L. Shumay and U. Höfer, "Phase transformations of an InSb surface induced by strong femtosecond laser pulses," *Physical Review B*, vol. 53, pp. 15878-15884, 1996.

[72] B. E. Warren, *X-ray Diffraction*. Reading, MA: Addison Wesley Publishing Co., 1969.

[73] B. L. Henke, E. M. Gullikson, and J. C. Davis, "X-ray Interactions: Photoabsorption, scattering, transmission, and reflection at E = 50-30,000 eV, Z = 1-92," *Atomic Data and Nuclear Data Tables*, vol. 54, pp. 181-342, 1993.

[74]   R. W. James, *The Optical Principles of the Diffraction of X-rays*. London: Bell, 1962.

[75]   B. K. Agarwal, *X-Ray Spectroscopy*, vol. 15, 2nd ed. Berlin: Springer-Verlag, 1991.

[76]   B. Klar and F. Rustichelli, "Dynamical Neutron Diffraction by Ideally Curved Crystals," *Nuovo Cimento*, vol. 13B, pp. 249-270, 1973.

[77]   A. Lietoila and J. F. Gibbons, "Calculation of carrier and lattice temperatures induced in Si by picosecond laser pulses," *Applied Physics Letters*, vol. 40, pp. 624-626, 1982.

[78]   H. M. v. Driel, "Kinetics of high-density plasmas generated in Si by 1.06-μm and 0.53-μm picosecond laser pulses," *Physical Review B*, vol. 35, pp. 8166-8176, 1987.

[79]   J. A. Kash, J. C. Tsang, and J. M. Hvam, "Subpicosecond Time-Resolved Raman Spectroscopy of LO Phonons in GaAs," *Physical Review Letters*, vol. 54, pp. 2151-2154, 1985.

[80]   M. C. Downer and C. V. Shank, "Ultrafast Heating of Silicon on Sapphire by Femtosecond Optical Pulses," *Physical Review Letters*, vol. 56, pp. 761-764, 1986.

[81]   S. Kojima, K.-Y. Liu, Y. Kudo, S. Kawado, T. Ishikawa, and T. Matsushita, "Time-Resolved X-Ray Diffraction Measurement of Silicon Surface during Laser Irradiation under Grazing-Incidence Conditions," *Japanese Journal of Applied Physics*, vol. 33, pp. 5612-5616, 1994.

[82]   P. C. Becker, H. L. Fragnito, C. H. Brito Cruz, R. L. Fork, J. E. Cunningham, J. E. Henry, and C. V. Shank, "Femtosecond Photon Echoes from Band to Band Transitions in GaAs," *Physical Review Letters*, vol. 61, pp. 1647-1649, 1988.

[83]   C. Kittel, *Introduction to Solid State Physics*, Sixth ed. New York, Chichester, Brisbane, Toronto, Singapore: John Wiley & Sons, Inc., 1986.

[84]   P. Langot, N. D. Fatti, D. Christofilos, R. Tommasi, and F. Vallee, "Femtosecond investigation of the hot-phonon effect in GaAs at room temperature," *Physical Review B*, vol. 54, pp. 14,487-14,493, 1996.

[85]   D. v. d. Linde, J. Kuhl, and H. Klingenberg, "Raman Scattering from Nonequilibrium LO Phonons with Picosecond Resolution," *Physical Review Letters*, vol. 44, pp. 1505-1508, 1980.

[86]   R. G. Ulbrich, V. Narayanamurti, and M. A. Chin, "Propagation of Large-Wave-Vector Acoustic Phonons in Semiconductors," *Physical Review Letters*, vol. 45, pp. 1432-1435, 1980.

[87]   S. C. Chapra and R. P. Canale, *Numerical Methods for Engineers*, 2nd ed. New York: McGraw-Hill, 1988.

[88]   E. J. Yoffa, "Dynamics of dense laser-induced plasmas," *Physical Review B*, vol. 21, pp. 2415-2425, 1980.

[89]   P. M. Fauchet, "The Auger Rate in Highly Excited Indium Antimonide," *Physica Status Solidi B*, vol. 110, pp. K11-K15, 1982.

[90]   D. E. Gray, "American Institute of Physics handbook," , 3rd ed. New York: McGraw Hill, 1972.

[91] J. A. V. Vechten, R. Tsu, F. W. Saris, and D. Hoonhout, "Reasons to Believe Pulsed Laser Annealing of Si Does Not Involve Simple Thermal Melting," *Physics Letters*, vol. 74A, pp. 417-421, 1979.

[92] J. A. V. Vechten, R. Tsu, and F. W. Saris, "Nonthermal Pulsed Laser Annealing of Si; Plasma Annealing," *Physics Letters*, vol. 74A, pp. 422-426, 1979.

[93] S. Hunsche, K. Wienecke, T. Dekorsy, and H. Kurz, "Impulsive Softening of Coherent Phonons in Tellurium," *Physical Review Letters*, vol. 75, pp. 1815-1818, 1995.

[94] J. Larsson, Z. Chang, E. Judd, P. J. Schuck, R. W. Falcone, P. A. Heimann, H. A. Padmore, H. C. Kapteyn, P. H. Bucksbaum, M. M. Murnane, R. W. Lee, A. Machacek, J. S. Wark, X. Liu, and B. Shan, "Ultrafast X-ray diffraction using a streak-camera detector in averaging mode.," *Optics Letters*, vol. 22, pp. 1012-1014, 1997.

[95] A. Maksimchuk, M. Kim, J. Workman, G. Korn, J. Squier, D. Du, D. Umstadter, and G. Mourou, "Signal averaging x-ray streak camera with picosecond jitter," *Review of Scientific Instruments*, vol. 67, pp. 697-699, 1996.

[96] J. M. Schins, P. Breger, P. Agostini, R. C. Constantinescu, H. G. Muller, G. Grillon, A. Antonetti, and A. Mysyrowicz, "Observation of laser-assisted Auger decay in argon," *Physical Review Letters*, vol. 73, pp. 2180-2183, 1994.

[97] Y. Kobayashi, T. Sekikawa, Y. Nabekawa, and S. Watanabe, "27-fs extreme ultraviolet pulse generation by high-order harmonics," *Optics Letters*, vol. 23, pp. 64-66, 1998.

[98] Z. Chang, A. Rundquist, H. Wang, M. M. Murnane, and H. C. Kapteyn, "Generation of Coherent Soft X-Rays at 2.7 nm Using High Harmonics," *Physical Review Letters*, vol. 79, pp. 2967-2970, 1997.

[99] J. J. Macklin, J. D. Kmetec, and C. L. Gordon, "High-order harmonic generation using intense femtosecond pulses," *Physical Review Letters*, vol. 70, pp. 766-769, 1993.

[100] P. B. Corkum, "Plasma Perspective on Strong-Field Multiphoton Ionization," *Physical Review Letters*, vol. 71, pp. 1994-1997, 1993.

[101] W. Becker, S. Long, and J. K. McIver, "Higher-harmonic production in a model atom with short-range potential," *Physical Review A*, vol. 41, pp. 4112-4115, 1990.

[102] M. Lewenstein, P. Balcou, M. Y. Ivanov, A. L'Huiller, and P. B. Corkum, "Theory of high-harmonic generation by low-frequency laser fields," *Physical Review A*, vol. 49, pp. 2117-2132, 1994.

[103] P. Kung, H. Lihn, and H. Wiedemann, "Generation and measurement of 50-fs (rms) electron pulses," *Physical Review Letters*, vol. 73, pp. 967-70, 1994.

[104] L. Serafini, R. Zhang, and C. Pellegrini, "Generation of sub-picosecond electron bunches from RF photoinjectors," *Nuclear Instruments and Methods in Physics Research A*, vol. 387, pp. 305-314, 1997.

[105] E. Esarey, R. F. Hubbard, W. P. Leemans, A. Ting, and P. Sprangle, "Electron Injection into Plasma Wake Fields by Colliding Laser Pulses," *Physical Review Letters*, vol. 79, pp. 2682-2685, 1997.

[106] D. Umstadter, J. K. Kim, and E. Dodd, "Laser Injection of Ultrashort Electron Pulses into Wakefield Plasma Waves," *Physical Review Letters*, vol. 76, pp. 2073-2076, 1996.

[107] A. Antonetti, F. Blasco, J. P. Chamaret, G. Cheriaux, G. Darpentigny, C. LeBlanc, P. Rousseau, S. Ranc, G. Rey, and F. Salin, "A laser system producing $5 \times 10^{19} W/cm^2$ at 10 Hz," *Applied Physics B*, vol. 65, pp. 197-204, 1997.

[108] C. T. Prewitt, P. Coppens, J. C. Phillips, and L. W. Finger, "New Opportunities in Synchrotron X-ray Crystallography," *Science*, vol. 238, pp. 312-319, 1987.

[109] C. Rischel, A. Rousse, I. Uschmann, P.-A. Albouy, J.-P. Geindre, P. Audebert, J.-C. Gauthier, E. Förster, J.-L. Martin, and A. Antonetti, "Femtosecond time-resolved X-ray diffraction from laser-heated organic films," *Nature*, vol. 390, pp. 490-492, 1997.

[110] P. Chen, I. V. Tomov, and P. M. Rentzepis, "Time resolved heat propagation in a gold crystal by means of picosecond x-ray diffraction," *Journal of Chemical Physics*, vol. 104, pp. 10001-10007, 1996.

[111] S. Williamson, G. Mourou, and J. C. M. Li, "Time-Resolved Laser-Induced Phase Transformation in Aluminum," *Physical Review Letters*, vol. 52, pp. 2364-2367, 1984.

[112] B. Perman, V. Srajer, Z. Ren, T.-y. Teng, C. Pradervand, T. Ursby, D. Bourgeois, F. Schotte, M. Wulff, R. Kort, K. Hellingwerf, and K. Moffat, "Energy Transduction on the Nanosecond Time Scale: Early Structural Events in a Xanthopsin Photocycle," *Science*, vol. 279, pp. 1946-1950, 1998.

[113] V. Srajer, T.-y. Teng, T. Ursby, C. Pradervand, Z. Ren, S.-i. Adachi, W. Schildkamp, D. Bourgeois, M. Wulff, and K. Moffat, "Photolysis of the Carbon Monoxide Complex of Myoglobin: Nanosecond Time-Resolved Crystallography," *Science*, vol. 274, pp. 1726-1729, 1996.

[114] U. K. Genick, G. E. O. Borgstahl, K. Ng, Z. Ren, C. Pradervand, P. M. Burke, V. Srajer, T.-Y. Teng, W. Schildkamp, D. E. McRee, K. Moffat, and E. D. Getzoff, "Structure of a Protein Photocycle Intermediate by Millisecond Time-Resolved Crystallography," *Science*, vol. 275, pp. 1471-1475, 1997.

[115] K. Moffat, Y. Chen, K. Ng, D. McRee, and E. D. Getzoff, "Time-resolved crystallography: principles, problems and practice," *Philisophical Transactions of the Royal Society of London A*, vol. 340, pp. 175-190, 1992.

[116] H. M. Epstein, R. E. Schwerzel, P. J. Mallozi, and B. E. Campbell, "Flash-EXAFS for structural analysis of transient species: rapidly melting aluminum," *Journal of the American Chemical Society*, vol. 105, pp. 1466-1468, 1983.

[117] J. A. Prybyla, H. W. K. Tom, and G. D. Aumiller, "Femtosecond time-resolved surface reaction: Desorption of Co from Cu(111) in <325 fsec," *Physical Review Letters*, vol. 68, pp. 503-506, 1992.

Alan Chin
08/19/98

Comparison of X-ray Pulse Sources

x-ray source	photons per pulse	divergence (mrad)	x-ray photon energy (keV)	relative bandwidth	source area (mm^2)	pulse spectral brightness (photons/ pulse-mm^2-mrad^2-(0.1% b.w.))	rep. rate	flux (photons/s-mrad^2)	flux (photons/s-0.1% b.w.-mrad^2)	average spectral brightness (photons/s-mm^2-mrad^2-(0.1% b.w.))	pulse duration (fs)
right-angle Thomson	5.00×10^4	10.00	7 to 30	0.15	1.00×10^{-2}	3.33×10^2	5	2.50×10^3	1.67×10^1	1.67×10^3	300
ALS undulator	2.63×10^9	1.00	0.50	0.01	1.00×10^{-2}	2.63×10^{10}	3.8×10^8	1.00×10^{18}	1.00×10^{17}	1.00×10^{19}	3.0×10^4
ALS bend magnet	1.32×10^8	1.00	1 to 5	1.00	1.00×10^{-2}	1.32×10^7	3.8×10^8	5.00×10^{16}	5.00×10^{13}	5.00×10^{15}	3.0×10^4
ALS wiggler	7.89×10^8	1.00	1 to 5	1.00	1.00×10^{-2}	7.89×10^7	3.8×10^8	3.00×10^{17}	3.00×10^{14}	3.00×10^{16}	3.0×10^4
ALS superbend	1.32×10^8	1.00	2 to 10	1.00	1.00×10^{-2}	1.32×10^7	3.8×10^8	5.00×10^{17}	5.00×10^{13}	5.00×10^{15}	3.0×10^4
laser-produced plasma (French)	5.00×10^4	71.00	2	0.0005	2.40×10^{-3}	8.27×10^3	10	9.92×10^1	1.98×10^2	8.27×10^4	700?
laser-produced plasma (Wilson)	1.00×10^9	3500.00	8	0.0002	1.00×10^{-4}	4.08×10^6	20	1.63×10^3	8.16×10^3	8.16×10^7	?
x-ray diode (Rentzepis)	1.00×10^7	1000.00	8	0.0002	1.60×10^1	3.13	300	3.00×10^3	1.50×10^4	9.38×10^2	8×10^3

Notes:
- Variations by factors of 2 are likely in many of these numbers.
- The right-angle Thomson scattering x-rays source numbers assume 30 keV x-rays (scattering off of 50 MeV electrons) with an electron beam emittance of 1×10^{-6} m-rad.
- ALS undulator numbers assume 100 periods (for the relative bandwidth) and an electron beam emittance of 1×10^{-7} m-rad (for source size and divergence). Most of the radiation is contained in a cone of ~ 1 mrad divergence. At 1.5 GeV, the natural x-ray divergence is ~ 300 μrad, but the electron beam emittance may determine most of the divergence.
- ALS bend, wiggler, and superbend assume an electron beam emittance of 1×10^{-7} m-rad (for source size and divergence). The vertical divergence is limited to ~ 1 mrad, but the horizontal divergence can be much larger.
- The numbers for the laser-produced plasma x-rays by the French group at ENSTA assume that the source spot size is comparable to the quoted x-ray focal spot size, and the divergence is the square root of the collection solid angle of the focusing toroidal x-ray mirror. The photons per pulse are on the target. Approximately 20 mJ of laser pulse energy are used for x-ray generation, 10% of which creates a preformed plasma for efficient generation of hot electrons.
- The numbers for the laser-produced plasma x-rays by the Wilson group at UCSD assume that the source spot size is ~ 10 μm, from knife edge imaging measurements of the x-ray emitting volume. The numbers are for 4π collection solid angle. Approximately 150 mJ of laser pulse energy are used for x-ray generation.
- The x-ray diode numbers assume the source area is the same as the anode area.

ERNEST ORLANDO LAWRENCE BERKELEY NATIONAL LABORATORY
ONE CYCLOTRON ROAD | BERKELEY, CALIFORNIA 94720